Copyright Undertaking

STUDYING LIQUID SULFUR IN LITHIUM-SULFUR BATTERIES

SHI FANGYI

PhD

The Hong Kong Polytechnic University

2024

The Hong Kong Polytechnic University
Department of Applied Physics

STUDYING LIQUID SULFUR IN LITHIUM-SULFUR BATTERIES

Shi Fangyi

A thesis submitted in partial fulfillment of the requirements for
the degree of Doctor of Philosophy

August 2023

CERTIFICATE OF ORIGINALITY

I hereby declare that this thesis is my own work and that, to the best of my knowledge and belief, it reproduces no material previously published or written, nor material that has been accepted for the award of any other degree or diploma, except where due acknowledgement has been made in the text.

____(Signed)

_________Shi Fangyi___________ (Name of studen

Abstract

The lithium-sulfur batteries have entered a stage of flourishing development for their attractive gravimetric energy density of 2567 Wh/kg and low cost of sulfur stock. Through decades of efforts, electrochemical performance, such as specific capacity, cycling stability, and rate performance, has been greatly improved. However, some problems still need to be overcome to achieve practical Li-S batteries, including the insulating nature of S/Li_2S, the shuttle effect of soluble lithium polysulfides, and the slow reaction kinetics of the Li_2S deposition. In addition, the real reaction process of Li-S batteries is still unclear due to the sensitivity of sulfur species to the environment and the complex reaction mechanisms. Liquid sulfur has been recently discovered in the charging process of Li-S batteries using optical microscopy and *in situ* Raman spectroscopy on an optical cell. Liquid sulfur has specific advantages over solid sulfur: i. The reshaping ability brings liquid sulfur a higher charging capacity even at a large current density. ii. The lower reaction barrier of liquid-liquid conversion leads to fast reaction kinetics. This thesis explores the role and application of liquid sulfur in Li-S batteries.

Firstly, we observed the sulfur generation and growth on the thick MoS_2 nanoflakes. Liquid sulfur can be generated on the basal plane of MoS_2 but would be solidified quickly when it comes into contact with crystalline sulfur growing from the edges. Annealing MoS_2 nanoflakes in the H_2 atmosphere can introduce oxide around the edges

and sulfur vacancies on the basal plane. These two factors enable the generation of liquid sulfur throughout the whole charging process, even at large overpotentials and low temperatures. The same annealing method can also be applied to other transition metal dichalcogenide (TMD) materials (WS_2 and $MoSe_2$). This research suggests that functionalized TMD materials have the potential to achieve a pure liquid sulfur-lithium battery system.

Compared to TMD materials, carbon is more common in Li-S batteries. To better understand the liquid sulfur, we observe the nucleation and growth of sulfur on single-layer graphene by *in situ* Raman and optical microscopy. Due to its metastable characterization, we found the supercooled liquid sulfur hard to keep as the final charging product. The important role of liquid sulfur has been verified through analysis of the growth dynamic of liquid sulfur in the charging process. Furthermore, we found that the current density strongly influenced the morphology and density of liquid sulfur, while the charge capacity was limited. Based on these findings, a cathode host supporting liquid sulfur formation has been designed to achieve high electrochemical performance at a high charging rate.

The third work has inspected the effects of charge transfer and mass transport of reaction species on liquid sulfur deposition. The electrochemical reaction kinetics of liquid sulfur was systematically studied by gradually increasing the conductivity of the substrate, introducing catalysts, and changing the temperature. This work reveals that excellent conductivity, efficient catalyst, and suitable temperature favor liquid sulfur deposition kinetics.

List of Publications

#Equal contribution first author; *Corresponding author.

1. **Fangyi Shi**#, Xuyun Guo#, Chunhong Chen, Lyuchao Zhuang, Jingya Yu, Qi Qi, Ye Zhu, Zheng-Long Xu,* Shu Ping Lau*, Unlocking liquid sulfur chemistry for fast-charging lithium−sulfur batteries, Nano Letter, 2023, Accepted.

2. **Fangyi Shi**, Nicolas Onofrio, Chunhong Chen, Songhua Cai, Yanyong Li, Lingling Zhai, Lyuchao Zhuang, Zheng-Long Xu*, Shu Ping Lau*, Stable liquid-sulfur generation on transition-metal dichalcogenides toward low-temperature lithium–sulfur batteries. ACS nano, 2022, 16,14412-14421.

3. **Fangyi Shi**, Chunhong Chen, Zheng-Long Xu*, Recent advances on electrospun nanofiber materials for post-lithium ion batteries, Advanced Fiber Materials, 2021, 3, 275-301.

4. **Fangyi Shi**#, Jingya Yu#, Chunhong Chen#, Shu Ping Lau, Wei Lv, Zheng-Long Xu*, Advances in understanding and regulation of sulfur conversion processes in metal–sulfur batteries, Journal of Materials Chemistry A 2022, 10, 19412-19443.

5. **Fangyi Shi**#, Lingling Zhai#, Qingqing Liu, Jingya Yu, Shu Ping Lau*, Bao Yu Xia*, and Zheng-Long Xu*, Emerging catalytic materials for practical lithium-sulfur batteries. Journal of Energy Chemistry, 2023, 76, 127-145.

6. Chunhong Chen#, **Fangyi Shi**#, Shishi Zhang, Yaqiong Su, Zheng-Long Xu*, Ultrastable and high energy calcium rechargeable batteries enabled by calcium intercalation in a NASICON cathode." Small,2022,14, 2107853.

7. Chunhong Chen, **Fangyi Shi**, Zheng-Long Xu*, Advanced electrode materials for nonaqueous calcium rechargeable batteries. Journal of Materials Chemistry A, 2021, 9, 11908-11930.

8. Lyuchao Zhuang, Qi Wei, Chuanzhao Li, Hui Ren, Yanyong Li, **Fangyi Shi**, Lingling Zhai, Kai Leng, Mingjie Li, Shu Ping Lau*. Efficient light-emitting diodes via hydrogen bonding induced phase modulation in quasi-2D perovskites. Advanced Fiber Materials, 2022, 10, 2201180.

Acknowledgements

How time flies, my three years of my Ph.D. are coming to an end. Ph.D. is not an easy job, and I faced many challenges during this experience. My heartfelt thanks to everyone who helped me during my Ph.D.

To start, I wish to extend my sincere appreciation to my chief supervisor, Professor Shu Ping Lau. Over the course of three years dedicated to my Ph.D. research, Prof. Lau has consistently offered invaluable guidance, insightful suggestions, and unwavering encouragement. He also provided me with a chance as an exchange student in Cambridge to broaden my horizons and experience different cultures. Without his unconditional support, I could not have grown to where I am now.

In addition, I am very grateful to my co-supervisor Dr. Xu Zhenglong. Without his recommendation, I would not have had this opportunity for a Ph.D. Though I was a junior in this research field three years ago, Dr. Xu is very responsible and patient and gave me a lot of guidance on my project. He taught me to fish instead of giving me a fish, which laid the foundation for my future development.

I would also like to thank the scientific officers in the Department of Applied Physics and the University Research Facility in Materials Characterization and Device Fabrication for their invaluable assistance in conducting sample characterizations.

I would like to thank Dr. Chunhong Chen, Dr. Lingling Zhai and Dr. Lyuchao Zhuang. They gave me a lot of discussion and guidance about my research. Besides, thanks to my past and present colleagues, Dr. Yanyong Li, Dr. Yi Hu, Dr. Qi Wei, Dr. Linlong Lyu, Dr. Xiangjun Pu, Dr. Man Chung Wong, Dr. Songhua Cai, Dr. Lukas Rogée, Dr.

Fuyou Liao, Dr. Nicolas Onofrio, Mr. Kin Ping Wong, Mr. Duanzijin Liu, Miss Hongye Chen, Miss Qi Qi, Miss Jingya Yu.

I want to thank my grandmother (I am sorry I could not say goodbye to you due to the coronavirus) and my parents for their unconditional support and encouragement. Finally, I want to thank myself, and please never lose your positivity, curiosity, and courage in the days ahead.

Table of Contents

Lists of Figures

Lists of Tables

Chapter 1 Introduction

1.1 Background and development of Li-S batteries

Facing fossil fuels' shortage and environmental pollution, rechargeable batteries are regarded as clean and sustainable development energy that can address our dependency on fossil fuels.[1-3] Lithium-ion batteries (LIBs) were first commercialized in 1991 and are now used in the portable power supply market and electric vehicles.[4] The increasing energy market urges high energy density and low-cost rechargeable battery systems. However, the specific energy limitation of electrode materials for lithium-ion batteries prevents them from becoming high-energy-density batteries.[3] Li-S batteries have been expected to replace state-of-the-art lithium-ion batteries to be the next-generation energy storage system because they offer a number of advantages, including the abundance of sulfur stock, high theoretical gravimetric energy density, and volumetric energy density (Figure 1.1).[5]

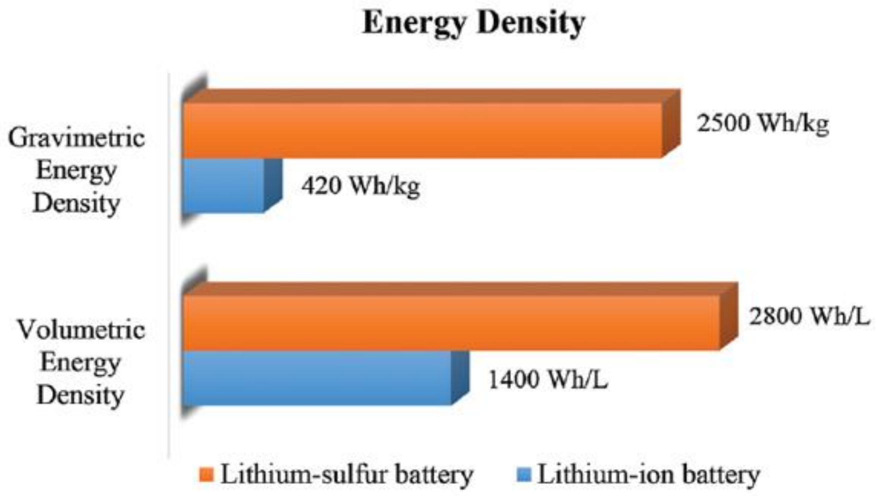

Figure 1.1 The energy density comparison between Li-ion batteries (graphite anode and $LiNi_{1/3}Mn_{1/3}Co_{1/3}O_2$ cathodes) and Li-S batteries.[1]

Since 2009, Nazar *et al*.[6] introduced conductive CMK-3 porous carbon as the host for sulfur and the battery attained a satisfied discharge capacity with more than 20 cycles. The Li-S batteries ushered in rapid development. Li-S batteries have different working mechanisms compared to lithium-ion batteries, the former is based on the sulfur conversion on the cathode and lithium plating/ striping on the anode, and the latter is operated based on the intercalation/deintercalation of lithium-ion.

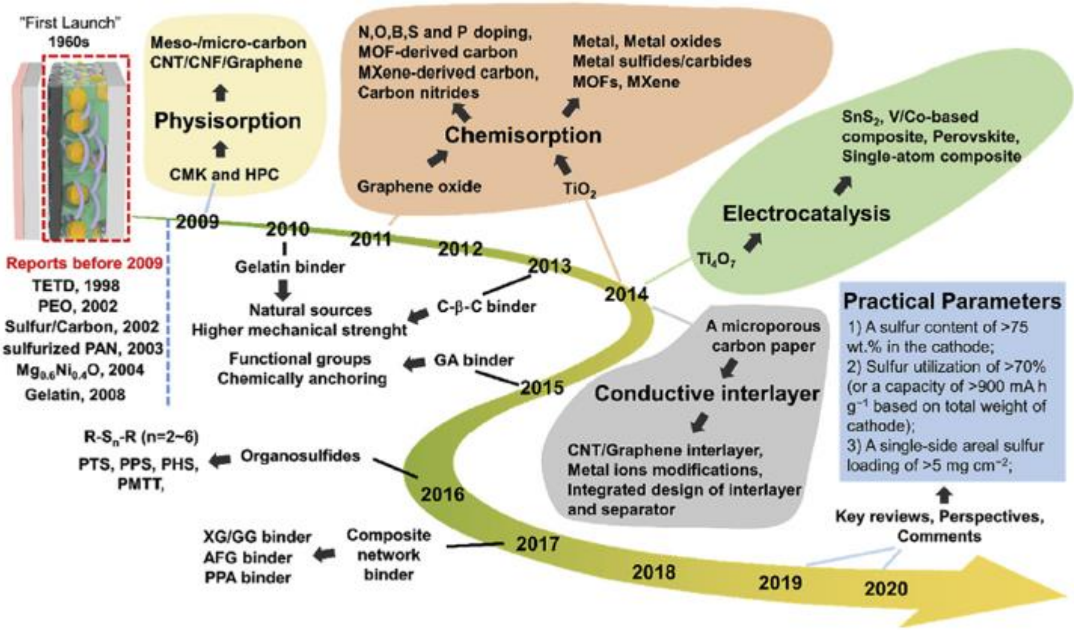

Figure 1.2 The development of strategies for Li-S batteries.[7]

Figure 1.2 depicts the strategies that have been developed to achieve practical lithium-sulfur batteries from 2009 to 2020, such as the evolution of cathode design from initial porous carbon to catalyst design.[7] After decades of hard work, many effective strategies have been promoted to improve electrochemical performance. The specific capacity, cycle stability, and rate performance of Li-S batteries have greatly improved. According to the latest report, the Li-S batteries can stable cycle over 2000,[8,9] and operate at ultra-high rates of 40C,[10] and display a high discharging capacity of 1200 mAh g^{-1} at 1C.[11,12] Although these data are attractive, there is still a huge gap between the laboratory level and the commercial. Many problems exist that need to be addressed for practical Li-S batteries.

1.2 Reaction mechanism in a typical lithium-sulfur batteries

Li-S batteries operate based on the electrochemical reaction of lithium and sulfur: $2Li+S \rightarrow Li_2S$. The actual discharging/charging processes of Li-S batteries are multi-step electrochemical reactions involving phase transitions (Figure 1.3a).[2] The discharging process is divided into four regions, and the related reaction equations are listed as follows:

Step I:

$$S_8(s)+2Li^+ \longrightarrow Li_2S_8(l) \tag{1}$$

Step II:

$$Li_2S_8(l)+2Li^+ \longrightarrow Li_2S_6(l) \tag{2}$$

$$Li_2S_6(l)+2Li^+ \longrightarrow Li_2S_4(l) \tag{3}$$

Step III:

$$Li_2S_4(l)+2Li^+ \longrightarrow Li_2S_2(s) \tag{4}$$

$$Li_2S_4(l)+2Li^+ \longrightarrow Li_2S(s) \tag{5}$$

Step IV:

$$Li_2S_2(s)+2Li^+ \longrightarrow Li_2S(s) \tag{6}$$

In Step I, the solid sulfur is lithiated to the soluble long-chain lithium polysulfides (LiPSs) and contributes to the first plateau (~2.35V). In Region II, the long-chain LiPSs are reduced to the short-chain LiPSs. The step only involves liquid phase conversion, leading to relatively fast reaction kinetics. The second plateau comes from Steps III and IV, and the soluble LiPSs are reduced to insoluble Li_2S_2/Li_2S. Steps III and IV devote 75% theoretical capacity (1254 mAh g^{-1}), regarded as rate-limiting processes.

In the charging process, the reaction steps are opposite to the charging process with two overlapping voltage regions, as shown in the cyclic voltammogram in Figure 1.3b. Moreover, an overpotential is needed for the Li_2S decomposition.

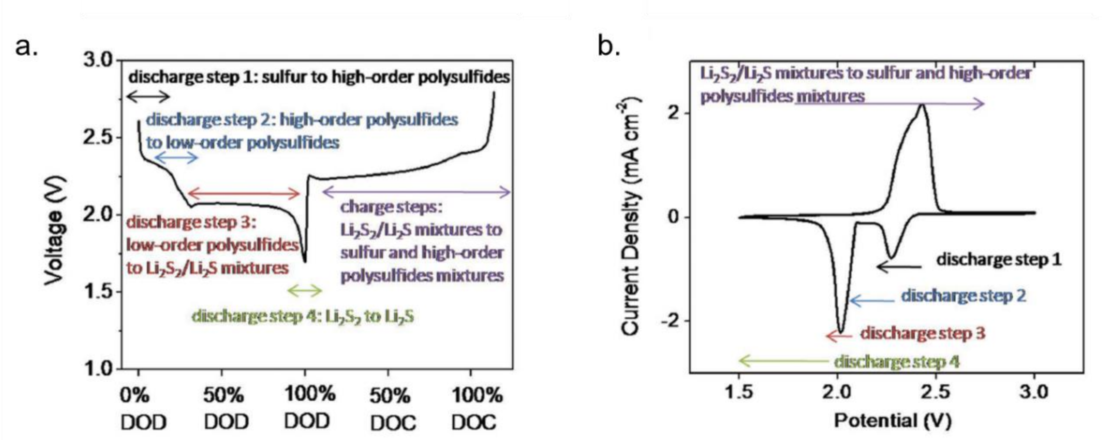

Figure 1.3 a. The charging and discharging profile of typical Li-S batteries. b. The cyclic voltammogram of typical Li-S batteries.[2]

Besides the electrochemical reaction, some chemical reactions occur in the charging and discharging process, which is potential-independent, such as the disproportionation of soluble LiPSs as shown below:

$$S_8^{4-} \longrightarrow 2S_4^{-} \tag{7}$$

$$S_8^{2-} \longrightarrow S_6^{2-} + 1/4S_8(\text{DMSO}) \tag{8}$$

$$S_6^{2-} \leftrightarrow 2S_3^{\cdot -}(\text{DMSO}) \tag{9}$$

$$2S_4^{2-} \rightarrow \frac{6}{7}S_8^{2-} + \frac{8}{7}S_1^{2-} \tag{10}$$

Combining the electrochemical reaction equation, we can find that the real reaction mechanism of Li-S batteries is very complex. In addition, the actual reaction process of

Li-S batteries is still being explored. Recently, Wang *et al.*[13] proposed that Li_2S_4 is reduced to Li_2S_2-Li_2S at an invariable ratio of 1:4, and the continuous formation of Li_2S_2-Li_2S solid discharge products comes from a self-catalytic process in practical conditions. Besides, liquid sulfur formation on some specific substrate has been observed in the charging process.[14] By means of *in situ*/ *ex situ* characterizations can help us comprehensively and deeply understand the actual reaction mechanism of Li-S batteries in the future.

1.2.1 Redox reaction between sulfur and lithium polysulfides

In Step I, the redox reaction between sulfur and LiPSs involves phase transition. During the discharge process, cyclo-S_8 is opened and reduced to the long-chain LiPSs and attributes the first discharge plateau (~ 2.34 V) with ~12.5% (209 mAh g^{-1}) theoretical capacity.[1] The discharge capacity is usually lower than the theoretical capacity because partial sulfur may have self-discharge and dissolve in electrolytes.[15] It is worth noting that the charging product sulfur is not the original orthorhombic α-sulfur but is found in the monoclinic β-sulfur.[16] The stable temperature for the β-sulfur existing is above 114 ~119 °C, but it can be generated though electrochemical at room temperature in Li-S batteries. Another interesting phenomenon has been reported: liquid sulfur can be generated from polysulfide electrochemical oxidation at room temperature on metal-containing electrodes.[14] They also found that liquid sulfur can generate on the basal plane of 2D materials (such as graphite, molybdenum disulfide (MoS_2)).[17] However, on the thick 2D materials the liquid sulfur quickly transfers to β-sulfur once is touched by a solid sulfur crystal as shown in Figure 1.4a, which illustrates that β-sulfur is more stable than liquid sulfur in this system. The reason for the liquid sulfur generation from the electrochemical pathway is possible that the relative free energy between LiPSs and sulfur has been changed by the electrochemical potential.[14] The formation of liquid sulfur is shown to be substrate-dependent, and no sulfur droplets are formed on glassy carbon substrates, graphene-nickel foams, and commercial carbon-coated aluminum.[14,18] Due to the fast reaction kinetics, high mobility and reshaping ability of liquid sulfur, it exhibits a higher capacity than the solid sulfur in the same charge condition.[17] Liquid sulfur allows the conversion of the sulfur and LiPSs to form a solid/liquid reaction to a liquid/liquid reaction, which can be applied to flow and fast-charging batteries.

1.2.2 Redox reaction between lithium polysulfides

In Step II, long-chain LiPSs are continued to be reduced to short-chain LiPSs (Li_2S_x, $2<x\leq6$, as shown in Figure 1.3a), and the voltage gradually decreases with further oxidation of LiPSs.[19] At the end of this stage, the viscosity of the electrolyte arrives a maximum, and the major intermediate product is S_4^{2-}.[20] This step is a single-phase reaction only involving liquid-liquid conversion (equation (2)) and has fast reaction kinetics. The properties of electrolytes (such as solution viscosity, solubility to LiPSs) will affect the kinetics.[21] In addition, the electrolyte type affects the reaction pathway, like most of the high donor number (DN) solvents, which can provide a stable environment to generate main intermediate products $S_3^{\cdot-}$ radical.[20] The solubility of Li_2S_4 is very low in the DOL(Dioxolane)/DME(Dimethoxyethane) electrolyte (the solubility of Li_2S_4 is smaller than 0.1 mol L^{-1}). Therefore, premature Li_2S_4 may occur

during discharging, as shown in Figure 1.4b.[22] The plateau ~2.157V (thermodynamic curve) comes from the deposition of Li_2S_4. Li_2S_4 deposition has a slow kinetic and displays thermal dynamic control.

The LiPSs are thought to bring favorable and unfavorable consequences to the reaction process. LiPSs lose contact with the cathode surface due to concentration gradient and diffusion to the separator and anode, resulting in irreversible loss of active material. Moreover, the long-chain LiPSs shuttle to the anode and are lithiated to form short-chain LiPSs, and then the short-chain LiPSs return to the cathode to be re-oxidized, which leads to low Coulombic efficiency and self-discharge. Severe capacity fading and low sulfur utilization are caused by the shuttle of LiPSs.[23] Nevertheless, LiPSs also play an important role in improving the reaction kinetic and efficiently employing the sulfur cathode. LiPSs are beneficial to react with insulating sulfur and to make the internal sulfur in the bulk sulfur have the opportunity to be oxidized, thereby improving the utilization of sulfur (Figure 1.4c).[23,24] The similar reaction also occurs in the charging process; the LiPSs will react with Li_2S to decrease the Li_2S decomposition barrier.

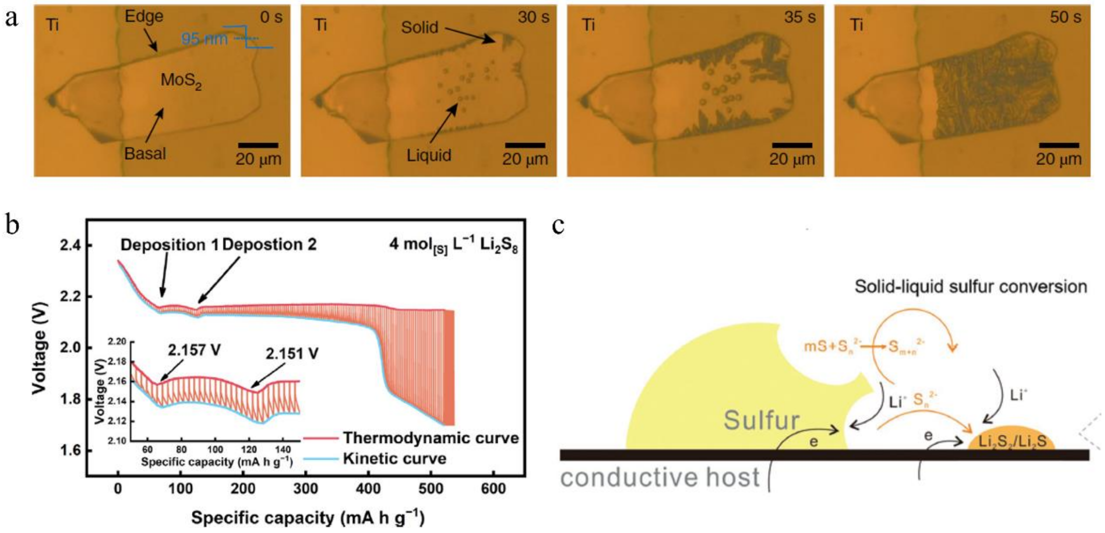

Figure 1.4 a. The optical photos of sulfur generation on the thick MoS_2 flake.[17] b. The GITT curve of Li_2S_8 conversion to Li_2S.[22] c. Schematic of lithium polysulfides react with insulation sulfur and Li_2S_2/Li_2S.[24]

1.2.3 Redox reaction between polysulfides to Li_2S

The Step III and IV of LPSs to solid Li_2S_2/Li_2S is regarded as a kinetic-limited step and attributes three-fourth theoretical capacity (that is, 1254 mAh g^{-1}) as well as the second discharging plateau (~2.15V). A voltage drop at the beginning of the second stage has been recognized as the nucleation overpotential for forming Li_2S, as shown in Figure 1.3a. The overpotential becomes prominent in a practical condition (high loading and lean electrolyte) even at a relatively small current density (0.12C), as shown in Figure 1.5a.[13] Besides, the rate capability and cyclability also turn unsatisfied. These problems are from high LiPS concentration, resulting in sluggish Li_2S deposition. Therefore, to alleviate the potentially limited step, introducing a catalyst can help Li_2S_2/Li_2S deposition Figure 1.5b. Most of the research recently focused on the catalyst design because the catalysts with absorption-catalytic ability can suppress the shuttle effect and improve the reaction kinetics, especially the Li_2S deposition.[25-27]

There is no consensus on how high concentrations of LiPSs lead to slow Li_2S deposition. Recently, Huang *et al.*[28] through electrochemical impedance spectroscopy, combined the galvanostatic intermittent titration technique (EIS−GITT) method to figure out the key kinetic limiting factor in the practical condition of Li-S batteries. During the charging process, the thermodynamic and kinetic voltage curves at different electrolyte/sulfur (E/S) ratios almost overlap, indicating that the E/S ratio has a limited influence on charging kinetics. Besides, the E/S ratio also influences little about the Lithium anode. In the discharging process, the kinetic polarization significantly increases with decreasing E/S ratio. They decoupled the polarization (η_{total}) to activation polarization(η_{ac}), the interfacial charge transfer decides η_{ac} and can reflect the activation energy needed for the Li_2S deposition; concentration polarization (η_{com}), η_{com} is influenced by the diffusion ability of the species involved in the reaction and arises from the difference in concentration of reacting species between the bulk electrolyte and the electrode surface; and Ohmic polarization (η_{ohm}) is induced by the applied current and the electrolyte ohmic resistance, and caused by the ion conduction in the bulk electrolyte (voltage loss) as shown in Figure 1.5c. Based on the analysis of the change of η_{ac}, $\eta_{com,}$ and η_{ohm} with the depth of discharge at different E/S ratios. They suggested that the η_{ac} at the Li_2S deposition stage is the major kinetic limitation in practical conditions (Figure 1.5d). Besides, the η_{con} also accounts for a high percentage in the η_{total} in the Li_2S nucleation and growth process, representing the high LiPS concentration that led to a low interfacial charge transfer and low LiPS diffusion kinetics. However, the η_{con} displays less sensitive to E/S ratio.

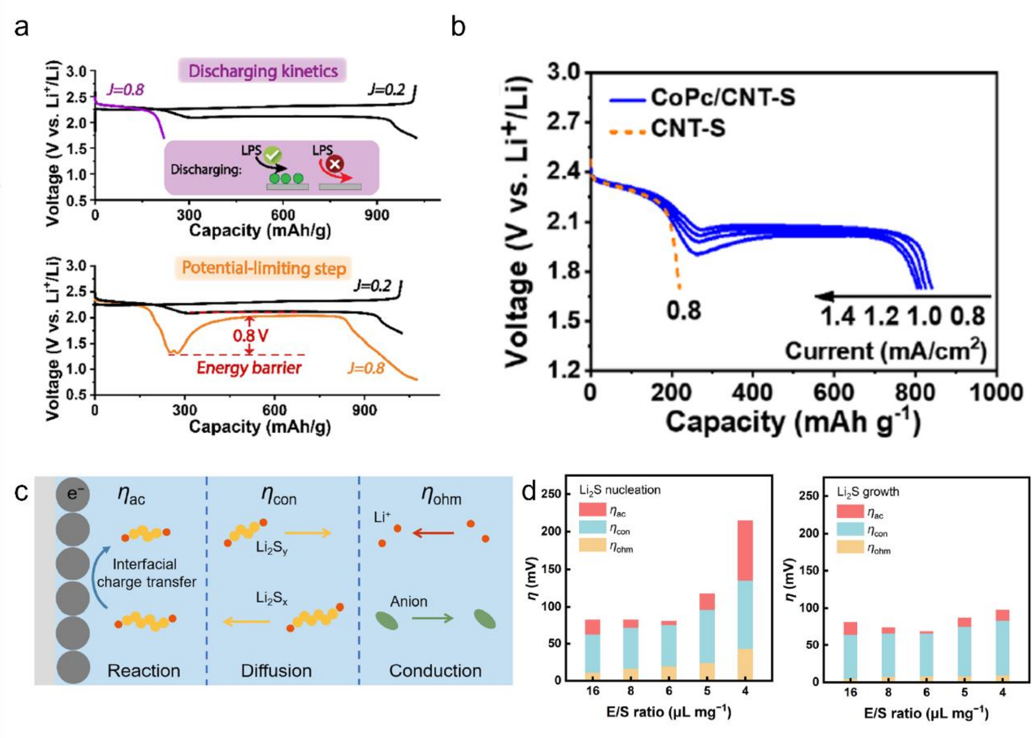

Figure 1.5 a. Schematic of the high energy barrier for Li_2S deposition in a practical condition. b. The alleviation of energy barrier through introducing catalyst.[13] c. Schematic of three kinds of polarization in Li-S batteries. d. The percentage of different polarization in total polarization in Li_2S nucleation and Li_2S growth process.[28]

1.3 The challenges of lithium-sulfur batteries

Working Li-S batteries involves multi-step reactions and phases transition, so the complex process leads to many issues. The challenges of sulfur cathode are listed as follows:

i. The insulation of S and Li_2S: the electrical conductivity of S and Li_2S are 5×10^{-3} S cm^{-1} and 10^{-13} S $cm^{-1,}$ respectively, resulting in sluggish reaction kinetics and low sulfur utilization.[29]

ii. The shuttle effect of soluble LiPSs: the soluble intermediate product LiPSs are cline to diffusion to anode due to the concentration gradient and are reduced to short LiPSs through a chemical reaction, which can diffuse back and be reoxidized electrochemically. Moreover, the diffused LiPSs can be lithiated and deposited on the anode surface as Li_2S_2/Li_2S (Figure 1.6a). The behavior of LiPSs will cause low Coulombic efficiency, self-discharging, active material continuous losing, and anode corrosion, which are regarded as the culprit for the short cycling and fast failure.[24,30]

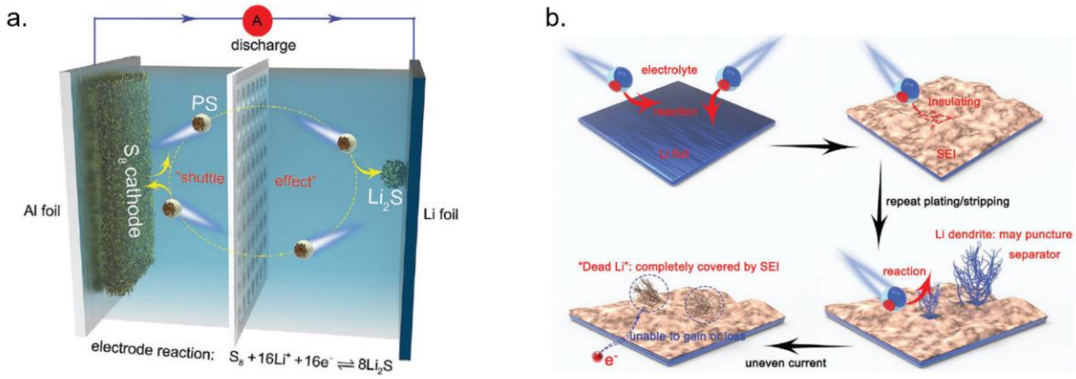

Figure 1.6 a. The schematic illustrates the lithium polysulfide shuttle effect in working Li-S batteries. b. The schematic illustration of the problems arising from Lithium dendrite.[30]

iii. The volume variation during the cycling process: due to the different densities between the S and Li_2S (S: 2.03 g cm^{-3} and Li_2S: 1.66 g cm^{-3}), the volume will expand 80% when S is lithiated to Li_2S. The volume variation will cause a fragile cathode structure, resulting in battery failure.[29]

Besides the problems in the cathode, the dendrite in the lithium metal anode may penetrate the separate, causing internal short circuits(Figure 1.3b); the unstable solid electrolyte interphase on the lithium metal will cause the continuous consumable of electrolyte and lithium metal.[30]

With a deep understanding of the reaction mechanism, different innovation strategies have been proposed for better performance of Li-S batteries. These strategies cover the cathode host design, binder modification, separator optimization, electrolyte improvement, and lithium anode protection. Most of the promotion of Li-S batteries' performance is based on the relatively low sulfur loading (<2.0 mg cm^{-2})[31] and high E/S ratio (> 10 μL mg^{-1}).[32] High E/S ratio systems can dissolve more LiPSs, leading to more attractive specific capacities and bringing about a penalty to energy density.[33] An overestimation of the stability and capacity of the cell will happen in the excess electrolyte environment, leading to the energy density of the cell always being far away from the theoretical value.[34] Today, the development of Li-S batteries towards a decent energy density in practical conditions means the Li-S batteries should have a high sulfur loading and operate in a lean electrolyte condition.[32,35] However, low E/S ratio and high sulfur loading cause the existing problems to become more severe:

i. Sluggish reaction kinetics

A low E/S ratio will bring high soluble LiPSs concentration, increasing viscosity. The large viscosity of the electrolyte leads to reduced ionic conductivity and diffusivity as well as increased interfacial resistance.[3,36] The increasing interfacial resistance negatively influences the charge transfer between the electrode and electrolyte, further affecting the reaction kinetics. Therefore, a low E/S ratio results in sluggish reaction kinetics, which triggers a bad rate performance.

ii. Severe shuttle effect

Due to concentration-driven, the soluble LiPSs will diffuse between the anodes and cathodes to form the shuttle effect. The shuttle effect is regarded as the main reason causing poor cycling efficiencies and low active materials utilization.[37] In the low E/S ration system, a high concentration of LiPSs is unavoidable, hence a more severe shuttle effect and poor electrochemical performance.

iii. Low utilization of active materials

High-loading sulfur requires enough electrode surface to provide the reaction sites. Owing to the limited electrolyte amount, the electrolyte may be unable thoroughly wet the high specific surface of the electrolyte, thereby, the Li-ion transport is impeded and lead to the reaction cannot occur. Besides, Li_2S precipitate faster on the host surface in high sulfur loading and low E/S ratio condition, and the deposition of Li_2S forms a dense passivation layer that hinders ion transport, resulting in low utilization of active materials.[38]

iv. Unstable lithium metal anode

The formation of solid electrolyte interphase (SEI) consumes parts of the electrolyte. In addition, the lithium dendrites growth breaks the formed SEI, and the SEI needs to reform. The electrolyte is easy to be depleted especially in lean electrolyte conditions.[39]

In summary, the development of Li-S batteries still faces many challenges, becoming harsher in high-loading and lean electrolyte conditions. Exploring suitable methods to overcome these problems will pave the way for the practical application of lithium-sulfur batteries.

1.4 *In situ* characterization for Li-S batteries

The multi-step reactions occurring during the cycling process endow a complex reaction mechanism of Li-S batteries. An in-depth and systematic understanding of the reaction mechanism will help to design strategies to address the problems that hinder the practical application of Li-S batteries.[40] Therefore, there are diverse *in situ*/*operando* characterization methods that have been taken to quest understanding the reaction mechanism of Li-S batteries, such as transmission electron microscopy (TEM),[41-45] ultraviolet-visible (UV-vis) absorption spectroscopy,[46-49] Raman Spectroscopy,[50-53] X-ray absorption near-edge structure (XANES),[54-60] and X-ray diffraction (XRD)[15,37,44,57,61-63]. Each characterization has its specific advantage to help researchers learn more about lithium-sulfur batteries. This section will focus on how *in situ* characterizations unveil the reaction process.

1.4.1 X-ray diffraction analysis (XRD)

XRD is an effective protocol to monitor the evolution of sulfur species during cycling, especially for S_8 and sulfur species with crystalline structures.[15,57,64] The evolution of α-sulfur to *β*-sulfur in cycling can be easily detected by the *in situ* XRD. [65,66] Through quantitative analysis, the signal intensity of Li_2S and S will help explore the solid product formation and deposition mechanism.[15] However, LiPSs have remained mysterious in the *in situ* XRD studies until Conder *et al*.[37] found the long-chain LiPSs became visible by adsorption of the glass-fiber separator. The two broad peaks of 25.56° and 28.32°from the long-chain LiPSs appeared after the disappearance of α-sulfur peaks, as shown in Figure 1.7a. The Li_2S_2 is difficult to observe due to thermodynamically unstable in Li-S cells, and it is easy to decompose to Li_2S and LiSPs.[67] Recently, Wang *et al*.[68] directly observed the Li_2S_2 evolution through *operando* XRD on the pouch cell. They found a new peak at ~23.8° at 20% depth of discharge, which was derived from the electrochemical reduction of Li_2S_8: $Li_2S_8 + 2Li^{+} + 2e^{-} \rightarrow Li_2S_6 + Li_2S_2$ (Figure 1.7b). The above discussion demonstrates that *in situ*/*operando* XRD can monitor both the solid-liquid and liquid-liquid reactions during cycling in Li-S batteries.

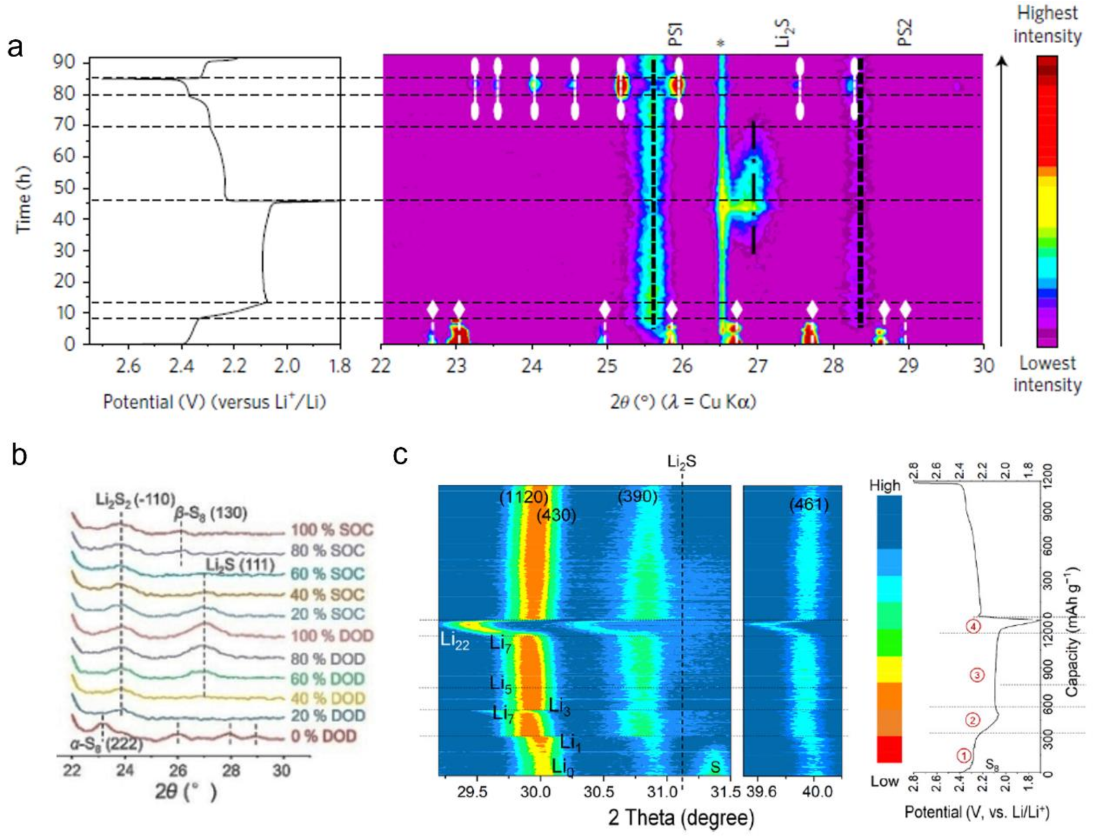

Figure 1.7 a. The *in situ* XRD contour plot with lithium polysulfides signal during Li-S batteries charging and discharging process.[37] b. The *in situ* XRD with Li_2S_2 signal during Li-S batteries charging and discharging process.[68] c. The *in situ* XRD contour plot with NOW catalyst structure variation signal during Li-S batteries charging and discharging process.[69]

By monitoring the signal evolution of sulfur species, *in situ*/*operando* XRD can provide direct observations to assess catalyst performance.[61,69-71] Using *in situ* XRD testing, Qiao *et al.*[69] demonstrated that 2D MoN-VN heterostructures can improve the utilization of active materials by clearly disappearing S signals and appearing Li_2S signals during cycling. In contrast, the signal of α-S_8 peaks can be detected using MoN as the catalyst in the discharge process. These results suggest that heterostructure MoN-VN has a better ability to improve the utilization of active materials and promote the conversion efficiency of sulfur species than MoN. He *et al.*[72] demonstrated the superior catalytic ability of MoB compared to the carbon/sulfur electrode, as confirmed by *in situ* XRD analysis. A strong single of α-S_8 has been detected in the whole discharging process and at the end of the first charging process when using carbon/sulfur as the electrode, which means the low utilization of active materials. In contrast, when MoB was introduced into the cathode, the α-S_8 peak vanished during the initial discharging stage, the Li_2S peak became strong with discharging, and the *β*-sulfur signal appeared at the end of the first charging process. The results indicate that MoB plays an important role in promoting sulfur reduction and Li_2S deposition/decomposition. Manthiram *et al.*[66] reported that the discharging process XRD signal of LiPSs has a noticeable change during the discharging process using graphene oxide (GO)/VS_4 electrode. At the same time, the broad peak of long-chain polysulfides existed without apparent evolution after appearance using the GO electrode. The results indicated that VS_4 could chemically anchor LiPSs and catalyze LiPSs to Li_2S/Li_2S_2.

Catalysts are crucial for Li-S batteries, and *in situ*/*operando* XRD can reveal the catalytic mechanism by studying the evolution of the catalyst. In a study conducted by Wang *et al.*[73], the role of niobium tungsten oxide (NWO) in Li-S batteries was investigated using *in situ* XRD analysis. During the discharging process, the peaks corresponding to NWO shifted towards lower angles, indicating the formation of Li_xNWO (Figure 1.7c). This formation of Li_xNWO proved beneficial for enhancing the conversion efficiency between sulfur species. Li_xNWO exhibited dual functionality by facilitating the transport of Li+ ions and establishing robust chemical interactions with lithium polysulfides (LiPSs). These interactions with LiPSs contributed to the overall improvement in the performance of the Li-S batteries. Likewise, by the *in situ* XRD, Liu *et al*.[74] observed the lithium-ion can insert into TiS_2 to form L_xTiS_2 during the discharging and subsequent extraction of lithium ions from Li_xTiS_2 back to TiS_2 during the charging in the TiS_2/S cathode. The TiS_2 as a multi-functional catalyst can contribute capacity, alleviate the shuttle effect and catalyze the decomposition of Li_2S effectively.

1.4.2 Transmission electron microscopy (TEM)

Both the morphology variation and the corresponding electron diffraction patterns (EDP) during the reaction can be recorded by *in situ* TEM. For Li-S batteries, two kinds of devices are being used to investigate the actual reaction process: solid cell setup and liquid cell setup.[42,75-77] The sulfur easily evaporates due to the heating caused by the electron gun and the high vacuum environment of TEM. The solid setup chose carbon nanotubes (CNTs) as holders to experiment. Kim *et al*.[43] used CNTs with 200 nm inner pores as reaction vessels to observe sulfur evolution in real time by *in situ* TEM. The sulfur was lithiated into nanocrystalline Li_2S without forming lithium polysulfides and Li_2S_2, and the reaction was processed along with the S-in-CNT direction linearly. The interface can be observed clearly between the sulfur and Li_2S, as shown in Figure 1.8a, and the interface exhibits electrical conductivity to facilitate the occurrence of reactions. The S lithiation and Li_2S delithiation in CNTs was also investigated by Wang *et al.*[41] through *in situ* TEM. The evolution of Li_2S includes the initial formation of amorphous and nanocrystalline states and will convert to polycrystalline states as the reaction continues. Compared with the lithiation process, the Li_2S delithiation process requires the synergistic effect of high temperature and electric field to improve the Li-ion diffusion. Moreover, the amorphous and nanocrystalline Li_2S are more favorable in the delithiation process than highly crystallized Li_2S or large grain size Li_2S.

Besides using CNTs as the holder, different materials with sulfur also have been observed through the solid cell setup.[42,44,59,76,78] For example, Xu *et al.*[42] observed the volume expansion of porous carbon nanofiber(CNF)/S during discharging process, Tang *et al.*[76] investigated the sulfur lithiation and lithiation process using MoS_2 encapsulated sulfur nanoparticles (Figure 1.8b), and Wu *et al.*[59] monitored the volume variation during cycling about the porous carbon-encapsulated sulfur.

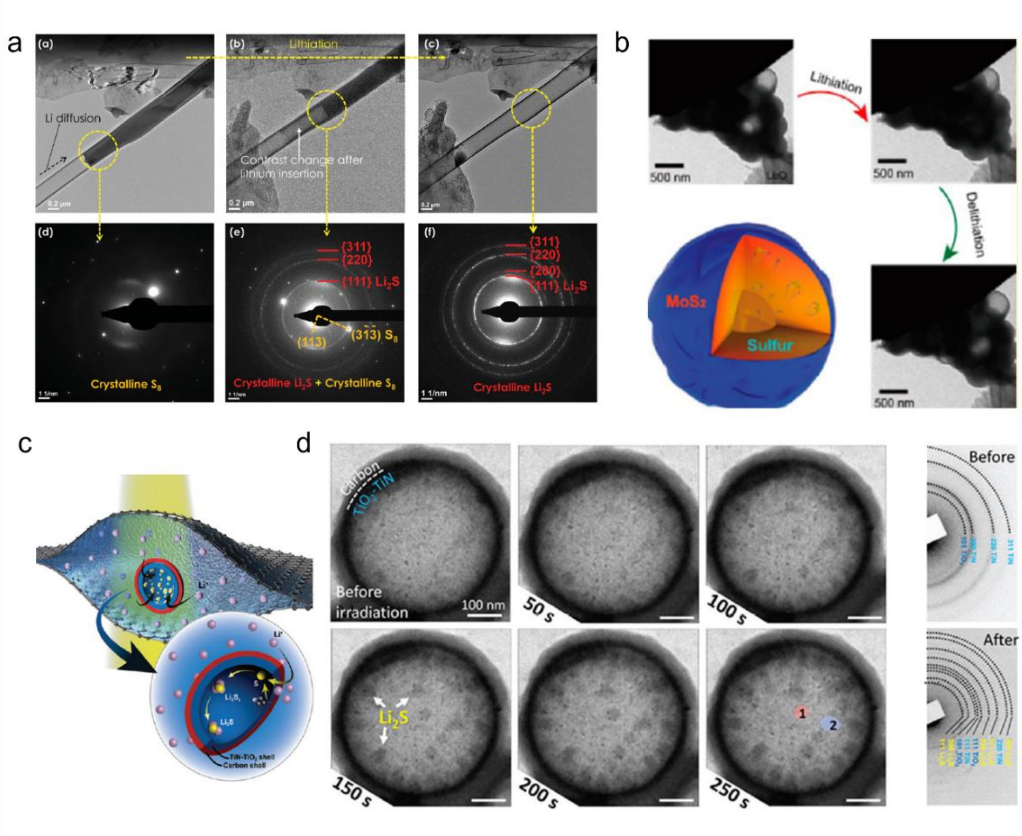

Figure 1.8 a. The *in situ* TEM images of sulfur lithiation process in carbon nanotube.[43] b. The *in situ* TEM images of sulfur lithiation and delithiation process in MoS_2 nanosheet.[76] c. The schematic of graphene liquid battery (GLC)-TEM. d. The *in situ* TEM images of nucleation and growth process of Li_2S in electrolyte.[75]

Liquid cell setup relies on the graphene liquid battery (GLC)-TEM technique, which provides an opportunity to observe the real-time sulfur evolution. The schematic of the cell is shown in Figure 1.8c: the sulfur cathode and electrolyte are enclosed by two graphene layers. The electrons for sulfur reduction come from the electron beam irradiation to irate the chemical lithiation reaction. Cairns *et al*.[77] observed the sulfur lithiation process through the GLC-TEM technique. The TEM results display the uniform growth of Li_2S, and the structure integrity can be preserved during the lithiation process. Xu *et al*.[75] observed the Li_2S nucleation and growth in the C/TiO_2–TiN host, as shown in Figure 1.8d. He claims that the growth of Li_2S follows diffusion control in the initial stage, and when the size reaches 20 nm, the growth is controlled by reaction kinetics.

1.4.3 *In situ* UV–visible spectrophotometry

Differentiating the evolution of soluble polysulfides can be challenging using *in situ* TEM and XRD techniques. The application of *in situ* UV spectroscopy offers a promising approach for both qualitative and quantitative analysis of the polysulfide conversion during cycling. UV-vis can detect the signal of Li_2S_8, Li_2S_6, Li_2S_4, and Li_2S_2 as shown in Figure 1.9a, b, leading to effectively track and characterize the transformation of polysulfides during battery operation to reveal the reaction kinetics.[20,79,80]

Wang *et al.*[68] monitored the variation of Li_2S_8, Li_2S_6, and Li_2S_4 in pouch cells through *in situ* UV-Vis. Analyzing the data, they found that the concentration of Li_2S_6 and Li_2S_4 would decrease at 20% DOD and increase at 60%. They claimed disproportionation reactions of Li_2S_2 arouse this phenomenon (attributed to a high concentration of Li_2S_4) and Li_2S_4 (attributed to a high concentration of Li_2S_6). The concentration of Li_2S_4 is higher than the Li_2S_8 and Li_2S_6, which illustrates the many Li_2S_2 join the disproportionation reaction. Therefore, they suggested that there are lots of Li_2S_2 not converted to Li_2S during cycling. Zou *et al.*[20], through *in situ* UV-Vis, compared the different reaction pathways of Li-S batteries in other electrolytes. In the general ether-based electrolyte (DOL: DME), the Li_2S_4 is the major intermediate product, while the dominant reaction intermediate is light $S_3^{\cdot -}$ radical in DMSO (high-donor number solvent).

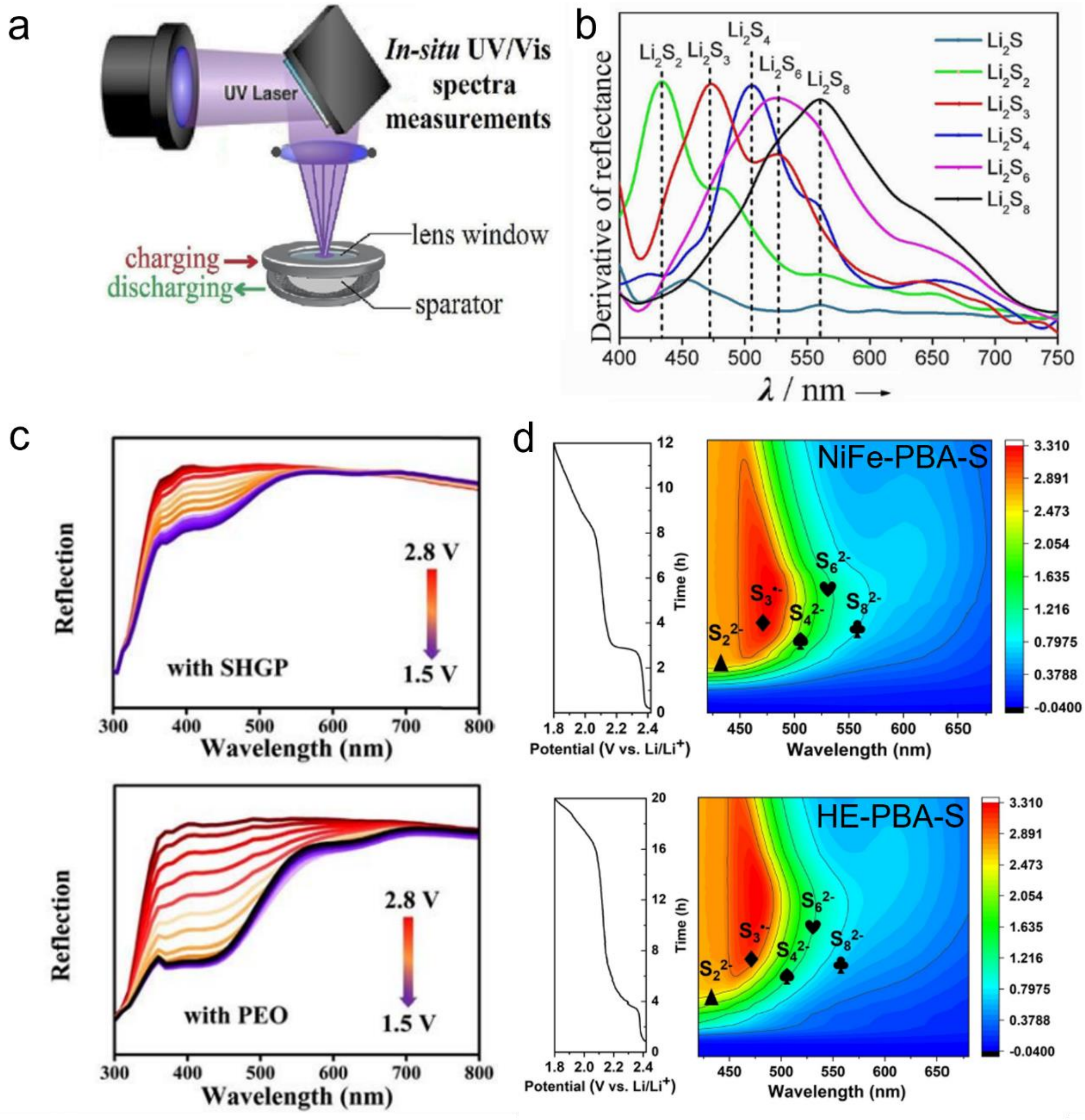

Figure 1.9 a. Schematic of *in situ* UV-Vis to monitor the charging and discharging of a battery. b. The UV-Vis spectra of different LiPSs.[80] c. The UV-Vis spectra comparison between the cell using SHGP electrolyte and PEO electrolyte.[81] d. The UV-Vis spectra comparison.[82]

In situ UV light can demonstrate the efficiency of materials to prevent LiPS diffusion by monitoring the variations of LiPSs. Zhou *et al*.[81] measured the UV-Vis spectra on the anode side to prove that their novel ultra-high ion-conducting gel polymer (SHGP) electrolyte can harness the shuttle effect. As shown in Figure 1.9c, there is an apparent change in the LiPS signal during discharge in a polyethylene oxide electrolyte cell. In contrast, the SHGP electrolyte battery showed a slight change in LiPS concentration at the end of discharge. This comparison demonstrates that SHGP electrolytes can successfully suppress LiPS diffusion. Goodenough *et al.*[47] proved that introducing bis(4-nitrophenyl) carbonate(BNC) as electrolyte additive can prevent LiPSs from dissolving in electrolytes from the *in situ* UV/Vis analysis. The BNC reacts with soluble LiPSs to get insoluble LiPSs, which can limit the LiPSs diffuse to the anode.

The variation of soluble sulfur species also can provide information about the reaction kinetic. Pang *et al.*[82] collected UV/Vis spectra from 420 nm to 680 nm to compare the LiPSs evolution during the discharging process to compare NiFe- Prussian Blue Analogues (PBA) -S and High-Entropy (HE) PBA-S cathode (Figure 1.9d). During the discharging process, the HE-PBA-S electrode attributes a longer discharging time and higher the S_6^{2-} and S_8^{2-} concentration, which demonstrates HE-PBA-S cathode has a greater reaction kinetics than the NiFe-PBA-S cathode. Ni *et al.*[83] also carried out a similar experiment to prove $ZnCo_2O_4$ quantum dots have great catalytic ability through monitoring the concentration variation of LiPSs($S_3^{\cdot-}$, S_6^{2-}, S_8^{2-}) from *in situ* UV-Vis.

1.4.4 *In situ* Raman spectroscopy

Compared to other characterizations, Raman spectroscopy has the specific advantage of exploring the reaction process of Li-S batteries, such as the Raman signal of sulfur (Figure 1.10a) and polysulfides. However, Raman spectroscopy cannot quantitatively analyze different polysulfides due to the overlapping of the polysulfides. *Operando*/*in* *situ* Raman has been widely used to understand the reaction process of Li-S batteries. For example, Abruña *et al.*[83] explored the reaction pathway and kinetics through *operando* confocal Raman microscopy. They analyzed the reduction reactants and intermediates through chronoamperometric measurements (potentiostat). The *in situ* mapping image of sulfur dissolution, polysulfide reduction and sulfur formation (through oxidation of polysulfides) can be attained through *operando* confocal Raman microscopy. Figure 1.10b displays sulfur reduction's spectra and mapping image under a constant potential. According to the mapping information, the reaction rate and the change of the surface area of the sulfur cluster can be established through the expression: $-dA/dt=K_sA^n$, K_s, A, t represent reduction rate of sulfur per active site, sulfur surface area and time respectively. The K_s can be calculated through the expression and K_s display a positive relationship with the overpotential. The reaction rate of the sulfur oxidation from polysulfides and polysulfide reduction also can be obtained through a similar calculation method. Different LiPS behaviors in other electrolytes have been explored by Zaghib *et al.*[84] through *in situ* Raman. The species of LiPSs are the same in 0.5 mol L^{-1} LiTFSI–PY13–FSI (ionic liquid) and 1 mol L^{-1} LiTFSI–DOL–DME. However, the LiPSs reaction kinetic and diffusion are slow due to the large viscosity of ionic electrolytes.

In situ Raman also can be applied to detect the signal of polysulfides. *In situ* Raman data provide compelling evidence in Yao *et al.*[85] work to demonstrate TiO_2-TiN catalytic and absorption ability of LiPSs through observing the signal of S^{6-} in the electrolyte. Chen *et al.*[86] monitored the Raman signal of LiPSs by *in situ* Raman to display their P-doped $NiTe_2$ with Te-Vacancies decorated separator can suppress the shuttle effect. Similarly, the weak signal about LiPSs during the charging and discharging process illustrated S/CNT-CoP with P vacancies cathode can more efficiently absorb the lithium polysulfides than the S/CNT-CoP cathode.[86]

Raman signal is from the vibration of molecules, so they have been used to explore the mechanisms of catalyst in the reaction. Yang *et al*.[50] monitored the catalyst, In_2O_3, Raman signal variation during the cycling through *in situ* Raman, as shown in Figure 1.10c. The Raman peak of In_2O_3 (134 and 310 cm^{-1}) disappears after 1.95 V and a new peak at 288 cm^{-1} emerges due to the formation of the LiInS catalyst. Besides the catalyst change during the cycling, the signal variation of LiPSs and sulfur also demonstrates the In_2O_3 can decrease the kinetic from the sulfur (sulfur signal disappears after 2.04 V with In_2O_3 and 2.20 V without In_2O_3) to polysulfides and improve the Li_2S deposition kinetic (more strong signal of LiPSs with In_2O_3).

In summary, researchers have developed *in situ* characterization techniques to gain deep insights into different aspects of Li-S batteries. These techniques, such as *in situ* XRD, TEM, and UV-Vis, allow for the detailed examination of phase transformations, metal polysulfide migration, and preserving active materials with catalysts in Li-S batteries. Though I only discussed the *operando*/*in situ* XRD, TEM, UV-Vis, and Raman spectrum in this section, other characterizations also have been applied in depth to understand Li-S batteries. **Table 1.1** lists some representative *in situ*/*operando* techniques. It is believed that combining the advantages of different technologies, it is possible to resolve the puzzle about the redox mechanism of lithium-sulfur batteries.

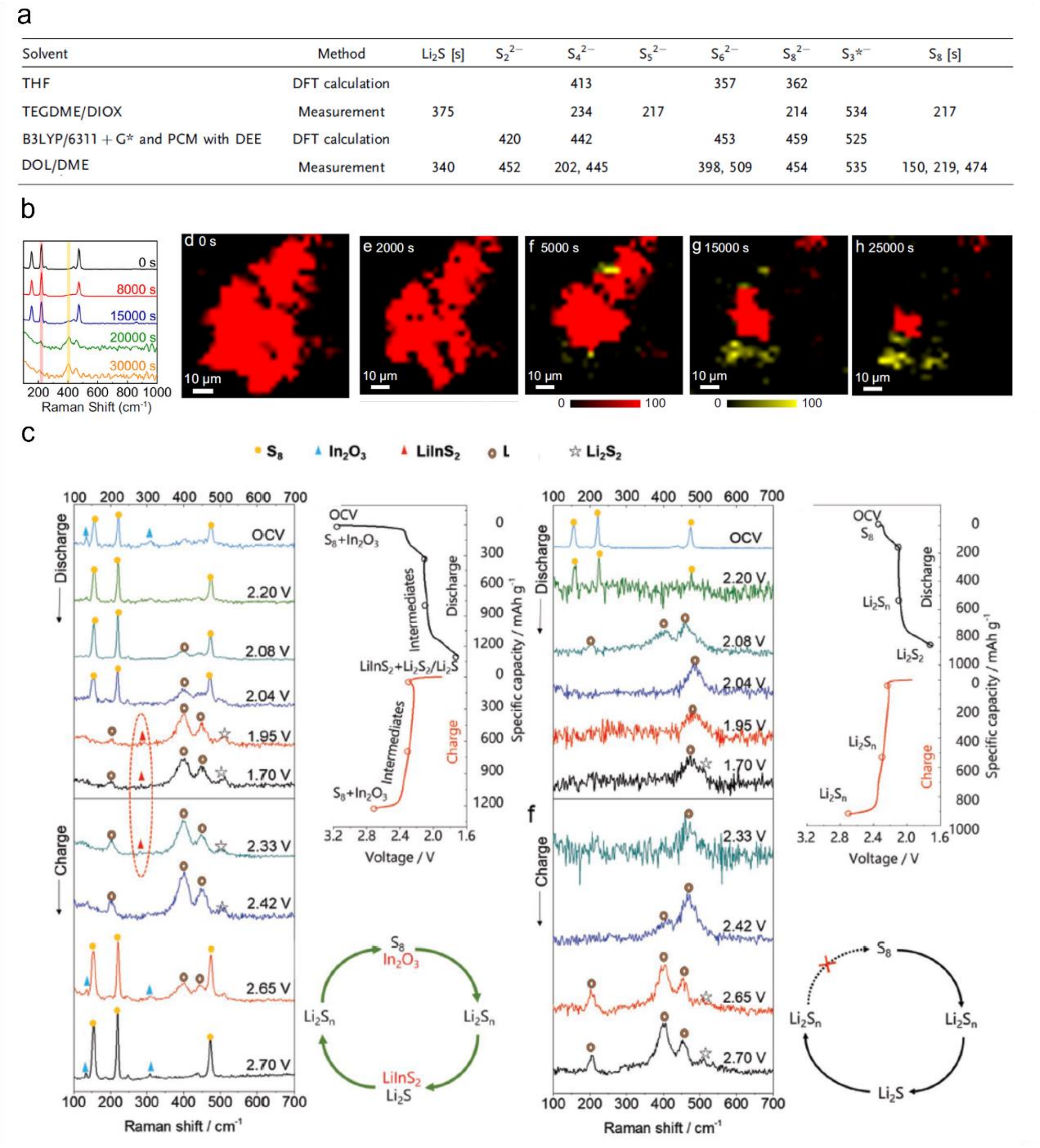

Solvent	Method	Li_2S [s]	S_2^{2-}	S_4^{2-}	S_5^{2-}	S_6^{2-}	S_8^{2-}	S_3^{*-}	S_8 [s]
THF	DFT calculation			413		357	362		
TEGDME/DIOX	Measurement	375		234	217		214	534	217
B3LYP/6311 + G* and PCM with DEE	DFT calculation		420	442		453	459	525	
DOL/DME	Measurement	340	452	202, 445		398, 509	454	535	150, 219, 474

Figure 1.10 a. The Raman signals of sulfur species in different electrolytes.[83] b. The *in situ* Raman and related mapping image of sulfur reduction to LiPSs process. c. The *in situ* Raman spectra of the sulfur cathode with In_2O_3 and without In_2O_3.[86]

Table 1.1 Capabilities, limitations and application examples of *in situ* characterization techniques of Li-S batteries.

In situ techniques	Capabilities	Limitations	Application in Li-S battery study
XRD	Monitoring phase transitions of sulfur species during cycling.	Direct observation of soluble polysulfides by XRD remains	1. Probing sulfur and sulfur species evolution during cycling.[57,87] 2. Provide evidence of the profitable catalytic

		challenging	effect. [61,69-71] 3. Probe the phase evolution of electrocatalysts. [73,74,88]
XANES	Probe S element reduction and oxidation state changes no matter crystal or amorphous, solid or liquid. Monitor the contributions of different sulfur compounds in the cathode during cycling.	X-ray absorption fine structure is affected by the sulfate groups in the salt or the solvent	1. Study the capacity degradation mechanism.[89] 2. Explore the reaction process and intermediates during the redox process. [54,58] 3. Provide evidence of the profitable catalytic effect. [90,91]
XPS	Study chemical composition, charge transfer, chemical bond in the surface.	The cell design is complex	1. Analysis interfaces of electrode and electrolyte.[92,93] 2. Provide evidence of the profitable catalytic effect. (semi-*in situ* XPS)[94]
NMR	Monitor changes in the chemical structure which involves detection radio-frequency. Quantitative tracking of the species concentration.	The experiment setup is expensive. The resolution hard below 100 μm. The alternating currents in the EC and NMR existing interferences.	Explore the reaction process.
Raman	Monitor the compositional and structural changes of sulfur species /related species in the electrolyte or the surface of the electrode.	Hard detect the signal of low-concentration soluble polysulfides.	1. Explore the reaction process. [83] 2. Provide evidence to the profitable catalytic. [85,86] 3. Identify reaction intermediates in the electrolyte.[52] 4. Provide evidence to suppress the shuttle effect.[95,96]
UV-vis	Monitor the evolution of soluble polysulfides qualitatively and quantitatively	Limited detection of solid metal sulfides and cannot be applied in solid-state batteries as well as carbonate-based electrolytes.	1. Exploration of the conversion process between sulfur and sulfur species. [20,79,80] 2. Monitor the shuttle effect.[15-18]
FTIR	Detect the chemical information of surface species	The reflective is quite low for the conductive carbon additives	1. detect polysulfides and electrolyte interactions.[97] 2. quantify the order and concentration of soluble LiPSs in the electrolyte during cycling.[98]
AFM	Observe surface morphology and structure	The large volume change may make trackable features in the topography unrecognizable	Observe the interfacial evolution of electrode/electrolyte.[99,100]
TEM	1. Morphologies change of solid sulfur and metal sulfides. 2. Phase change and chemical composition transformations.	1. Open-cell setups cannot be applied in liquid electrolyte systems. 2. The lithiated process of graphene liquid cell is ignited by electron beam, cannot achieve the cycling process.	1. Monitor the chemical composition transformation and volume expansion of the lithiation/delithiation process. [42,75-77] 2. Observe the nucleation and growth of metal sulfides.[77,75]

1.5 Liquid sulfur in Li-S batteries

1.5.1 Basic knowledge about liquid sulfur

At room temperature, sulfur usually exists as a solid. The melting point of sulfur is 115.21 °C generally, liquid sulfur is only stable above this temperature. The chemistry in liquid sulfur has been proposed as following (R represents ring and C represent diradical chain):[101]

Ring opening:

$$S_8^R \rightleftharpoons S_8^C \tag{11}$$

Chain dissociation:

$$S_n^C \rightleftharpoons S_i^C + S_j^C \tag{12}$$

Ring addition:

$$S_i^C + S_8^R \rightleftharpoons S_j^C \tag{13}$$

Radical displacement:

$$\text{-}S_i^{\cdot} \pm S\text{-}S\text{-} \rightleftharpoons \text{-}S_i\text{-}S^{\cdot} \tag{14}$$

These reactions demonstrate the existence of ring sulfur, chain sulfur, and diradicalic sulfur in liquid sulfur. The physical state of the sulfur can be identified by Raman spectroscopy due to the strong Raman scattering intensity of S-S bonds.

1.5.2 Liquid sulfur in Li-S batteries

Researchers found an abnormal phenomenon during the charging process by optical microscopy, the liquid sulfur can be stable generated on some specific substrate (like Au, Ni) under the melting temperature.[14] The generation of liquid sulfur display substrate dependence and they can form on some specific substrate like indium tin oxide (ITO), Ni and CoS_2 while only solid sulfur on glassy carbon. Liquid sulfur also can be generated on the basal plane of 2D (like MoS_2, WS_2, $MoSe_2$) materials but can be solidified into solid sulfur by contact of solid sulfur which is growing from edge.[17] The large polarization of the edge is regarded as the major problem inducing the nucleation of solid sulfur. Through deposition Ti around the edge of MoS_2, the areal capacity can be compared through controlling the physical state of sulfur. Liquid sulfur displays a large areal capacity compared to solid sulfur owing to its reshaping ability. Cui et al. observed the sulfur generation on three different substrates, Al, carbon and Ni to establish the correlation between battery performance and physical state of sulfur.[18] Compared with Al and carbon, Ni can not only support the Li_2S decomposition but also benefit liquid sulfur generation. Therefore, Ni substrate displays great electrochemical performance and cycling stability. The research about liquid sulfur is still in the very initial stages and there are many unexplored areas of liquid sulfur in the Li-S battery system.

1.6 Objectives and outline

Liquid sulfur has been observed in an optical cell through optical microscopy and *in situ* Raman spectroscopy in Li-S batteries.[18,102] The ability of liquid sulfur to reshape and the lower energy barrier of liquid-to-liquid conversion are specific advantages of liquid sulfur in Li-S battery systems. However, research on liquid sulfur is limited. This thesis focuses on the study of liquid sulfur in Li-S batteries and the objectives are listed:

(i) Liquid sulfur can be generated on thick TMD nanoflakes, but preserving it in the charging process is difficult. Explore a general method to keep liquid sulfur in the charging process on thick TMD materials.

(ii) Unveil the role of liquid sulfur in Li-S batteries and utilize its specific advantages in Li-S batteries.

(iii) Study the reaction kinetics of liquid sulfur deposition.

Through understanding their deposition mechanism, growth kinetics, and specific advantages, the role of liquid sulfur in Li-S batteries has been comprehensively discussed. The thesis contents are listed as follows:

Chapter 1: This chapter briefly introduces the reaction mechanism and existing challenges of Li-S batteries. In addition, the *in situ*/*operando* characterization to explore the real reaction process of Li-S batteries has also been summarized.

Chapter 2: The experimental methods used in this thesis are systematically described.

Chapter 3: This section presents a general method to keep liquid sulfur on thick TMD nanoflakes. The mechanism to prevent solid sulfur accumulation on the edge and liquid sulfur growth kinetics are also presented in this chapter.

Chapter 4: The electrochemical generation of liquid sulfur on single graphene has been investigated. This chapter has comprehensively studied the role of liquid sulfur in the charging process and its deposition behavior. A cathode with fast-charging ability was presented.

Chapter 5: In chapter 5, the effects of mass transport and charge transfer on the deposition behavior of liquid sulfur have been investigated.

Chapter 6: This section summarizes the series work about liquid sulfur. Proposed future work includes further exploration of liquid sulfur and the discharge process using optical cells.

Chapter 2 Experimental methods

The main chemicals and reagents for the series work are listed in this chapter. This chapter also describes the characterization of materials' morphology, structure, composition, and main experimental methods. The specific method for each work was listed.

2.1 Chemicals and reagents

All chemicals were used without any purity, and the related information is listed in Table 2.1. The $Si0_2/Si$ wafer (285nm and 300nm) and Si wafer were purchased from Fangdao Semiconductor Co., Ltd.

Table 2.1 The synthesis and measurements involved using various chemicals and reagents.

Chemicals	Purity	Company
Molybdenum disulfide (MoS_2) crystal	/	6Carbon Technology (Shenzhen)
Molybdenum diselenide ($MoSe_2$) Crystal	/	6Carbon Technology (Shenzhen)
Tungsten disulfide (WS_2) crystal	/	6Carbon Technology (Shenzhen)
single layer graphene on copper	/	6Carbon Technology (Shenzhen)
Polyacrylonitrile (average Mw 150,000)	/	Sigma-Aldrich
Dimethylformamide (DMF)	99.80%	Sigma-Aldrich
Lithium bis(trifluoromethanesulfonyl)imide (LiTFSi)	99.90%	Aladdin
Lithium nitrate ($LiNO_3$)	99.90%	Aladdin
Dioxolane (DOL)	99.80%	Sigma-Aldrich
Dimethoxyethane (DME)	99.50%	Sigma-Aldrich
Li metal (d iameter:16mm; thickness:0.6 μm)	99.95%	China Energy Lithium Co., Ltd

2.2 Material preparation

TMD nanoflakes and H_2-TMD on SiO_2 wafer (work 1)

The MoS_2, $MoSe_2$, and WS_2 flakes were exfoliated by the Scotch tape on 300-nm-thick SiO_2/Si substrate. The samples were then annealed in a 5 % H_2/Ar atmosphere at 600 °C for 10 hours to attain H_2-treated TMD materials.

Graphene transfer(work 2)

The monolayer graphene was transferred to SiO_2/Si wafer through a standard Poly(methyl methacrylate) (PMMA)-based method.[45] The PMMA-coated graphene on a copper substrate (Tanfeng Tech. Inc) was etched through copper etchant (Sigma-Aldrich). Then the PMMA/graphene was washed with DI water several times to remove the residual copper etchant solution. The PMMA/graphene film was transferred to a 300nm SiO_2/Si wafer or TEM grid (Au Quantifoil). Next, the sample was naturally dried in air for the whole night and baked on a hot plate for 1h at 150 °C. Subsequently, the samples were soaked in acetone for 10 mins three times to remove the PMMA layer. Then the sample was washed with IPA and DI water to get the single-layer graphene on SiO_2/Si wafer or TEM grid.

Carbon film on SiO_2 wafer (work 3)

A solution of polyacrylonitrile (PAN) dissolved in N,N-dimethylformamide (DMF) (1 g in 5 ml) was prepared as the precursor. The precursor solution was coated on a SiO2 wafer and heated at 110°C to evaporate the DMF solvent. The samples were then stabilized in air at 230 °C for 3 hours, followed by carbonization at 650 °C, 750 °C, 850 °C, 950 °C, and 1050 °C, respectively.

Preparation of CNFs

The polyacrylonitrile (PAN) (2g) was dissolved in 20 ml dimethylformamide (DMF) to prepare as an electrospinning precursor. The solution was magnetically stirred for a whole night at 80 °C. Then the solution was electrospun at 13.5 KV and the distance between the needle and the current collector was ~10 cm. The electrospinning flow rate was kept at 0.5 ml h^{-1}. After getting the PAN paper, the PAN paper was stabilized at 220 °C for 3 h in the air. Subsequently, the film was carbonized at 1050 °C under the Ar atmosphere with a ramp rate of 3 °C to get the freestanding CNF.

Optical cell fabrication

Figure 2.1 shows the optical device using MoS_2 as a cathode and lithium as an anode. The MoS_2, $MoSe_2$, and WS_2 flakes were exfoliated by the Scotch tape on 300-nm-thick SiO_2/Si substrate. The samples were then annealed in a 5% H_2/Ar atmosphere at 600 °C for 10 hours to attain H_2-treated TMD materials. Photolithography and electron beam deposition prepared titanium electrodes (50-70 nm thick) on the TMD flakes. The device was fixed on a glass slide. Aluminum bonding wires created electric interconnections between the titanium electrodes and copper foil. A glass plate was placed over the two electrodes, and the cover glass was fixed with Kapton tape. Then the following steps were carried in the argon-filled glove box. Lithium metal was pressed onto the copper foil to work as the anode. 0.25M Li_2S_8 catholyte (volume ratio of DOL: DME1:1) with 0.5M LiTFSI and 0.1M $LiNO_3$ can fill the optical cell due to the capillary effect. Finally, vacuum grease (Dow Corning) was used to seal the cell.

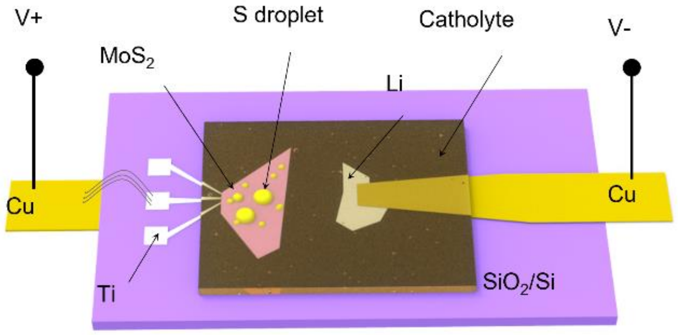

Figure 2.1 The schematic image of the optical cell with MoS$_2$ as cathode and Lithium as anode.

The assembling process for the optical cell using single-layer graphene as the cathode is the same as the optical cell with TMDs as the cathode.

2.3 Characterization methods and sample preparation

Optical microscopy

The main purpose of optical microscopy (Leica Dm 2700M) with a dry-immersion objective (N PLAN L 50x/0,50) was performed to record the videos and images. Videos were recorded at room temperature at 1 frame/second, and images were captured with a resolution of 4.99 megapixels unless otherwise noted.

Raman Spectroscopy and low-temperature testing

The signal of Raman comes from the inelastic light scattering between incident photons and the sample. The Raman spectra of sulfur and LiPSs were collected by Confocal Raman microscopy (alpha300 R, WITec Inc) with 532 nm monochromatic light. The collection time was 10 seconds for every Raman signal. Besides, unless otherwise mentioned, the video resolution is 1.3 megapixels using the 50× objective lens.

The cell was put on a temperature-controlled stage (DSC600) and measured by confocal Raman microscopy. A T96 controller, an LNP95 liquid nitrogen pump, and the linksys32 software controlled the stage temperature. Before cooling down, dry nitrogen was used to purge all air out of the chamber to avoid the influence of water in the air. After starting the low-temperature testing, the liquid nitrogen pump kept working until the experiment finished.

Scanning Electron Microscope (SEM)

The SEM can be used to investigate the morphologies and composition of the sample through a focused beam of electrons. The morphology of materials is being observed by Scanning Electron Microscope (Tescan VEGA3). The chamber was evacuated to a pressure of less than 3 x 10^{-6} torr, and the operating voltage was set to 15 kV.

Transmission electron microscopy (TEM) and scanning transmission electron microscope (STEM)

All TEM and STEM were performed using JEOL JEM-2100F TEM/STEM operated at 200 kV, equipped with a Gatan Enfina electron spectrometer (CA, USA). Both imaging and EELS were carried out under 200 kV accelerating voltage with a 13 mrad convergence angle for the optimal probe condition. Energy dispersion of 0.3 eV per channel and 21 mrad collection angle were set up for electron energy loss spectroscopy (EELS), and high-angle annular dark-field imaging (HAADF) images were acquired with an 89 mrad inner angle simultaneously. Energy-dispersive X-ray spectroscopy (EDS) was acquired with an Oxford INCA detector. After adding the liquid nitrogen into the Dewar, the system was stabilized for at least 40 min before observation to minimize the vibration and operated under ~-175 ^{o}C.

High-angle annular dark-field STEM was used to acquire the atomic arrangement and analyze the materials' composition and electric field. Helios 5CX dual-beam focused ion beam (FIB) system was used to prepare the cross-sectional STEM samples.

Other characterization

X-ray photoelectron spectroscopy (XPS) (Thermo Scientific Nexsa) was used to measure the electronic state of the element. XRD (Rigaku SmartLab) was used to identify the phase. Four Point Probing & Sheet Resistivity was used to test the sheet resistivity.

2.4 Electrochemical measurement

Linear sweep voltammetry measurement

The preparation of cells is the same as for optical cells. The cell was tested from open circuit voltage to 2.8V with a scan rate of scanning rate of 0.3 mV s^{-1}.

Potentiostat testing

The cell was potentiostat charged and galvanostatic discharged using an electrochemical workstation (CHI 760e).

Cycling testing

The electrochemical experiments of the hall cell were tested using a CR2032 coin cell, and all the assembled process was operated in an argon-filled glovebox. The blank electrolyte included 1M LiTFSI and 0.2M $LiNO_3$. The 0.5M Li_2S_8 was prepared by dissolving a proportion of sulfur, Li_2S, in the blank electrolyte. The CNFs (1cm ×1cm) were prepared as cathode, then 10μL 0.5M Li_2S_8 (corresponding to1.28 mg sulfur) was added into CNFs (the mass of the CNFs is ~1.5mg and thickness is ~90 μm); another CNFs paper as an interlayer was placed on the CNFs as cathode and adding another

10μL blank electrolyte. Then, a Celgard separator (2400) with a diameter 19 mm was put on the CNFs. About 10 uL blank electrolyte was added to wet the separator, placing the lithium metal (diameter: 15.6 mm and thickness: 45 μm) on the separator. The G/Ni electrode (1cm ×1cm) was pressed before using it as a cathode. The same procedure was applied to assemble the G/Ni-Li_2S_8-Li cell as previously described, except that there was no interlayer in this cell. For a high-loading battery, we prepared 0.5M Li_2S_8 in DME. The solution was added into CNFs and waited for drying. The loading can be controlled by adjusting the solution amount. Subsequently, the battery was assembled as previously described. The electrolyte consumption for the high-loading testing was 40μL. All the coin cells were tested at room temperature in a voltage range of 1.5V-2.8V and tested more than two times.

2.5 Calculation

The binding energy for TMDs and sulfur (work 1)

DFT calculations have been performed with VASP[103,104] with the Perdew, Burke, and Ernzerhof functional.[105] Based on the rectangular unit cell, simulation cells consist of a single layer of MoS_2 replicated 3×6 (with various S vacancies). We used a 35 Å supercell to ensure no interactions between atoms and periodic images in the direction perpendicular to the surface. To adequately describe vdW interactions between the MoS_2 surface and S8, we used the DFT-D2 correction proposed by Grimme and coworkers[105]. Due to a large number of calculations, we performed only Gamma point calculations and utilized a 400 eV kinetic energy cutoff. All molecular structures were optimized until energy and forces reached a minimum of 10^{-6} eV and 5×10^{-2} eV/Å, respectively. Binding energies were calculated as:

$$E_b = E_{S8@MoSx} - E_{S8} - E_{MoSx} \tag{15}$$

with E_{S8}, E_{MoSx} and $E_{S8@MoSx}$ the energy of the S_8 molecule, defective MoS_2 and S_8 adsorbed on top of MoS_x, respectively.

The binding energy between the different planes of sulfur crystal and sulfur/Li_2S_8 (work 2)

The electronic binding energies were calculated as:

$$E_b = E_{slab+mol} - E_{mol} - E_{slab} \tag{16}$$

E_{slab}, E_{mol} subscript were the energies of the bare beta-sulfur slab without the adsorbed molecules, the energy of the isolated molecule and the energy of the beta-sulfur slab with the molecule adsorbed. According to this definition, a more negative binding energy denotes a more favorable adsorption bond formation.

Surface energy of different planes of the sulfur crystal (work 2)

The surface energies were calculated as follows:

$$E_{surface} = \frac{E_{slab} - nE_{bulk}}{A} \tag{17}$$

where E_{slab}, E_{bulk} and A were the energies of the bare beta-sulfur slab, bulk and total surface area of the slab, respectively. The unit of calculated surface energies was converted to J/m^2.

Electric field simulation (work 1)

Electric field simulations were conducted by the AC/DC physics module of COMSOL Multiphysics. The geometry of the MoS_2 flack was 20 μm × 5 μm × 100 nm. 400nm wide MoO_2 surrounded the MoS_2 flake, so the dimension of H_2 treated MoS_2 was 20.8 μm × 5.8 μm × 100 nm. The MoS_2 or H_2-treated MoS_2 was placed between two electrodes, and the distance between the two electrodes was 50 μm. The ether-based lithium-ion battery electrolyte (as system environment), MoS_2, and MoO_2 are 7, 16[106], and 9.5[107], respectively. The Li anode was grounded, and the Ti cathode was applied constant voltage of 3.0 V, 3.2V, and 3.5V.

Chapter 3 Stable liquid-sulfur generation on transition- metal dichalcogenides toward low- temperature lithium–sulfur batteries

3.1 Introduction

Studies by X-ray diffraction (XRD),[15,108] transmission electron microscopy (TEM)[41,109] and X-ray absorption spectroscopy (XAS)[110] indicate that the Li_2S crystal is oxidized to soluble polysulfides and further to solid sulfur in β phase during the charging process. However, some researchers recently found an unusual phenomenon under *operando* optical microscopy: the charging product (S_8) would be in the liquid phase instead of solid in an electrochemical cell at room temperature.[14] The sulfur droplets obtained through electrochemical reaction far below their melting temperature (155 °C) open new avenues toward high-energy liquid Li-S batteries, electroactive flow devices, and liquid microlensing applications.[102] Simultaneously observing the sulfur growth and electrochemical behaviors, liquid sulfur droplets can induce higher areal capacities than solid sulfur crystals under the same operating conditions due to releasing active sites/substrates by coalescence of sulfur droplets.[17] In addition, the sulfur droplets' fast dynamic and supercooled nature signify possibly fast-charging and low-temperature liquid S-Li batteries.

Nevertheless, Yang *et al.*[17] found that the liquid sulfur generated on the basal plane of two-dimensional (2D) layered materials (*i.e.*, MoS_2) would be solidified by touching solid sulfur crystals, which would grow and propagate from the edge upon charging. As a result, the complete coverage of insulating solid sulfur on MoS_2 stalled the electrochemical reaction. Instead, the strong electric field polarization dominantly caused the edge-induced crystallization on the edge areas of MoS_2 flakes. To eliminate the edge effect, they either conformally covered the MoS_2 edges with titanium/SiO_2 layers or deposited MoS_2 monolayers, which are considerably expensive, elaborative, and infeasible for practical applications. Thus, a significant challenge is to develop efficient strategies or materials to sustain the appealing liquid sulfur for high-performance liquid sulfur-based energy storage technology.

This contribution demonstrates only liquid sulfur generation from delithiation of polysulfides on MoS_2 flakes annealed in an H_2 ambient (designated as H_2-MoS_2). Both optical and Raman spectroscopy observations reveal that the liquid sulfur phase sustains on the basal plane of H_2-MoS_2 without solid sulfur growing from the edge area, even charging the electrochemical system up to 3.5 V *vs.* Li/Li^+. Combined experimental and theoretical investigations elucidate the mechanism of eliminating edge-induced sulfur crystallization. We find that the binding energies between sulfur molecules and H_2-MoS_2 are lower than those for pristine MoS_2, which weakens the local sulfur supersaturation and wettability on the edges, thus suppressing the ordering of S_8 molecules into solid crystals. In addition, the marginal oxidization layer around H_2-MoS_2 plays a considerable role in delocalizing the electric field at the edges upon charging. Quantitatively analyzing the size and number of sulfur droplets with charging time illustrates that the liquid sulfur formation on H_2-MoS_2 follows diffusion-control growth kinetics and droplet-merging growth models. The rapid coalescence of droplets can release the active H_2-MoS_2 surfaces for a further polysulfide redox reaction, resulting in high areal capacities.

In contrast, the systems using pristine MoS_2 substrates present solid sulfur propagation from the edge to the basal area, indicating much lower areal capacities under the same measurement conditions. To demonstrate the universality of this strategy, we further annealed other transition metal dichalcogenides (TMDs) under H_2, which delivers similar growth behaviors: solid sulfur crystals form on pristine TMDs, whereas only liquid sulfur generates on H_2-treated ones. The environmental stability of the liquid sulfur is also investigated by decreasing the charging temperature from 25 °C to -50 °C, where sulfur droplets are still clearly observed on H_2-MoS_2 with remarkable areal capacities, suggesting their promise for extremely low-temperature energy storage applications. This work sheds new light on the mechanism of sulfur formation on transition metal dichalcogenide substrates, which will expedite the development of a broad range of metal-liquid sulfur battery chemistries.

3.2 Results and discussion

3.2.1 Electrochemical generation of sulfur on MoS_2 and H_2-MoS_2

The thick MoS_2 nanosheets (50 -150 nm) were prepared on Si/SiO_2 substrate to get rid of the thickness influence. The MoS_2 was then annealed in an H_2 atmosphere at 600 °C for 10 h before being connected with titanium (Ti) micro-current collectors and sealed with a glass slide cover. It is noted that H_2 annealing effectively tunes the chemical structures and electronic properties of MoS_2.[111] Ti is selected to build the MoS_2 cathode because it is inactive to the sulfur formation, even charging up to 4.0 V.[102] Before applying an external voltage of 2.8 V to drive the electrochemical reactions, the open circuit potential of the micro-device was measured to be ~2.4 V (Figure 3.1a), consistent with that in actual batteries.

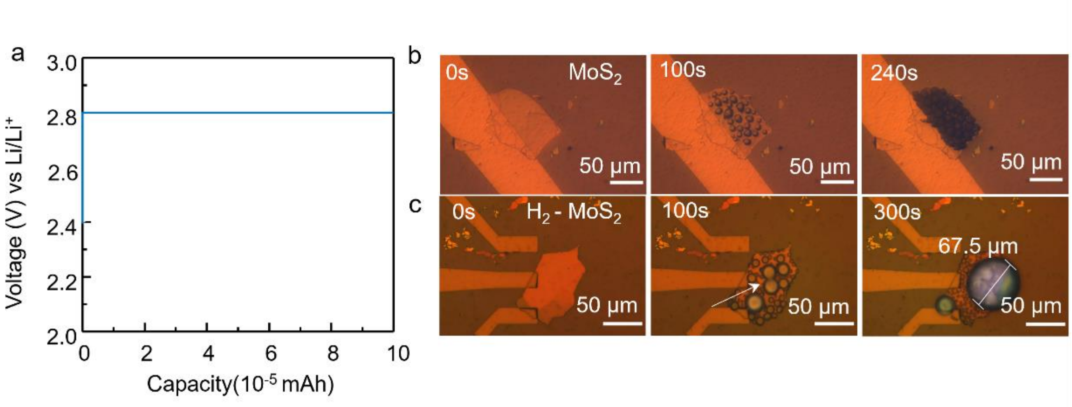

Figure 3.1 a. The open-circuit voltage of the device and the applied constant voltage. b. Sulfur generation on the MoS_2 nanoflakes. c. Sulfur generation on the H_2-MoS_2 flakes.

The *in situ* optical microscopy first observed the electrochemical formation of sulfur on MoS_2 and H_2-MoS_2, as shown in the time-sequential images in Figures 3.1b and c. It is observed that liquid sulfur droplets (in light contrast) nucleated and grew at the beginning and then transferred to the solid phase (in dark contrast, at 120 seconds) once in contact with the solid sulfur generated on the edges of pristine MoS_2. The insulating solid sulfur continued to expand and occupy the entire basal planes by the end of the charging. These observations agree well with the previous studies,[17] indicating the reliability of the electrochemical device in this work. In contrast, the delithiation of polysulfides on H_2-MoS_2, as depicted in Figure 3.1c presents no contrast transition from light to dark of the sulfur product over the whole charging process, implying only liquid sulfur formation. The growth of the sulfur on H_2-MoS_2 is associated with the coalescence of adjacent droplets (as shown by the arrow in Figure 3.1c), releasing the conductive basal plane for additional liquid sulfur formation. This phenomenon will benefit high areal capacities in actual Li-S batteries. The merged sulfur droplet on H_2-MoS_2 can be up to 67.5 µm, approximately five times larger than the 13.6 µm of solid sulfur crystals formed on MoS_2. Such a difference further suggests the preservation of liquid sulfur on H_2-MoS_2 due to the unique reshaping capability of liquid sulfur. In addition, the linear scanning voltammetry (LSV) result demonstrates that the Li_2S_8 conversion to sulfur on the H_2-MoS_2 substrate possesses a smaller overpotential (Figure 3.2) than that of the MoS_2 substrate, which illustrates the higher redox kinetics on H_2-MoS_2.

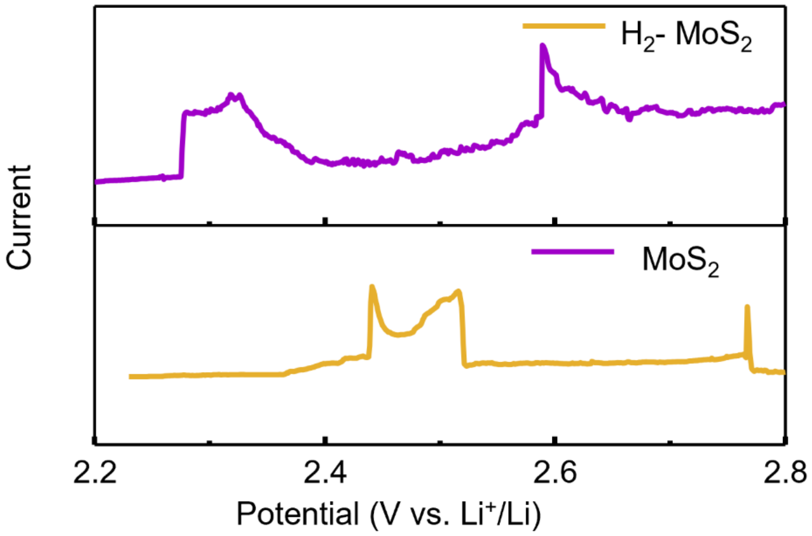

Figure 3.2 LSV curves of Li_2S_8 conversion to sulfur on MoS_{2-x} and MoS_2 substrates.

The *in situ* Raman spectroscopy study was also conducted to confirm the chemical structures of sulfur formed on MoS_2 and H_2-MoS_2, as shown in Figure 3.3. Notable is that the micro-Raman spectrometer possesses sufficient spatial resolution (500 nm) to focus on individual sulfur droplets or particles. For the Raman signatures of sulfur, the internal vibration peaks at 153 cm^{-1}, 220 cm^{-1}, and 473 cm^{-1}, corresponding to the asymmetric vibration, symmetric vibration, and stretching of S-S bonds in the S_8 ring, are independent of the liquid or solid phase of sulfur (Figure 3.3a, b). In the low-frequency region (<100 cm^{-1}), solid β-sulfur and liquid sulfur droplets can be easily distinguished by the widened doublet peaks at 33 cm^{-1} and 42 cm^{-1} for the former and the smooth and Rayleigh wing-like slop for the latter, respectively.[112] It is worth noting that liquid sulfur cannot block the substrate signal (Figure 3.3 b). Thus, the Raman spectra still identify the feature peaks of MoS_2, whereas the Raman signal of MoS_2 is hardly detected for the coverage of solid sulfur. According to these fingerprint features, it is observed that over the whole charging process, only liquid sulfur was detected on the surface of H_2-MoS_2, which is different from the liquid-solid phase transition of the sulfur product on MoS_2 upon charging.

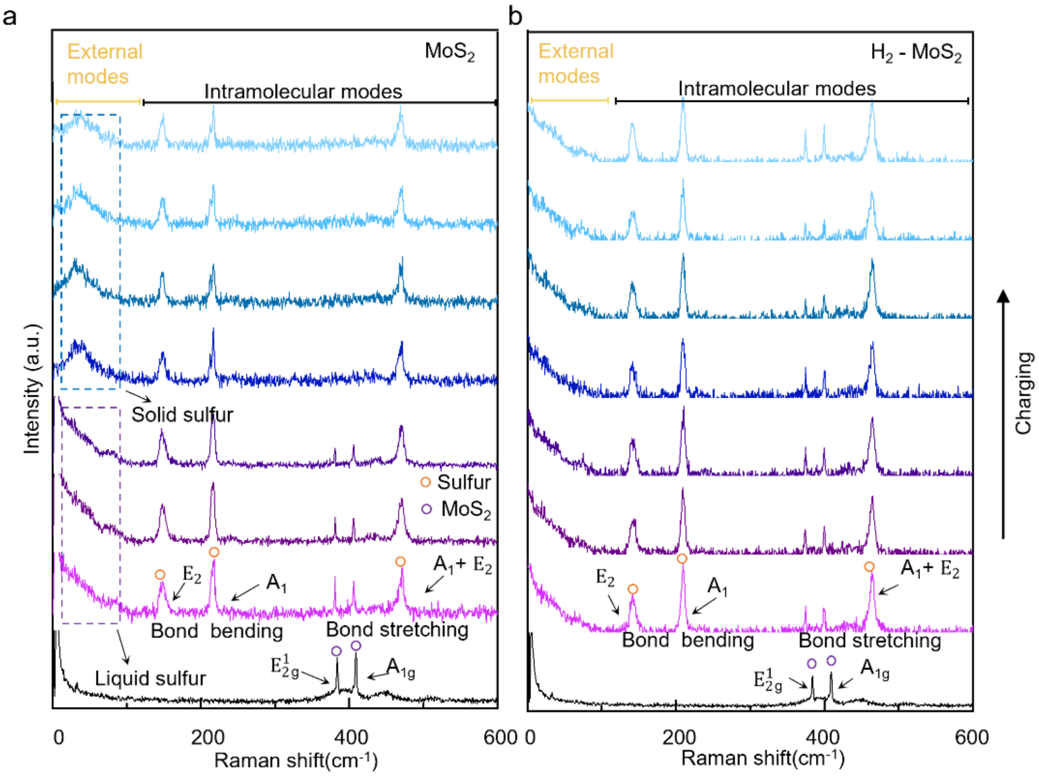

Figure 3.3 a. Evolution of Raman spectra on the pristine MoS_2 (left) and b. the H_2-MoS_2 (right) during charging.

We also conducted *in situ* optical and Raman characterization of the H_2-MoS_2-based electrochemical cells under different overpotentials of 3.0 V, 3.2 V, and 3.5 V (see details in Figure 3.4). All the samples present solitary formation of liquid sulfur during the whole charging process, suggesting the overpotential independent nature of the liquid sulfur generation on H_2-MoS_2.

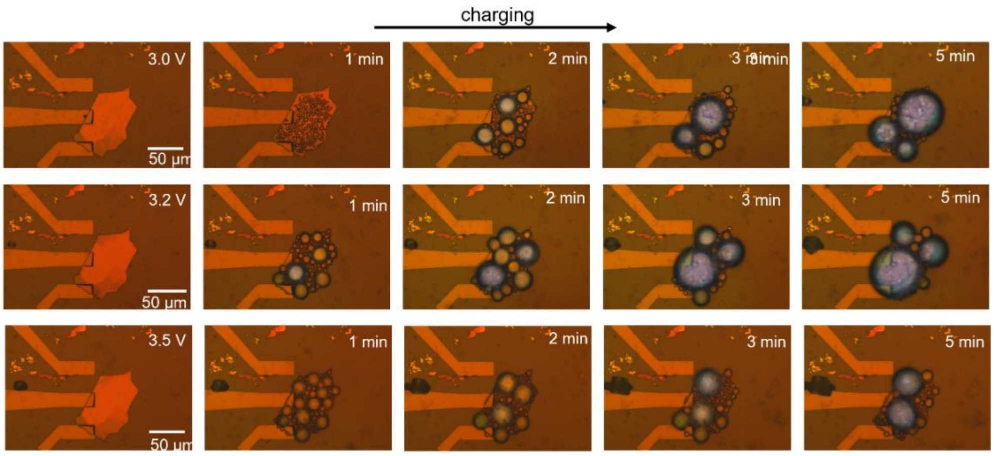

Figure 3.4 Liquid sulfur generation on the H_2-MoS_2 at 3.0, 3.2, and 3.5 V.

In order to demonstrate the universality of the liquid sulfur generation and preservation on H_2-annealed TMDs, we also prepared other 2D materials before and after annealing in H_2, *i.e.*, WS_2, H_2-WS_2, $MoSe_2$, and H_2-$MoSe_2$ (See details in Supporting Information), for the *in situ* optical and Raman characterization. We observed similar sulfur growth behaviors as mentioned above for the pristine and H_2-TMDs: only liquid sulfur droplets were generated on the H_2-WS_2 and H_2-$MoSe_2$, whereas the surface of pristine $MoSe_2$ and WS_2 are covered by solid sulfur crystals (Figure 3.5 a, b) eventually. The sulfur phases on the different substrates were confirmed by Raman spectroscopy (Figure 3.5

c). It is noteworthy that solid sulfur is directly growing from the edge and propagating to the basal plane of pristine WS_2, whereas only liquid sulfur droplets can be formed on H_2-WS_2. The different solid sulfur growing behavior on WS_2, $MoSe_2$ and MoS_2 may be attributable to their dissimilar binding energies with sulfur species. For example, WS_2 was calculated to show a stronger affinity to LiPSs than MoS_2 and $MoSe_2$.[17] Together with the intensive electric field at the edge of semi-conductive WS_2, direct solid sulfur formation from the WS_2 edges was observed. All the above evidence demonstrates that liquid sulfur generation in an electrochemical system at room temperature is achievable on H_2-TMD substrates.

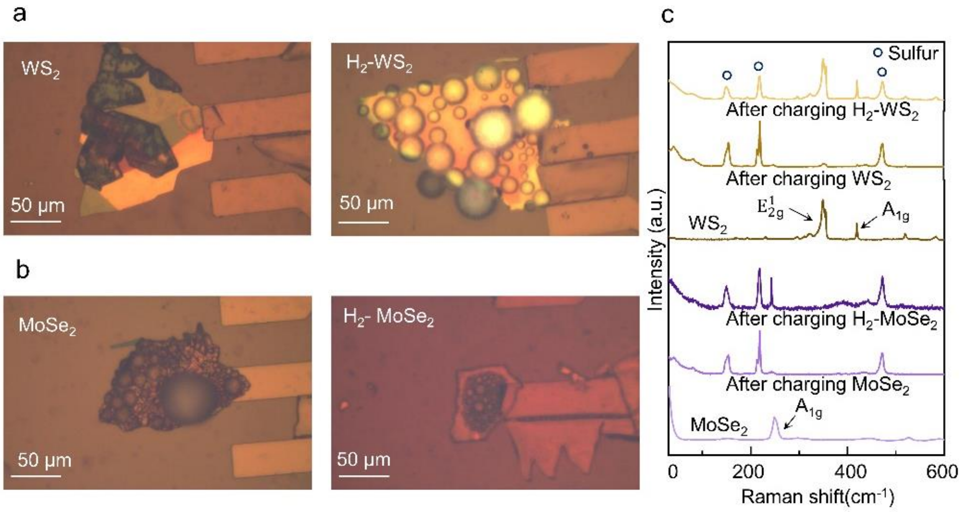

Figure 3.5 a. The optical images of solid sulfur and liquid sulfur formed on the WS_2 and H_2-WS_2 flakes, respectively. b. The optical images of solid sulfur and liquid sulfur formed on $MoSe_2$ and H_2-$MoSe_2$ flakes, respectively. c. The Raman spectra of sulfur generation on $MoSe_2$, H_2-$MoSe_2$, WS_2, H_2-WS_2.

3.2.2 Sulfur growing dynamics on MoS_2 and H_2-MoS_2

Before explaining the distinct sulfur formation behaviors on MoS_2 and H_2-MoS_2, we investigate the liquid sulfur growing dynamics lacking in previous studies. The nucleation and growth kinetics of sulfur droplets are studied by quantitatively analyzing the droplet size and number with charging time, as shown in Figure 3.6. Notably, the growth of the sulfur droplets on the substrate is accomplished by the coalescence of adjacent particles and the isotropic growth of individual particles (Figure 3.7). For the sulfur growing kinetics study, we selected droplets driven by the delithiation of polysulfides without coalescence occurring. Accordingly, we choose three droplets on H_2-MoS_2 (designated as $1^{\#}$, $2^{\#}$ and $3^{\#}$ with dash circles in Figure 3.6e) and another three on the MoS_2 (designated as 1, 2 and 3 with dash circles in Figure 3.6a) as control. It is observed that the sizes of the droplet 1 and 2 on the basal plane of MoS_2 approached 10 µm at approximately 80 seconds (Figure 3.6b), whereas it only needs around 48 seconds for 1# and 3# to reach this size on H_2-MoS_2 (Figure 3.6f). Thus, the average sulfur growing rate on H_2-MoS_2 is more than 1.5 times faster than on MoS_2. The faster-growing kinetics can be attributable to the tailored electrical conductivity or/and binding energy between sulfur species and H_2-MoS_2.[113] In addition, we measured the I-V curves (Figure 3.8a) of pristine MoS_2 and H_2-MoS_2. Their conductivity can be calculated using the formula:

$$\frac{1}{\rho} = \frac{R \times w \times t}{L} \tag{18}$$

The thickness (t), width (w) and length (L) of the MoS_2 flake are 200 nm, 17.5 µm, 12 µm and ρ refer to conductivity. The electrical conductivities of MoS_2 before and after H_2 treatment are determined as 16 S m^{-1} and 213.7 S m^{-1}. H_2 annealing introduced sulfur deficiency on the basal plane, which improved the electrical conductivity of MoS_2.[114,115]

The electrical conductivities of MoS$_2$ (200nm) before and after H$_2$ treatment are determined as 16 S m^{-1} and 213.7 S m^{-1}. A closer examination shows that the change of droplet size becomes slower with time increase, which is consistent with the diffusion-controlled reaction.[116] Further studies are needed to elucidate the origin of the distinct kinetic transition behavior of sulfur growth in a liquid electrochemical system.

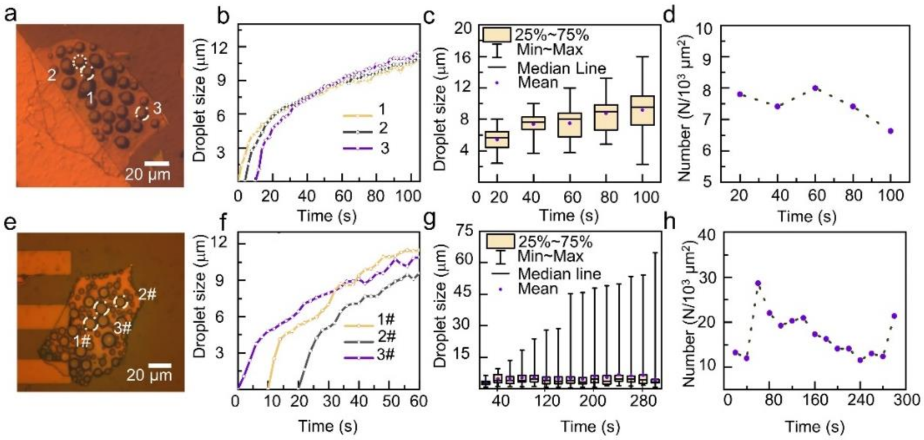

Figure 3.6 a. Optical image of the three chosen droplets marked as 1, 2, 3 on MoS$_2$. b. Growth behavior of the three droplets in a. c. Droplets size distribution during the charging process on MoS$_2$. d. Droplets number per 1000 μm^2 on MoS$_2$. e. Optical image of the three chosen droplets marked as 1$^{\#}$, 2$^{\#}$, 3$^{\#}$ on H$_2$-MoS$_2$. f. Growth behavior of the three droplets in e. g. Droplets size distribution during the charging process on H$_2$-MoS$_2$. h. Droplets number per 1000 μm^2 of H$_2$-MoS$_2$.

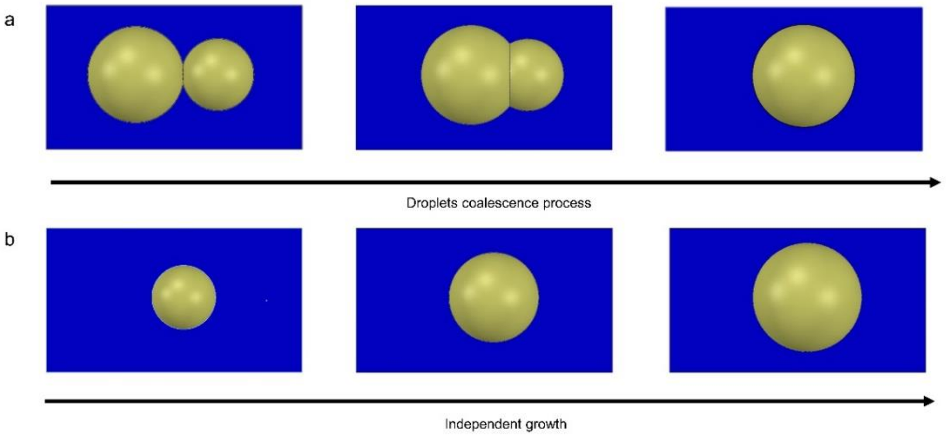

Figure 3.7 a. The process of droplets coalescence. b. The process of droplet-independent growth.

We further examined the overall particle size distribution of the sulfur product as a function of time. The size distributions are plotted as bar graphs with the growth time in Figure 3.6g. At 20 seconds, the average droplet size on H_2-MoS_2 is 2.87 ± 1.25 μm, rendering a standard error of 15.9%. After 100 seconds, the standard deviation increases up to 3.83 μm, also the mean and median difference is 40.4%. The increasing disparity in size distribution with time suggests progressive nucleation of the sulfur droplets, which is described as the continuous formation of small nuclei during other particles growing on the substrate. Similar phenomena are also observed in the overall sulfur droplet size distribution on MoS_2 (Figure 3.6c). Therefore, it is evident that the precipitation of sulfur on MoS_2 substrates follows the progressive nucleation model.[117] Interestingly, the number density of sulfur droplets on H_2-MoS_2 is continuously decreasing from 36.9×10^3 μm^{-2} at 80 seconds to 20.8×10^3 μm^{-2} at 280 seconds (Figure 3.6h). It means there is competition between the nucleation (increase the droplet number) and the coalescence (decrease the droplet number) process. The interfacial tension drives the coalescence of the contacted droplets to reduce the surface energy in the system.[118,119] Apparently, the merging speed surpasses the nucleation speed of sulfur droplets between 80 and 280 seconds, which would free active surfaces on H_2-MoS_2 for excess sulfur deposition, leading to high areal capacities in practical batteries. In contrast, the number density of sulfur particles on MoS_2 exhibits slight fluctuation after the solidification of sulfur droplets (Figure 3.6d), leading to complete coverage of the conductive host by insulating sulfur, rendering relatively low areal capacities (Figure 3.8b). The capacity was calculated based on the following formula:

$$\text{Area capacity} = \int I\,dt/A \tag{19}$$

I is current, t is time and A is area.

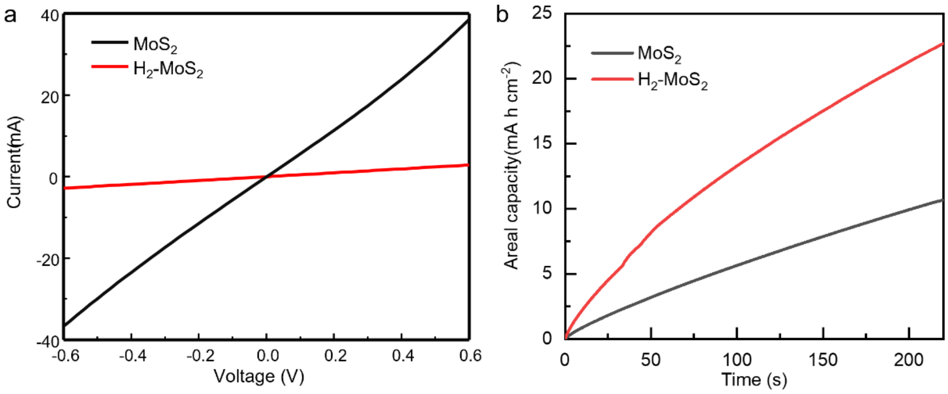

Figure 3.8 a. Current-voltage (I-V) curves of MoS_2 sample and H_2-MoS_2 using two-probe resistance measurement. b. Comparison capacity of MoS_2 and H_2-MoS_2.

In brief, the progressive nucleation and droplet-merging growth models contribute to the aggressive growth of large sulfur droplets for high areal capacity Li-S batteries with H_2-MoS_2.

3.2.3 Mechanisms of entire liquid sulfur generation on H_2-MoS_2

Sulfur display different growth behavior on the MoS_2 and H_2-MoS_2. To better understand the difference between these two kinds of substrate, we performed material characterization of these two substrates, as shown in Figure 3.9.

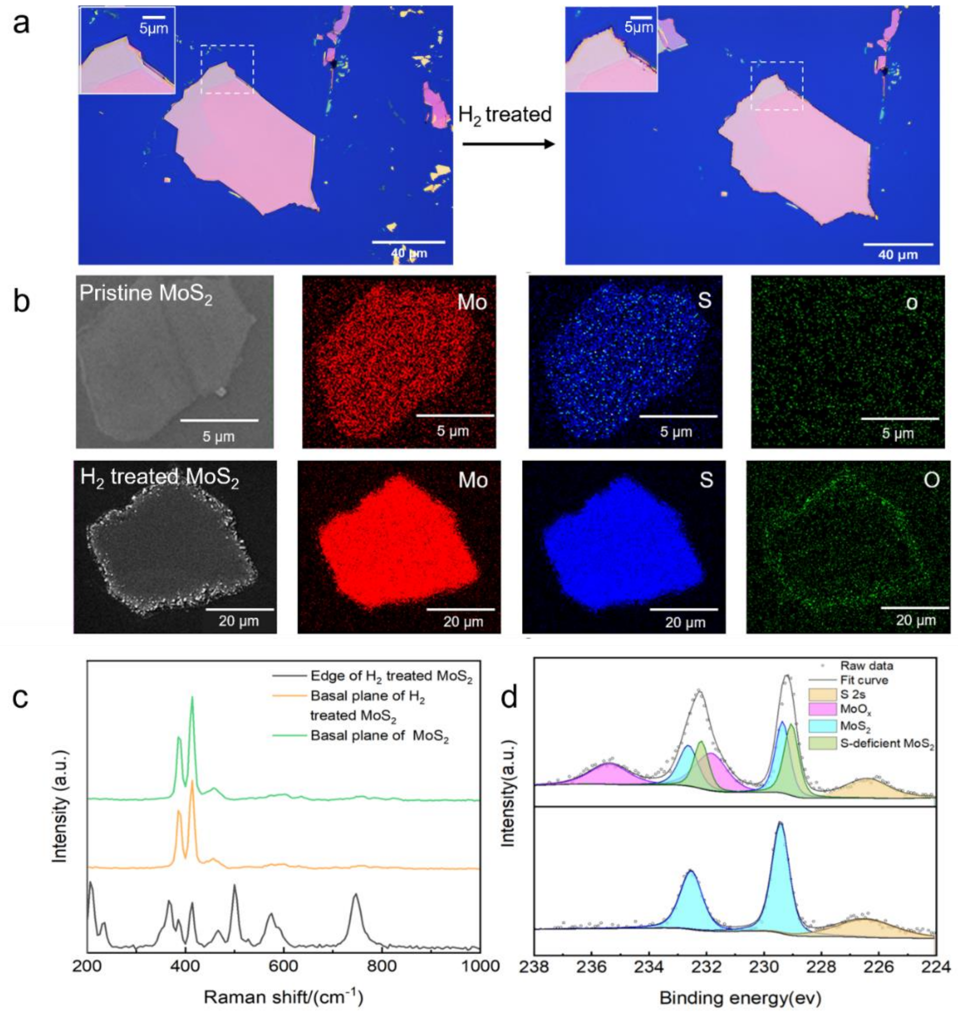

Figure 3.9 a. The optical images of MoS_2 flakes before and after H_2 annealing. b. SEM images of the MoS_2 and H_2-treated MoS_2. c. Mo 3d XPS spectra of the MoS_2 (bottom) and H_2-MoS_2 (top).

Optical microscopy (OM) and scanning electron microscopy (SEM) images reveal no apparent change in the overall morphology of MoS_2 after H_2 annealing treatment, except for some particles formed on the edge area of H_2-MoS_2 (Figures 3.9a, b). Energy-dispersive spectroscopy (EDS) elemental maps indicate these particles as marginal MoO_x compounds. Then, to identify the chemical structures of H_2-MoS_2, we performed Raman, X-ray photoelectron spectroscopy (XPS). XPS spectra show nonnegligible peaks referring to MoO_x.[120] Raman spectra (Figure 3.9 c) on the basal plane and edge area of H_2-MoS_2 are significantly different, with distinct features referring to MoS_2 and MoO_x, respectively.[121] It means the edges of MoS_2 flakes are partially oxidized during the annealing process. The reason for the formation of MoO_x around the edges may be that the edges of MoS_2 are more easily reduced to low oxidation state Mo atoms and then oxidized in the air when the sample is removed from the furnace.[75,122] Another interesting message derived from the Mo 3d XPS spectra of the MoS_2 and H_2-MoS_2 is the appearance of new peaks at 232/229 eV(Figure 3.9c), corresponding to sulfur-vacancy rich H_2-MoS_2.[120,123] High-resolution TEM (HRTEM) images (Figure 3.10) confirmed that the 2H MoS_2 phase was kept intact.

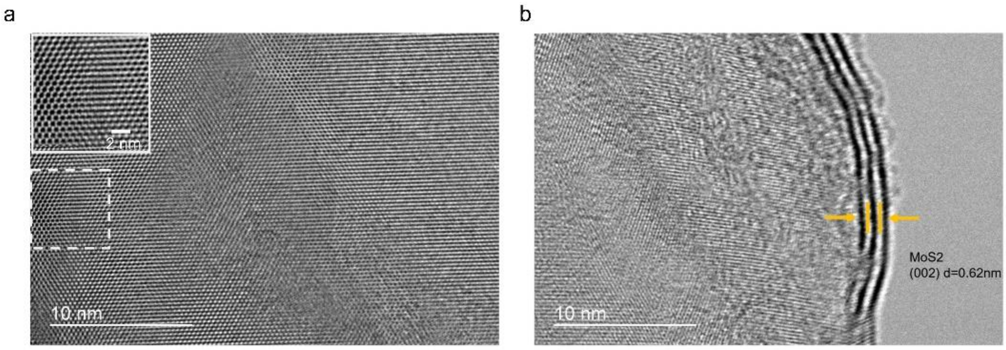

Figure 3.10 HRTEM images of the H_2-MoS_2.

Thus, it is concluded that the H_2 annealing treatment can induce sulfur vacancies on the basal plane and partial oxidation on the edge of MoS_2. The chemical structure of the edge area were measured by SEM and STEM. The EDS mapping of the edge area displayed Mo: S: O atomic ratios of 1: 0.96: 2.23, demonstrating the severe oxidation at the edge area with discrete oxidized particles (Figure 3.11 a, b). A close look at the oxidized particles in STEM illustrates an atomic ratio of approximately 1:1:1 for Mo: S: O (Figure 3.11 d, e), suggesting MoS_2 has been oxidized.

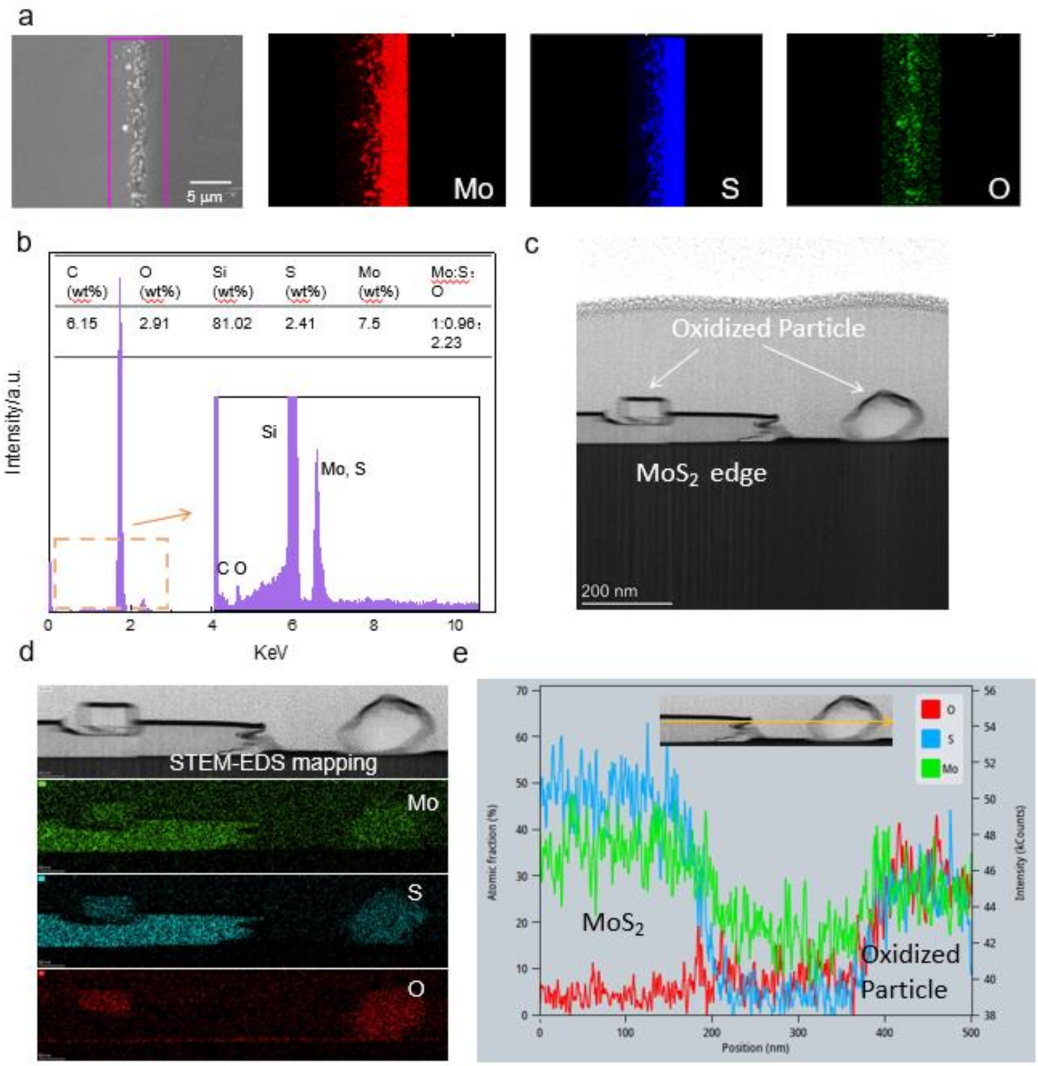

C (wt%)	O (wt%)	Si (wt%)	S (wt%)	Mo (wt%)	Mo:S: O
6.15	2.91	81.02	2.41	7.5	1:0.96: 2.23

Figure 3.11 a. The SEM imaging and EDS-mapping imaging of the edge of H_2-MoS_2. b. The SEM-EDS spectrum of the edge of H_2-MoS_2. c. HAADF-STEM-EDS images of the H_2-MoS_2. d. The STEM EDS-mapping images of the H_2-MoS_2. e. EDS line scanning profiles.

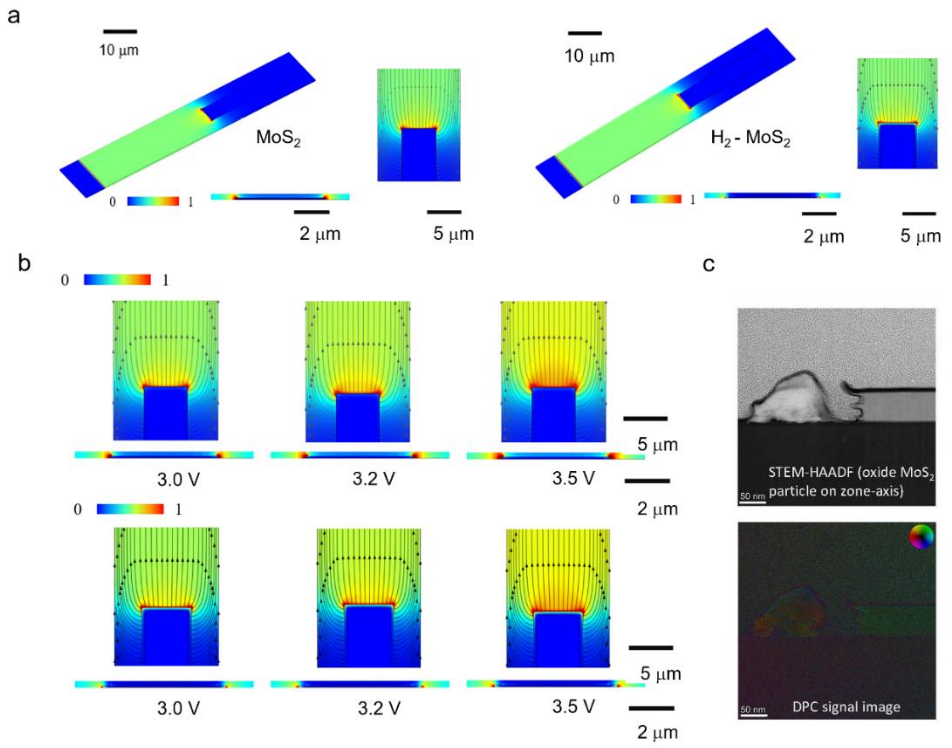

Figure 3.12 Electric field distribution on a. MoS_2 and H_2- MoS_2 at 2.8 V, b. at 3.0 V, 3.2 V and 3.5 V. c. HAADF-STEM-EDS images of the MoS_2 layers and oxidized MoS_2 and their related DPC signal image (the color represents the measured field direction).

Because the non-uniform electric field distribution on the edge was the critical factor contributing to the solid sulfur formation on MoS_2, the electric field distribution on H_2-MoS_2 is of primary interest in understanding the liquid sulfur formation. We simulated the electric field distributions on H_2-MoS_2 and MoS_2 flakes by applying constant voltages of 2.8, 3.0, 3.2, and 3.5 V (Figure 3.12a, b). Compared with the intense polarization at the edges of MoS_2, there is a buffer region to passivate the electric field distribution on the edge for H_2-MoS_2. In addition, the relative permittivity of MoO_2, the main component in MoO_x, is lower than that of MoS_2[124,125] but is closer to that of the electrolyte. Thus, the MoO_x compounds could provide the transition of electric field distribution. The different phase contrast (DPC) image in Figure 3.12c clearly illustrates the various electric fields in the oxidized edge areas and the intact basal plane of H_2-MoS_2, consistent with the simulation results under constant external potentials. Furthermore, the relatively homogeneous electric field at the edge of H_2-MoS_2 can decrease the local sulfur supersaturation and electrowetting effect, thus suppressing the ordering of S_8 molecules into solid crystals on the edges. In contrast, strongly localized partial charges and enhanced electric fields appear at the edge of MoS_2 upon applying constant potentials, consistent with the previous report.[17] The enhanced driving force promoted the droplet wetting on the edge, which lowered the energy barrier from liquid to a solid phase transition, thus facilitating the crystallization of sulfur on the edge. The weakened wettability of liquid sulfur on H_2-MoS_2 edges can be directly evidenced by comparing the contact angles of sulfur droplets on MoS_2 materials. During the charging process, some sulfur droplets grew along the edge of MoS_2 flakes (Figure 3.13a, b), allowing us to measure the contact angles from the top view directly. The contact angle between sulfur droplets and H_2-MoS_2 was around 113°, almost twice the 56° contact angle between a sulfur hemisphere and pristine MoS_2. This result clearly illustrates much stronger wettability between sulfur droplets and MoS_2 than that for H_2-MoS_2. Thus, the poor wettability between H_2-MoS_2 and liquid sulfur, as well as the uniformed electric field distribution, play critical roles in preserving the liquid sulfur on the edge of H_2-MoS_2.

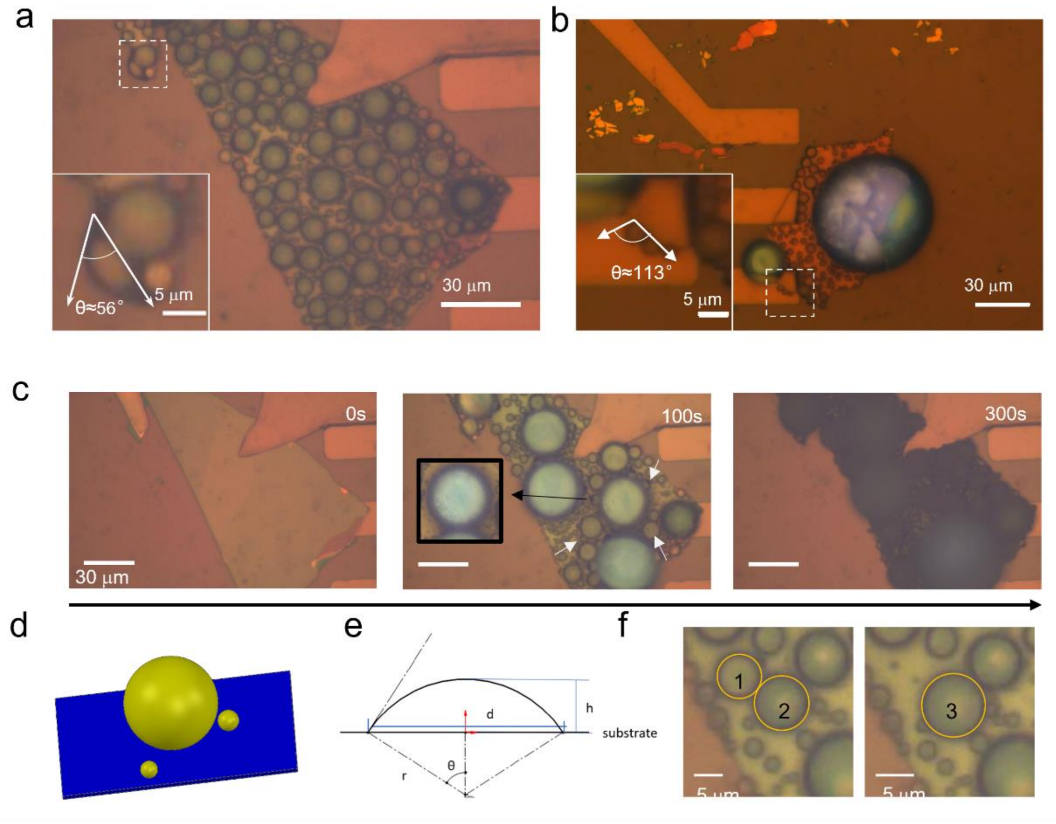

Figure 3.13 Liquid sulfur generation on a. MoS_2 and b. H_2-MoS_2 flakes. Insets are the contact angle between the sulfur droplet and the MoS_2 (or H_2-MoS_2) edge. c. Optical images of liquid sulfur generation on the MoS_2 at 2.8V, as a function of time. d. The model was built based on the contact angle of 180°. e. The schematic of the spherical cap. f. The optical images illustrate the process of droplet 1 coalesced with droplet 2 to form droplet 3.

It is noted that the contact angles between sulfur droplets and MoS_2 measured in this work are different from the hypothesized 180º in the previous work.[17] To demonstrate the soundness of the results in this work, we (i) analyzed the droplet merging behaviors in this work by assuming a 180º contact angle between droplet and MoS_2, and (ii) calculated the volumes of sulfur droplets using the geometric models with measured contact angles in this work. As marked by white arrows in Figure 3.13c, several small droplets (around 5 μm in size) are in physical contact with a large droplet of 31 μm in size on MoS_2 at 100 seconds. They merged later, as shown in the inset of Figure 3.13c. If the contact angle between sulfur droplet and MoS_2 is close to 180°, above adjacent droplets with significantly different sizes will be either disconnected from each other or not displaceable simultaneously (Figure 3.13d), which disagrees with the experimental observation. If the contact angle is less than 90°, such as 56º measured in this work, the equivalent between the experimental result and the model becomes reasonable and plausible. Further, we calculated the volumes of two droplets before and after merging using a spherical cap model with the 56º contact angle (Figure 3.13e). It shows that the volume of the merged droplet is almost equal to the sum of volumes of two-parent droplets Figure 3.13f. We can measure the d1 = 7.78 μm, d2 = 9.46 μm, d3 = 11.13 μm, θ = 56.25° and the volume of droplets are calculated using the following formula:

$$V = d^3 \times \frac{\pi(2+\cos\theta)(1-\cos\theta)^2}{24 sin^3\theta} \tag{20}$$

Furthermore, it is noted that the merging process only takes 0.1 seconds. Thus the growth of the droplets from polysulfide oxidation can be negligible. These results also suggest that the contact angle should not change significantly during coalescence. Based on this finding, we also calculated the total volumes of sulfur droplets on H_2-MoS_2 at different charging times, which display an accordant tendency with the areal capacities (Figure 3.14).

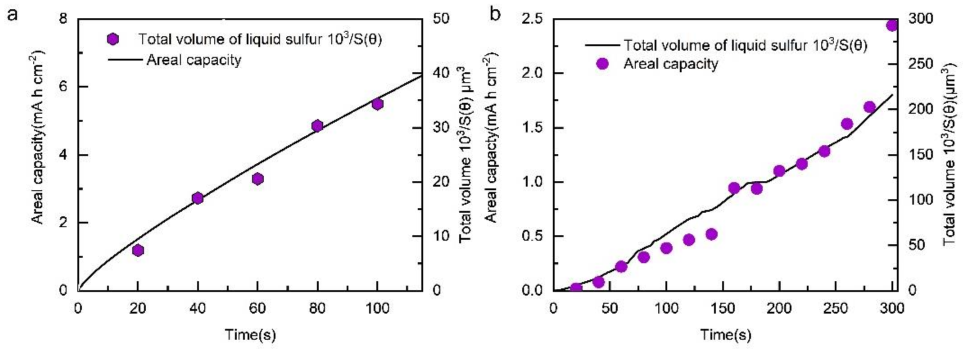

Figure 3.14 a. The correlation of areal capacity and total volume of droplets of MoS$_2$. b. The correlation of areal capacity and the total volume of the droplets of H$_2$-MoS$_2$.

Therefore, the contact angles measured for sulfur droplets and MoS$_2$ materials in this work are plausible and capable of predicting the wettability effect and furthering the solid sulfur growth behaviors.

The sulfur deficiency on the basal plane of H$_2$-MoS$_2$ is verified by the integrated differential phase contrast (iDPC)-STEM image, as shown in Figure 3.15a. To further probe the fundamentals of distinct sulfur growing behaviors on pristine MoS$_2$ and H$_2$-MoS$_2$, we also performed density functional theory (DFT) calculations. We evaluated the binding energy between the S$_8$ molecule and the surface of MoS$_2$ at various sulfur vacancy content. We selected 7 sulfur atoms of the upper layer of MoS$_2$ as being directly under the S$_8$ molecule. For a given number of sulfur vacancies (from 2 to 6), their precise location dramatically affects the binding energy (*e.g.*, 2 vacancies adjacent versus 2 vacancies away from each other). There are C_k^n combinations corresponding to k vacancies (k = 1 to 7) out of n = 7 sites giving a total of 128 structures and binding energies. Therefore, we developed an automatic procedure to compute all the 128 binding energies. It is clearly illustrated in Figure 3.15 b that, on average, the magnitude of the binding energy between S_8 and H_2-MoS_2 decreases when the vacancies number increases. The weaker binding likely leads to the stabilization of liquid sulfur droplets.[17] The binding energies between S_8 and $MoSe_2$ with diselenide deficiency also have a similar change tendency, as shown in Figure 3.15 c, thus explaining the exclusive liquid sulfur formation on H_2-TMDs. Furthermore, we found that the binding energy between the lithium polysulfide Li_2S_8 and the substrate increases with sulfur vacancies (Figure 3.15 d). It suggests that the defective substrate has more absorption efficiency to lithium polysulfide than pristine MoS_2,[108] which is beneficial to polysulfide entrapment on H_2-MoS_2. The efficient absorption of polysulfide could correlate with higher kinetics of the electrocatalytic conversion of polysulfide.[124] The theoretical analysis demonstrates that the H_2-MoS_2 favors both the liquid sulfur preservation and the superior reaction kinetics, in total agreement with the above experimental observations.

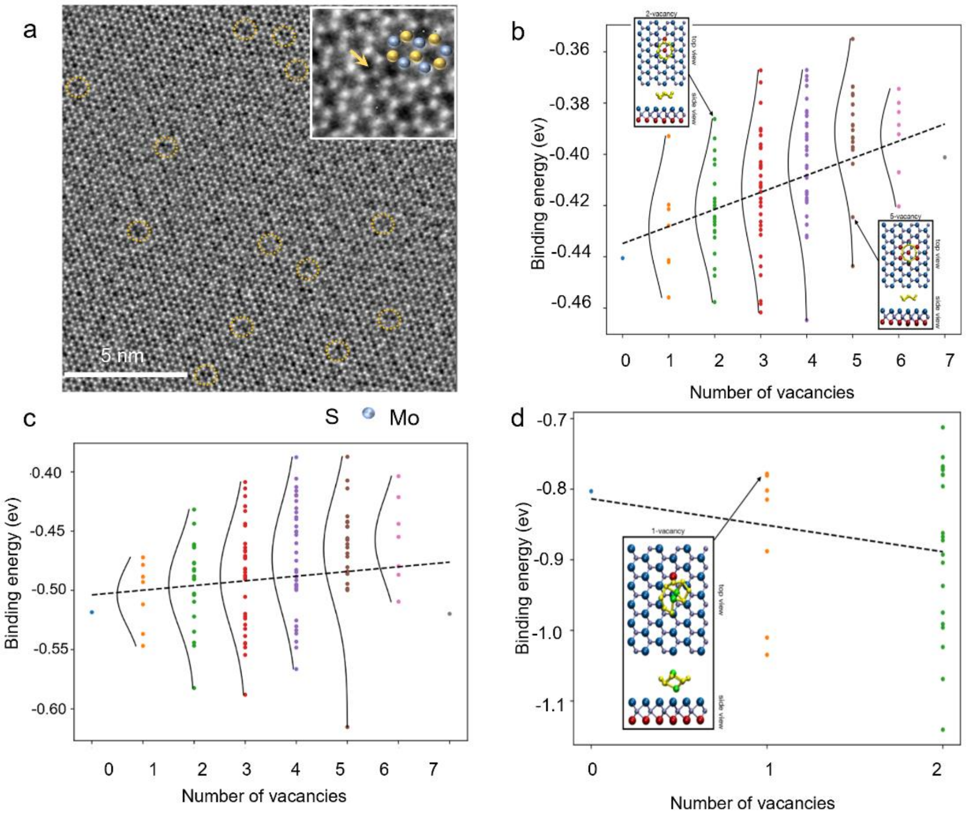

Figure 3.15 a. iDPC-STEM image of H_2-MoS_2. Sulfur vacancies are highlighted by bash circles and an arrow (in the inset). b. The binding energy between the S_8 and MoS_2 as a function of sulfur vacancies. c. The binding energy between the S_8 and $MoSe_2$ as a function of sulfur vacancies. d. The binding energy between the Li_2S_8 and MoS_2 as a function of sulfur vacancies.

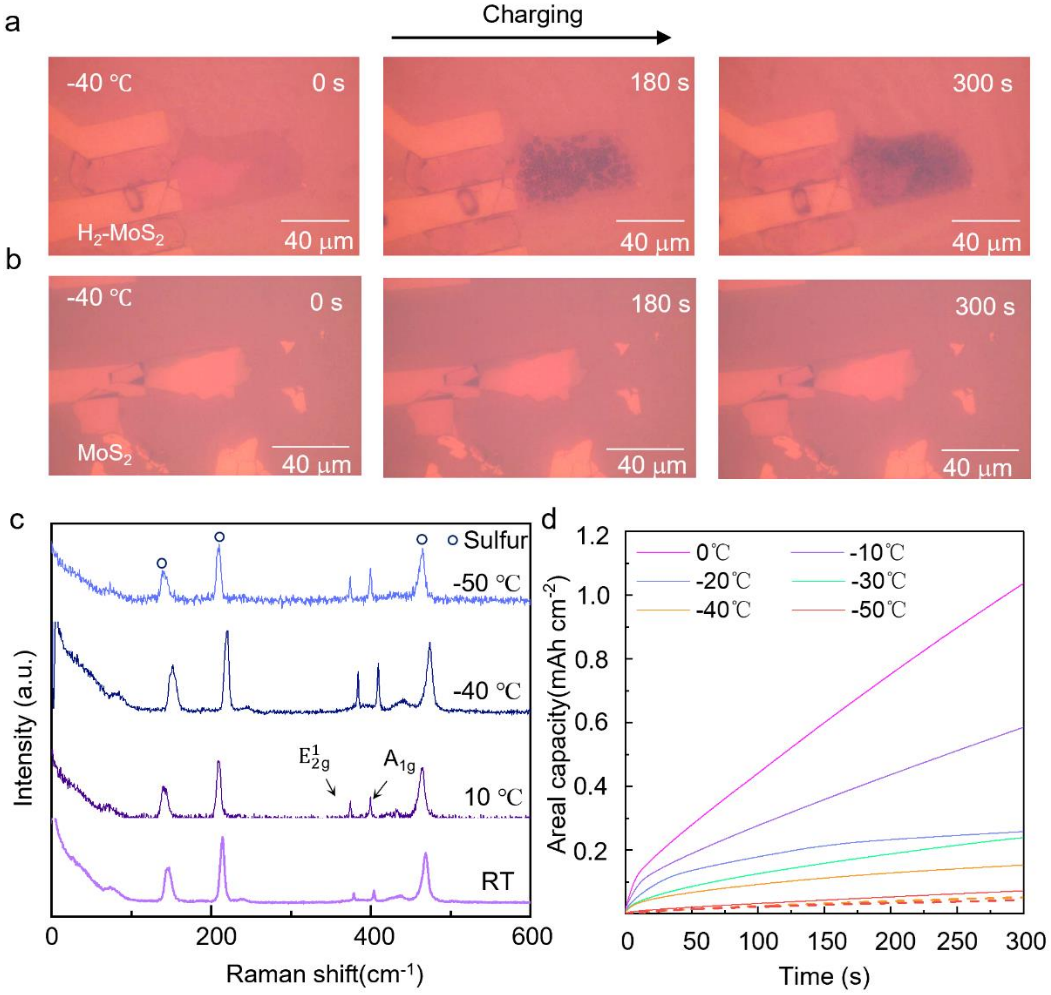

Figure 3.16 a. H_2-MoS_2 and b. MoS_2 at -40 °C. c. Raman spectra of liquid sulfur generation on H_2-MoS_2 at different temperatures. d. The areal capacities when charging the H_2-MoS_2-based optical cells at temperatures ranging from 0 to -50 °C (solid line) and MoS_2-based optical cells at temperatures -40 °C and -50 °C (dash line).

3.2.4 Electrochemical performance of Li-liquid S cells working under low temperatures

Finally, to assess the electrochemical performance of the Li-liquid sulfur system, we tested the micro-Li-S cells with H_2-MoS_2 as working electrodes at decreasing temperatures ranging from room temperature (25 °C) to -50 °C. We chose -50 °C as the lowest testing temperature because the dimethoxyethane solvent in the electrolyte can freeze below -58 °C.[125] Commercial batteries' capacity retention and rate performance deteriorate severely below 0 °C, and they can hardly work at -20 °C.[125,126] Li-S batteries have the potential to be applied to a low-temperature condition not only for their high specific capacity but also for the low freezing point of electrolytes.[125] The micro-Li-S cells were located in a liquid nitrogen-controlled low-temperature device. When we applied an overpotential of 2.8 V to the electrochemical system, only liquid sulfur generation was observed on the H_2-MoS_2 at room temperature, 10 °C, -40 °C, and even -50 °C (Figure 3.16a and 17), which was confirmed by the Raman spectra with only Rayleigh wing features between 10 and 100 cm^{-1} (Figure 3.16c).

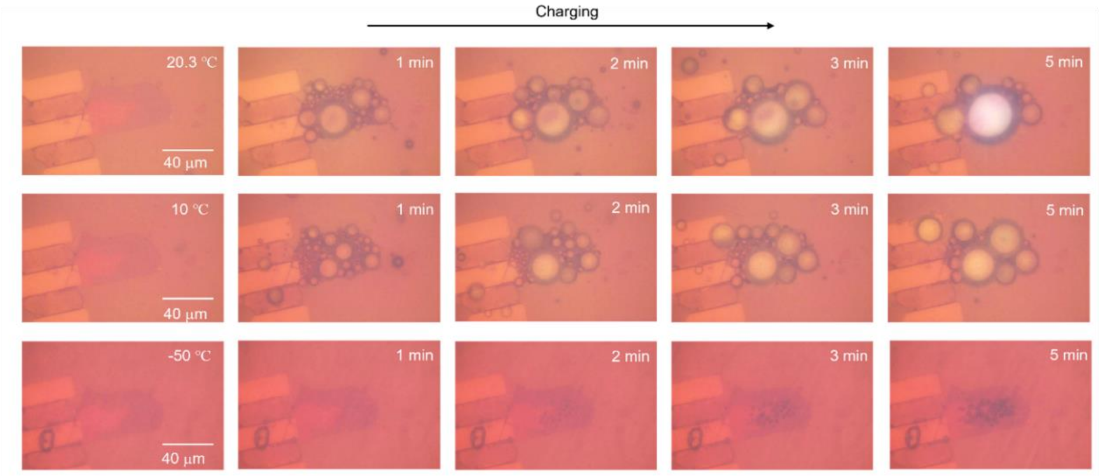

Figure 3.17 Evolution of the optical images at room temperature, 10 °C and -50 °C. Only liquid sulfur is observed when a 2.8 V is applied.

The supercooling sulfur at -50 °C, which is much lower than the melting temperature of 155 °C, warrants further discussion. No solid sulfur formation implies the disordered nature of the sulfur molecular in the long-range, which may be driven by the thermodynamic variations between liquid Li_2S_8 and S_8 under moderate electrochemical potentials. The low temperature (*i.e.*, -50 °C) may induce the glass transition of liquid sulfur, rendering decreased flowability.[14] The correlation among the working temperature, local potential, and the sulfur state requires more investigations in the future. In contrast, no reaction occurred on the basal plane of MoS_2, as shown in Figure 3.16b and Figure 3.18 at -40 °C and -50 °C.

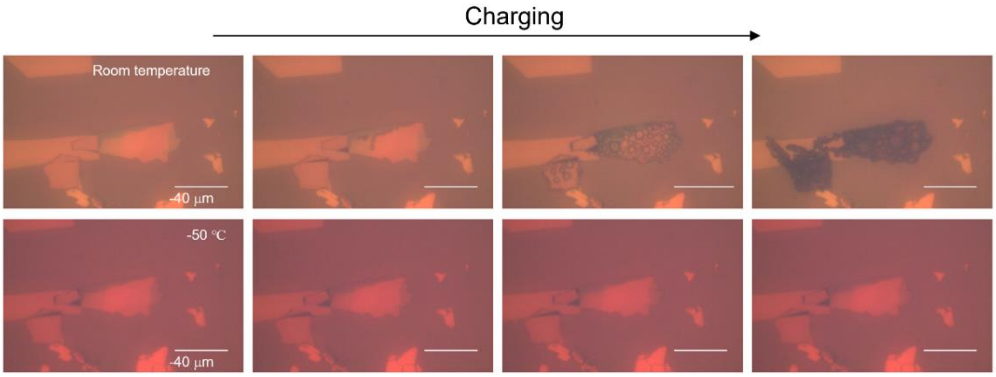

Figure 3.18 Evolution of the optical images at room temperature and -50 °C.

As the working temperature goes below 0 °C, it is notable that the optical observation was blurred by condensed moisture on the glass cover, but the flowable sulfur droplets are still detectable with light contrast color and merging phenomenon. Interestingly, at -40 °C and -50 °C, the size distributions of sulfur droplets formed on H_2-MoS_2 are more uniform than those generated at room temperature (Figure 3.1b). The difference should result from the significantly decreased merging rate (see Figure 3.19, the coalescence of two droplets takes 1 s, which is less than 0.1 s at room temperature) and the growing kinetics of individual droplets at extremely low temperatures.[14] The sluggish kinetics at the low temperature can be amenable by selecting temperature-insensitive ionic liquid electrolytes in future studies.[127]

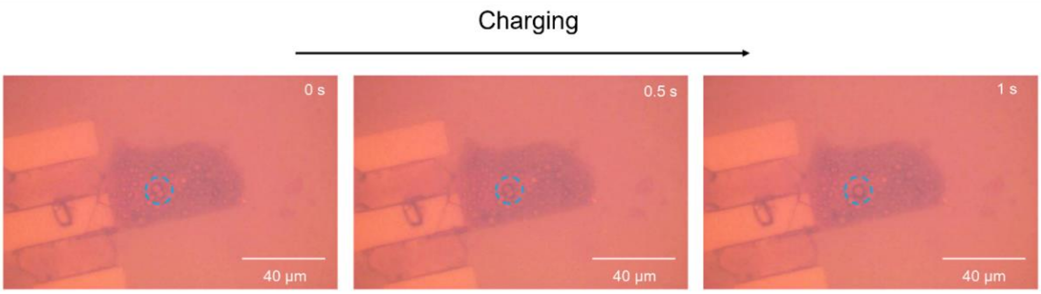

Figure 3.19 The coalescence process of the droplets at -30 °C. The video was recorded in 2 frames/second.

Figure 3.16d presents the areal capacity profiles with charging time at 2.8 V when the working temperature decreases from 0 °C to -50 °C on MoS_2 and H_2-MoS_2 within 5 minutes. It shows the cells can retain liquid sulfur and deliver appreciable areal capacities of 1.04, 0.15, and 0.07 mAh cm^{-2} at 0, -40, and -50 °C on H_2-MoS_2. In contrast, the MoS_2 cell only attributes 0.052 mAh cm^{-2} and 0.043 mAh cm^{-2} at -40, and -50 °C (dash line), which is lower than the H_2-MoS_2 cell. The liquid sulfur sustaining at ultra-low temperature may be attributed to higher reaction kinetics for the Li_2S_8 reduced to liquid sulfur than solid sulfur. However, the coalescence process becomes difficult for the large viscosity of liquid sulfur at low temperatures,[14] and the droplet growth mainly relies on independent growth. The general testing temperature for low-temperature Li-S batteries is -20 °C, regarded as the ‘deadline’ for a battery test.[125,126] To estimate the standing of the electrochemical performance current Li-liquid sulfur system among the reported low-temperature Li-S batteries, we calculated the areal capacity for the whole charging process. It is found that the capacity has the potential to arrive at 1.22 mAh cm^{-2} at -40 °C. The Li-liquid-sulfur system would exclude the need for battery warming in previous LIB systems due to their universal operating capability at ultra-low temperatures.[126]

3.3 Conclusion

In summary, we have demonstrated stable liquid-sulfur generation on H_2-annealed MoS_2 substrates during the delithiation of polysulfides. The liquid-sulfur formation is progressive, rapidly merging and growing, leading to exceptionally large sulfur droplets and high areal capacities. The phenomenon has never been observed in conventional Li-solid-sulfur electrochemical systems. The intriguing liquid sulfur chemistry originates from the partially oxidized layer around the edge of MoS_2 and sulfur vacancies on the basal plane of MoS_2, which effectively tune the electric field distribution and the binding energies to sulfur molecules with H_2-MoS_2 substrates. We have also demonstrated competitive areal capacities and ultra-stable liquid sulfur phases in the H_2-MoS_2-based electrochemical system, decreasing the operating temperature to -50 °C, which has been very difficult for commercial Li-ion batteries and Li-solid sulfur batteries to survive. We believe stable liquid sulfur formation on hydrogen-treated TMDs will spur extensive research interest in liquid sulfur-based flow batteries, fast-charging batteries, and low-temperature energy storage technologies.

Chapter 4 Unlocking liquid sulfur chemistry for fast charging lithium-sulfur batteries

4.1 Introduction

To unveil the Li-S redox reaction mechanisms, rigorous *in situ*/*operando* characterizations have been proposed to monitor the cycling processes in working Li-S cells.[15,88,110,128] *In situ* X-ray diffraction (XRD) revealed the formation of amorphous or crystalline β-S_8 at the end of charging,[15,88] which differs from the α-S_8 starting material. *Operando* X-ray microscopy and tomography illustrated the critical role of current density and temperature in determining the size of the resulting sulfur clusters in cycling Li-S pouch cells.[128,129] The X-ray absorption spectroscopy (XAS) study suggested the redissolution of formed S_8 into the electrolyte to facilitate Li_2S redox throughout the charging process.[110] Quite recently, an *operando* light microscopy captured the generation of supercooled liquid sulfur droplets in an electrochemical cell at room temperature, which is much lower than the melting temperature of sulfur (115 °C).[14,102] This finding signifies the possibility of manipulating the polysulfide redox processes, which entails a fast-kinetic liquid-liquid conversion pathway to replace the sluggish liquid-solid ones in conventional LSBs. The mobility and highly dynamic nature of liquid sulfur also promise to design fast-charging Li-S chemistry or/and regulate sulfur utilization for high capacities.[17] On two-dimensional (2D) layered materials (e.g., MoS_2), the liquid sulfur accumulated on the basal plane is ready to be crystallized once touching the solid sulfur grown from the edge areas.

We found that liquid sulfur can be entirely preserved in the charging process by creating sulfur deficiencies on the 2D surface (*i.e.*, MoS_{2-x}).[17,130] The substrate-dependent liquid sulfur generation was also observed on Al, C, and Ni current collectors, among which the Ni metal demonstrated preservation of liquid sulfur in working LSBs.[18] To date, the research on liquid sulfur chemistry is in its infancy. Many critical questions remain open. For example, what is the role of liquid sulfur in the charging process? Is the liquid sulfur generation a ubiquitous process in LSB or only occurring on specific substrates? How to effectively utilize the *in situ* generated liquid sulfur for high-performance Li-S cells?

Herein, we develop an *operando* electrochemical cell to systematically investigate the sulfur growing mechanisms on a graphene-based substrate. Graphene is the simplest but perfect carbon material without atomic defects and functional groups, thus excluding the unpredictable impacts from substrate chemistry on polysulfide oxidation. In addition, the centimeter-scale graphene sheets provide a large enough platform for the visualization and quantification of sulfur products. We find a general liquid-to-solid sulfur phase transition on graphene sheets (Figure 4.1a). *In situ* Raman spectroscopy, cryogenic transmission electron microscopy (cryo-TEM), and density functional theory (DFT) calculations reveal anisotropic growing dynamics for the solid sulfur towards the (224) crystallographic orientation or the liquid sulfur-rich region. The constrained in-solution growth of solid sulfur emphasizes the importance of preserving liquid sulfur in facilitating sulfur utilizations. By measuring the droplet number, size distribution, and areal capacities, we demonstrate that the former two parameters are more sensitive to the applied current densities than areal capacities. The rationalized guideline suggests designing a lightweight, interconnected, and freestanding carbon nanofiber framework for sulfur cathodes, which enables pronounced amounts of liquid sulfur before becoming solid. The liquid sulfur-associated Li-S cells indicate an impressive electrochemical performance with almost 100% capacity retention, increasing the charging rate by 30-folds at high sulfur loadings, rivaling state-of-the-art power capabilities. This work is believed to provide new insights into liquid sulfur chemistry and feasible schemes to tackle the fundamental challenges facing fast-charging Li-S batteries.

4.1.1 Results and discussion

Optical microscopy equipped with an *in situ* Raman spectroscopy provides an effective platform for monitoring an electrochemical cell's sulfur morphology and phases. The Li-S cell consists of a monolayer graphene film (0.5 cm × 0.5 cm) as the sulfur-growing substrate, 0.25 M Li_2S_8, and LiTFSI in 1,3-dioxolane/1,2-dimethoxyethane (DOL/DME) as the catholyte, and Li metal pressed on the copper foil as the anode, which is sealed between the Si/SiO_2 wafer and a transparent glass cover. Optical and Raman characterization demonstrate the high-quality graphene in Figure 4.2. The graphene substrate is connected to an external circuit by titanium (Ti) microrods, which can block sulfur formation even at a high overpotential of 4.5 V *vs*. Li/Li^+.[102] The micro-cell displayed a stable open-circuit voltage of 2.38 V *vs*. Li/Li^+, consistent with the real Li-S batteries.

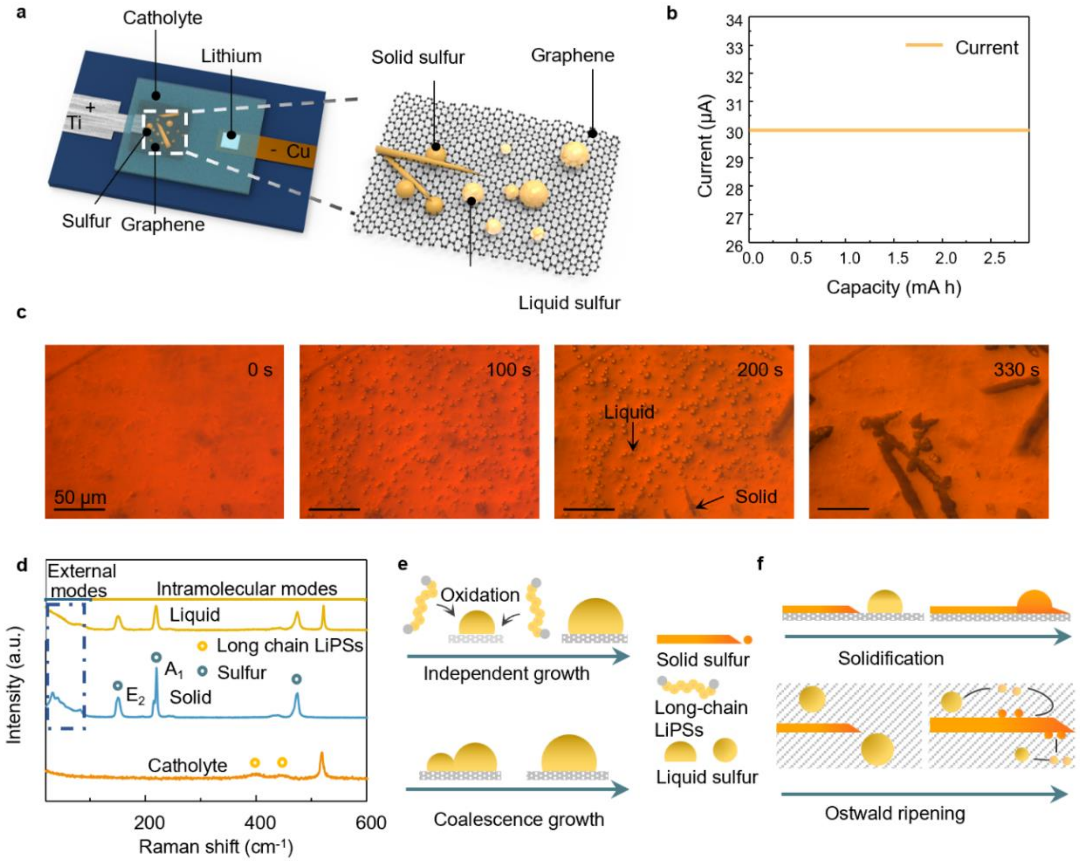

Figure 4.1 a. The schematic of the *in situ* optical cells and sulfur generation on graphene. b. Sulfur generation at a constant current. c. Captured time-sequential optical microscopy images of sulfur generation on graphene. d. The Raman spectra of long chain polysulfides (LiPSs), liquid sulfur, and solid sulfur. The schematics of the e. liquid sulfur and f. solid sulfur growing mechanisms.

A constant current of 30 μA was applied to initiate the $Li_2S_8 - 2e^- - 2Li^+ \rightarrow S_8$ reaction (Figure 4.1b). The electrochemical formation of sulfur is shown in Figure 4.1c. Before applying the external current, the catholyte presents a deep-orange color corresponding to the long-chain polysulfides (Li_2S_8, Figure 4.1c). After charging for a while, a large number of fine nuclei are observed, which grow into discernible droplets with an average size of 3.7 µm at 100 s. Further proceeding the reaction, a needle-shaped solid sulfur appeared at 200 s, when the droplets reached 5.1 µm. Then, solid sulfur growth becomes dominant with the consumption of sulfur droplets.

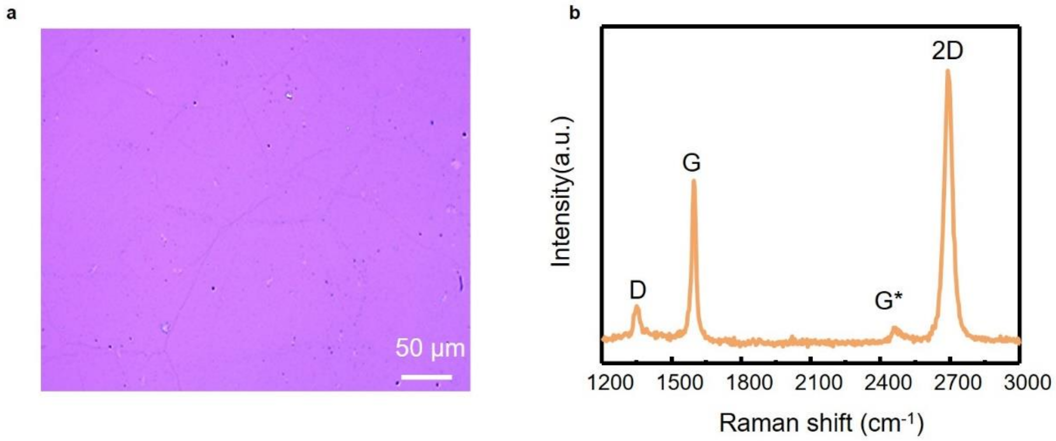

Figure 4.2 a. Optical image of the monolayer graphene on 300 nm SiO_2/Si wafer and b. the corresponding Raman spectrum.

In order to study the phase transition of sulfur species during charging, *in situ* Raman characterization of the electrochemical cell was performed (Figure 4.3). The Raman spectra exhibit peaks at around 400/448 cm^{-1} and 520 cm^{-1}, corresponding to the long-chain polysulfides and Si substrate, respectively.[131] The solid and liquid sulfur phases can be distinguished from the external vibration range (10 - 100 cm^{-1}). The liquid sulfur presents a fingerprint Rayleigh wing in the external vibration due to their long-range disordered structure (Figure 4.1d), whereas the solid sulfur shows broad peaks at 33, 42, and 82 cm^{-1} referring to the β-S_8 crystal.[112] In addition, we can also discern the liquid phase from the solid phase by deconvoluting the intramolecular peaks in the range of 190 - 220 cm^{-1} and 420 - 460 cm^{-1} (Figure 4.4). The doublet peaks at 440/432 cm^{-1} and 218/214 cm^{-1} arise from the crystal-field effects of β-sulfur, whereas the liquid sulfur displays a single peak in these regions.[132,133] The peak at around 462 cm^{-1} indicates long polymeric diradical S_μ chains in liquid sulfur, while the peak at 467 cm^{-1} refers to S-S stretching vibrations in solid sulfur (Figure 4.4b).[112]

Accordingly, we can demonstrate the liquid-to-solid sulfur phase transition in a Raman contour map (Figure 4.3b), where the Raman modes for liquid sulfur gradually disappear along with the increasing peak intensities referring to β-S_8 crystals. By the end of charging, the modes for solid sulfur intensified significantly because of the augmented crystallinity.

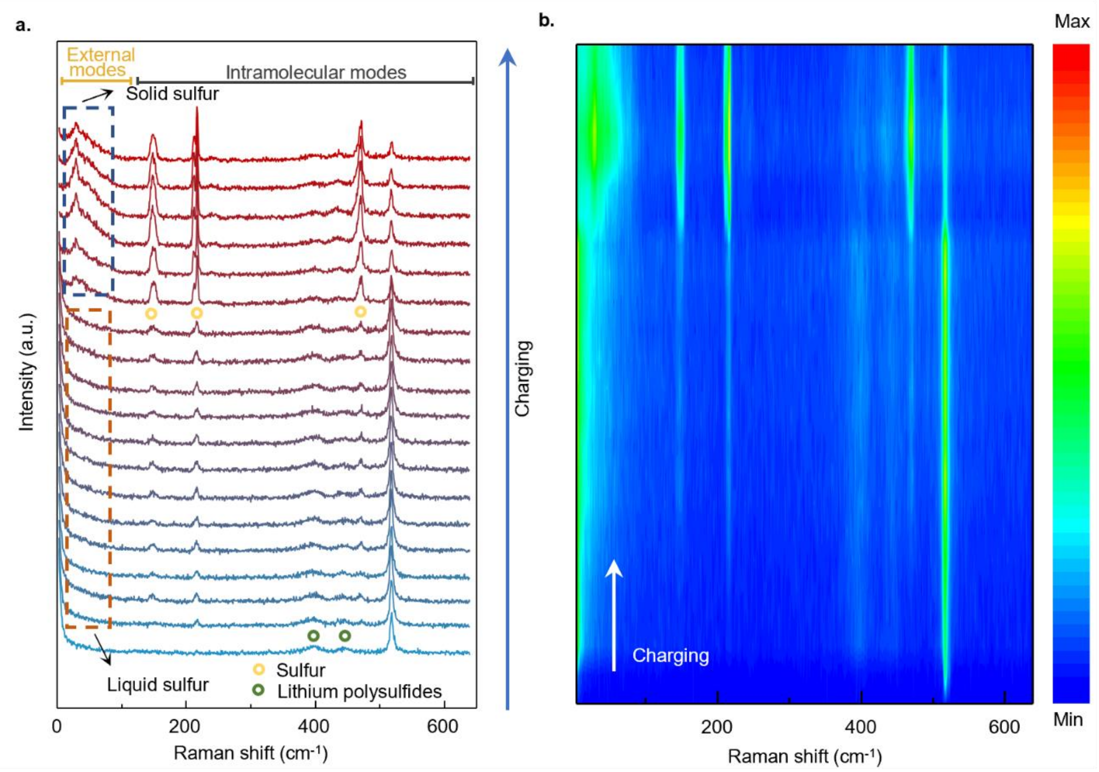

Figure 4.3 a. *In situ* Raman spectra of the phase transition process of sulfur and b. the corresponding contour pattern.

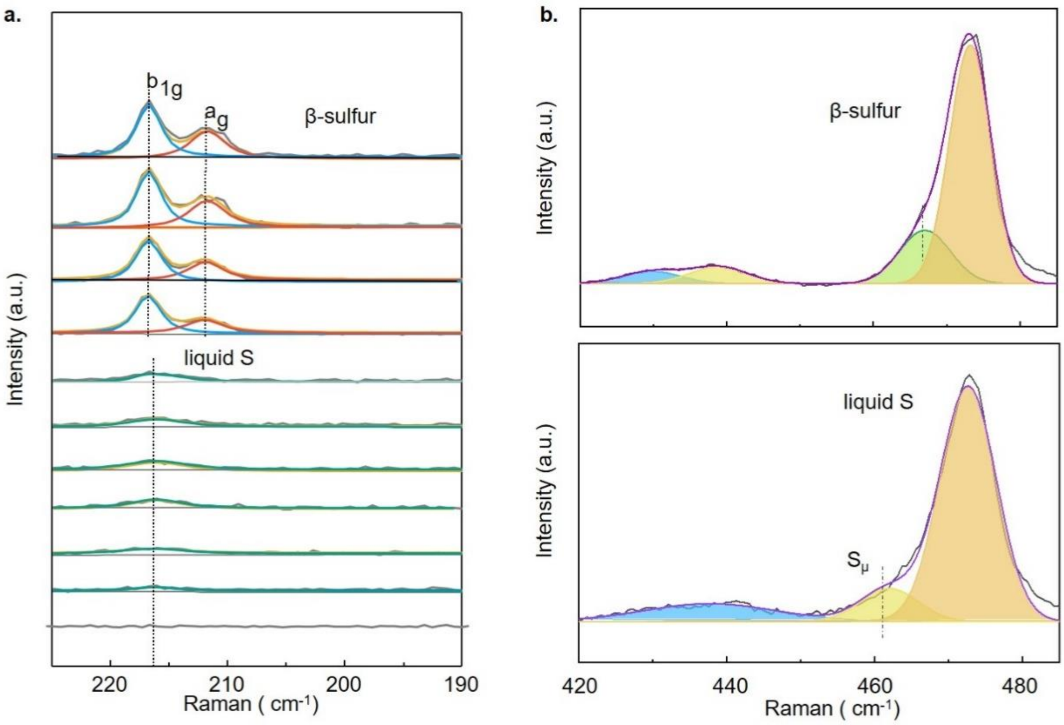

Figure 4.4 a. The *in situ* Raman spectra of the phase transition process of sulfur in the range of 190 cm^{-1} - 220 cm^{-1} and b. the difference of the liquid sulfur and β-sulfur in the range of 420 cm^{-1} - 460 cm^{-1}.

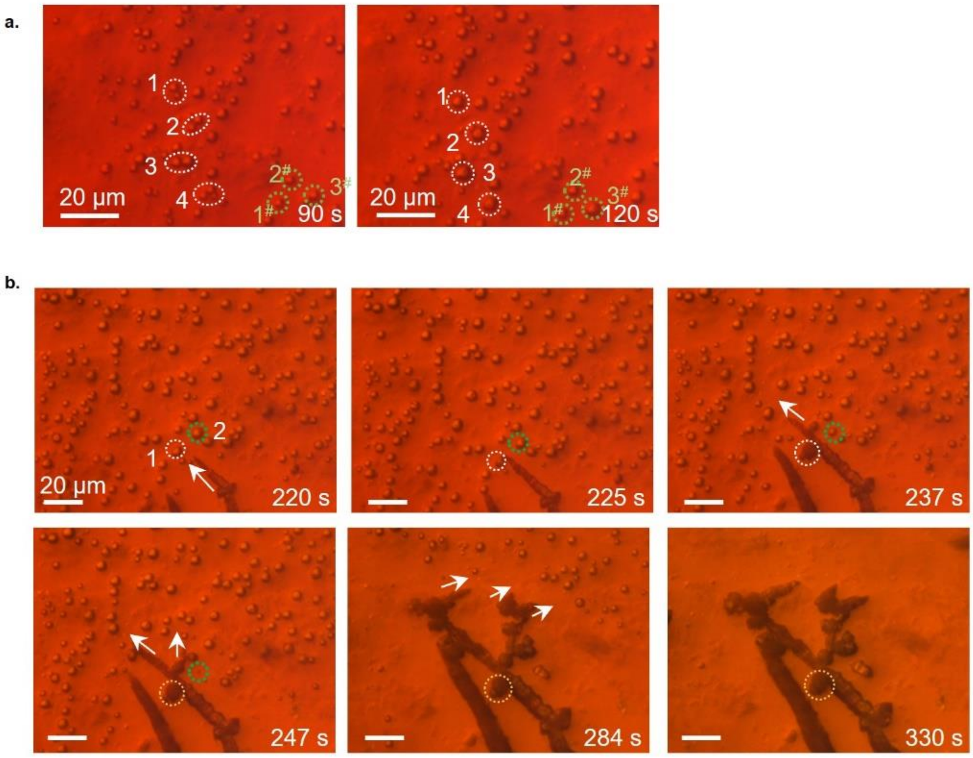

Figure 4.5 a. The optical images of the liquid sulfur growth process. b. The optical images of the solid sulfur growth process.

After demonstrating the formation of liquid and solid sulfur phases, we further analyzed the sulfur species growth dynamics (Figure 4.5). The growth of liquid sulfur may follow two modes - independent and coalescence. The sulfur droplets marked as $1^{\#}$, $2^{\#}$, $3^{\#}$ in Figure 4.5a present independent growth relying on the oxidation of Li_2S_8. The droplets marked as 1, 2, 3, 4 display the liquid sulfur merging process. Two growth mechanisms are summarized as shown in Figure 4.1e. The solid sulfur initially nucleates on the graphene substrate away from the liquid droplets, possibly due to the impurity-induced heterogeneous nucleation. Upon constitution of the charging process, the solid sulfur grows anisotropically into a needle-like shape. According to the images of the solid sulfur growth process, droplet 1 became solid when it was touched by solid sulfur. Droplet 2 gradually disappeared and may redeposition on the solid sulfur because of the Ostwald ripening（Figure 4.5b）. The solid sulfur growth behavior is presented in Figure 4.5b.

Meanwhile, the droplets adjacent to the sulfur crystals will stop growing and dissolve gradually through an Ostwald ripening reaction to deposit on the solid sulfur. Therefore, the solid sulfur undergoes surface deposition and solution-mediated growth pathways, allowing large insulating sulfur particles to form without contacting conductive substrates (Figure 4.5b). Solid sulfur grows anisotropically toward a specific crystallographic orientation or/and the liquid sulfur-rich region, manifesting the importance of liquid sulfur for the charging performance in Li-S batteries.

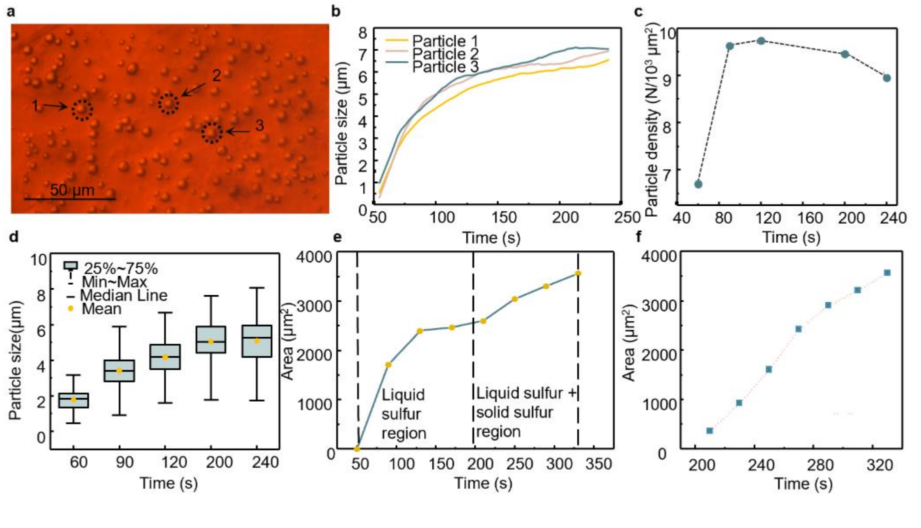

Figure 4.6 a. Optical image of the three chosen droplets marked 1, 2, and 3 on graphene. b. Droplet size distribution changes on graphene during the charging process. c. Particle density on graphene (1000 μm^3). d. Time-sequential droplet size change of particles 1, 2, 3 in a. e. Plot the sulfur area changes with time. f. Plot the solid sulfur area changes with time.

4.1.2 The dynamic transition of liquid and solid sulfur on graphene

Quantifying the growing dynamics of liquid and solid sulfur formed on graphene is essential to unveil the charging kinetics in real Li-S batteries. Only liquid sulfur was generated for the first stage (0-200 s). Hence, we first analyzed the liquid sulfur growing process in a selected area with dimensions of 175 μm ×100 μm (Figure 4.6a). We counted particle sizes in this region and found that the average size of particles reached ~5.02 μm, barely changing after 200 seconds (Figure 4.6b). Furthermore, the standard deviation to the mean droplet size is 0.53 μm at 60 s and increased by over 2-folds to 1.23 μm at 240 s. That means the nucleation follows a progressive mechanism corresponding to the continuous formation of nuclei during the entire charging process. In addition to the independent droplet growth, the coalescence of adjacent droplets to lower the surface energies also occurs, leading to the decreased droplet number, as shown in Figure 4.6c. Droplet merging can release the conductive graphene surfaces for new oxidation reactions (Figure 4.7a). The individual growth of three representative droplets (Figure 4.6a) in this area is plotted as a function of charging time (Figure 4.6d). According to Fick's second law, the sulfur droplets follow diffusion-limited kinetics. As a result, the sizes of sulfur droplets are stabilized at around 6.5 μm, as shown in Figure 4.6d.

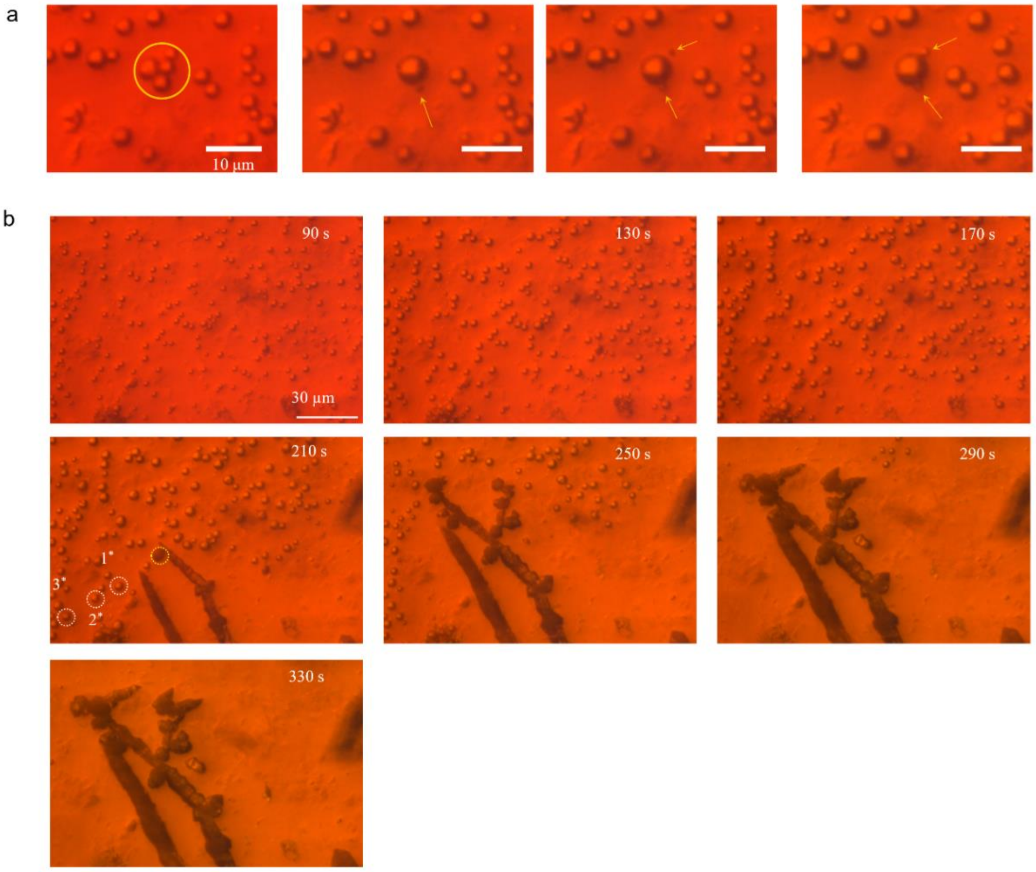

Figure 4.7 a. The photos of new droplets formation on the released conductive surface. b. The selected area is to analyze the relationship between solid sulfur and liquid sulfur

in Figure 4.6e.

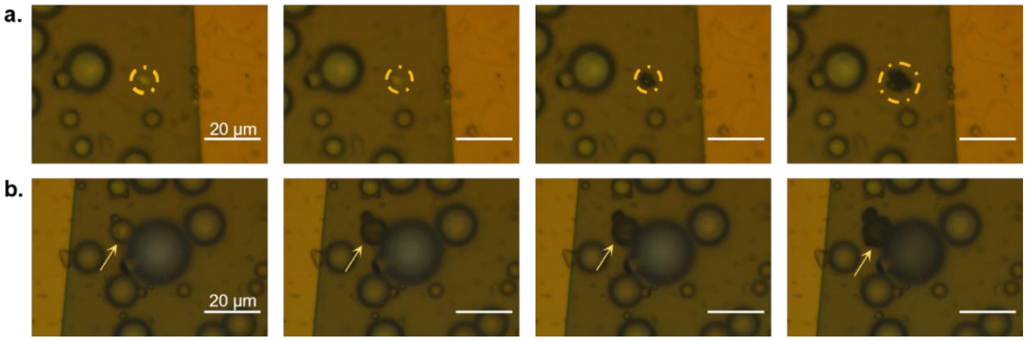

Figure 4.8 a. Solid sulfur formation directly on graphene. b. Solid sulfur conversion from liquid sulfur.

For the second stage, solid sulfur appears and governs the sulfur growing dynamics from 210 s onward, as shown in Figure 4.6e and Figure 4.7b. The increase of liquid sulfur area becomes very slow after 130 s, which is consistent with the change of individual particle size. The emergence of solid sulfur brings about a rapid increase in the oxidation product area. Solid sulfur growth is based on the oxidation of Li_2S_8 and the redeposition of liquid sulfur. The accumulated surface area of solid sulfur is plotted with time in Figure 4.5f. The growth rate refers to the surface area slope over time. It slows down after 290 s when the liquid sulfur is exhausted. Figure 4.5e, f claims that liquid sulfur contributes to the rapid growth of solid sulfur.

In an effort to understand the origins of the resulting liquid and solid sulfur transition behavior, we performed a classic thermodynamic estimation of S_8 droplets or crystals. According to the nucleation theory, the Gibbs energy change ($\Delta G_{nucleation}$) can be described as [134,135]

$$\Delta G_{nucleation} = -\frac{4}{3}\pi r^3 \Delta G_v + 4\pi r^2 \gamma \tag{21}$$

$$\Delta G_v = \Delta H_v \frac{T_m\text{-}T}{T_m} \tag{22}$$

were ΔG_v, γ, r, T_m, T, ΔH_v represents the free energy change from Li_2S_8 to S_8 per volume, the surface energy of the sulfur/electrolyte interface, the nuclei radius, the equilibrium crystallization temperature, the supercooled temperature, and the volumetric fusion enthalpy, respectively.[136] Eqs (15) and (16) reveal that the supercooled state (T_m - T > 0) favors the driving force ($\Delta G_v < 0$) for nucleation. However, the large surface energy of the liquid sulfur (γ>0) on graphene counteracts this trend even in a supercooled environment (*i.e.*, $\Delta G_{nucleation} > 0$). For the formation of solid sulfur, the energy fluctuation or decreased γ for sulfur formed on impurities can provide the force to overcome the energy barrier to assist the stable growth of the embryonic crystal ($d\Delta G_{nucleation}/dr=0$). Therefore, In the micro-cell device, both direct solid sulfur formation and liquid-solid phase transition happen on the graphene (Figure 4.8), suggesting the thermodynamic favorability of the solid phase at room temperature. In real Li-S batteries, the complex electrochemical, chemical, and electrical environment would indicate liquid phase is vulnerable. Therefore, liquid sulfur is believed to be crystalized finally, in agreement with our experimental result.

4.1.3 Formation of solid sulfur on graphene

Before disclosing the liquid sulfur growing dynamics, looking into the final solid sulfur formed on the graphene sheet is necessary. Due to the low vapor pressure of sulfur, it is infeasible to detect sulfur in the conventional transmission electron microscope (TEM), where the electron gun would heat and sublimate sulfur in a high vacuum environment. In this work, we employed a cryogenic-TEM to relieve the vulnerable sulfur particles.[137,138] In order to visualize the native sulfur crystals generated electrochemically, we designed an *ex-situ* cryogenic-TEM experiment by transferring monolayer graphene on a holey TEM grid (G@TEM) which was assembled in the micro-cell for sulfur growing. Figure 4.9a verified the successful formation of liquid and solid sulfur products on the G@TEM. Therefore, we can utilize the solid sulfur generated in G@TEM as an equivalent sample in Li-S cells (Figure 4.9b, c).

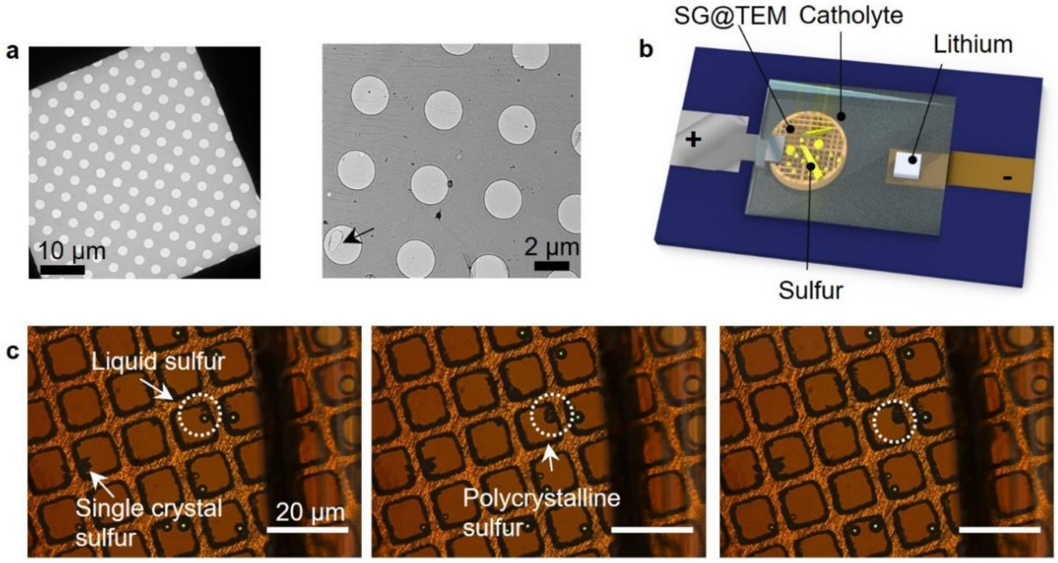

Figure 4.9 a. TEM images of the graphene. The arrow points to the region with and without graphene. b. The schematic of the optical cell to prepare the TEM sample. c. The optical images of solid sulfur and liquid sulfur formation on the G@TEM.

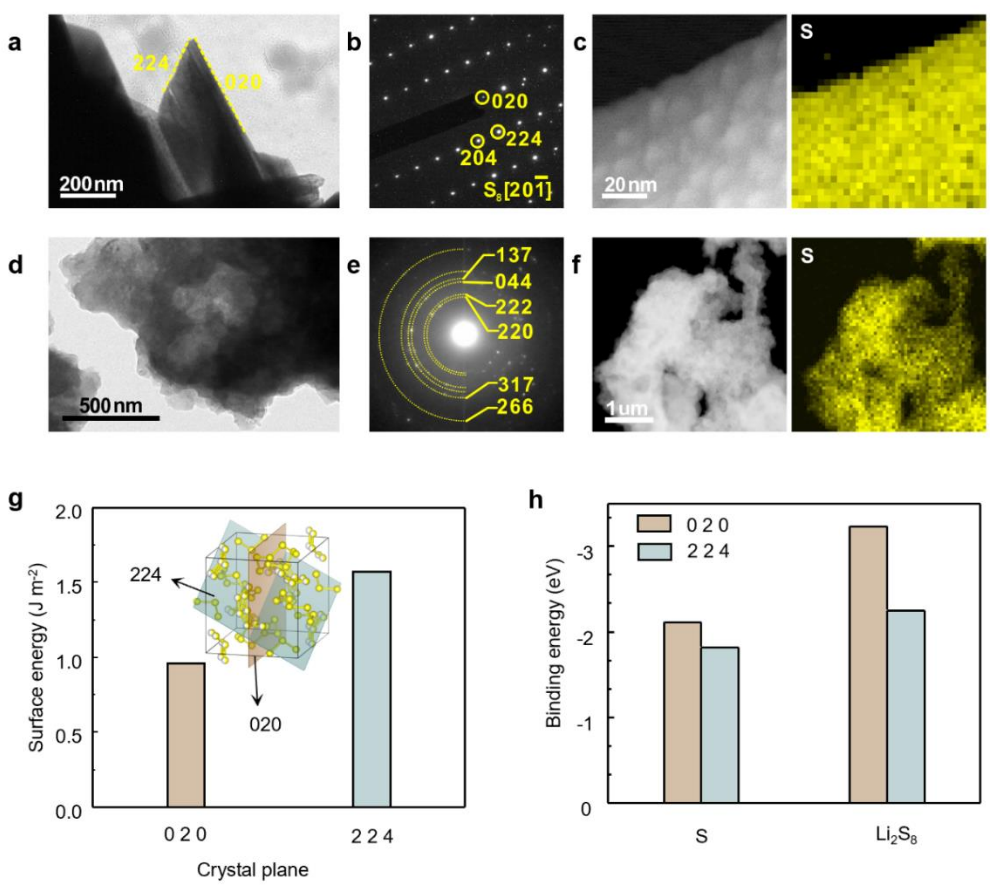

Figure 4.10 a. Cryo-TEM image of needle-like solid sulfur and b. corresponding SAED pattern. c. EDS-mapping of needle-like solid sulfur. d. Cryo-TEM image of solidification sulfur and e. corresponding SAED pattern. f. EDS-mapping of solidification sulfur. g. The surface energy of *β*-sulfur (020) and (224) planes. h. The binding energy of the (020) and (224) of *β*-sulfur to S_8 and Li_2S_8.

Figures 4.10a and d show the TEM images of a needle-shaped crystal and particle-like sulfur, respectively. Energy dispersive spectrometry (EDS) mappings verified the sulfur elements in both structures Figures 4.10c and f. The electron diffraction patterns in Figure 4.10b clearly show the single crystalline nature of the needle-shaped sulfur with indicative spots referring to (020), (224), and (204) planes of *β*-S_8 (PDF No. 01-071-0137). In addition, the needle-shaped sulfur displayed a selective growth orientation towards the surface termination (002). In contrast, the sulfur particle formed from liquid sulfur droplets displayed polycrystalline diffraction rings (Figure 4.10e), which is also evidenced by the Raman spectra (Figure 4.11). The single- and polycrystalline structures of solid sulfur agree with the isotropic and anisotropic growing dynamics as highlighted in Figure 4.5. Density functional theory (DFT) calculations were further conducted to explain the anisotropic sulfur growing along (002) direction. Figure 4.10g shows that the surface energy of 1.57 J m^{-2} for (224) plane is much higher than the 0.96 J m^{-2} for the (020) plane. It was reported that material growing prefers to retain the stable surface.[139] Therefore, sulfur crystals thermodynamically favor the (002) plane. We further calculated the binding energies of S_8 and Li_2S_8 molecules on various facets of β-S_8 as shown in Figure 4.10h and Figure 4.11. Both the redeposition of liquid S_8 in electrolyte and the electrochemical oxidation of sulfur from Li_2S_8 prefer to happen on the (020) plane.

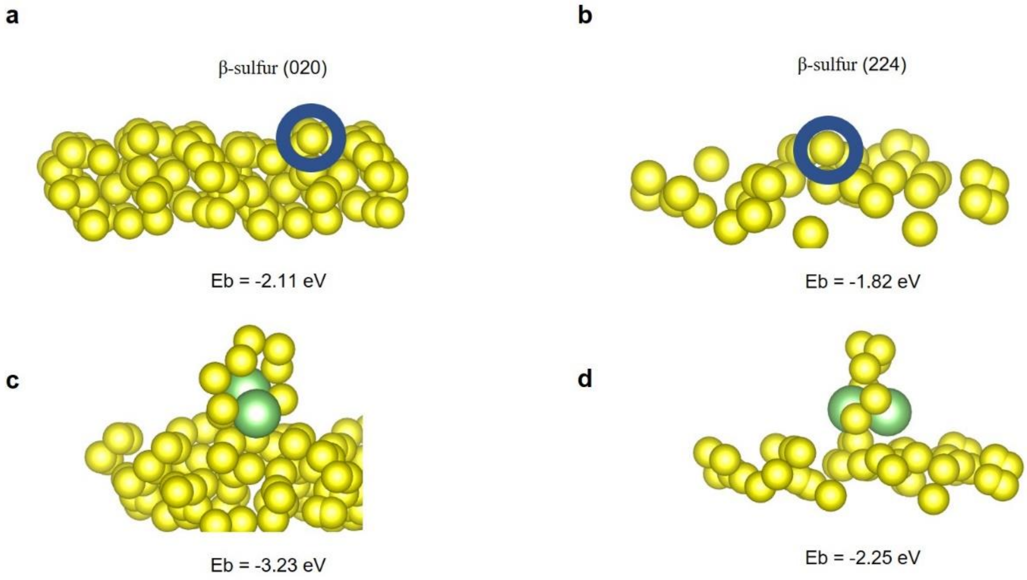

Figure 4.11 The binding energy of sulfur molecular with a. (0 2 0) plane b. (2 2 4) plane

of β-sulfur.

Different from the hybrid iso-anisotropic sulfur growing dynamics, the sulfur crystals dissolved isotropically during the discharging process, regardless of the crystallographic orientations and the accessibility of electrons (Figure 4.12a). The dissolution of polycrystalline sulfur became faster when the size was below ~8 μm (Figure 4.12b, c) (~0.015 μm s^{-1} to 0.35 μm s^{-1}). On the other hand, the dissolving rate of single-crystal sulfur was more uniform (Figure 4.12d). When we consider the single and polycrystalline sulfur as a whole part for dissolution kinetic analysis, it also presents a uniform dissolving process (Figure 4.12e), suggesting a high percentage of single-crystal sulfur in the final product. This observation contradicts the common belief that the insulating sulfur particles require electronic conduction to be discharged in a Li-S cell. It can be attributed to the disproportional reaction between residual polysulfides in electrolytes and sulfur particles ($S_8 + Li_2S_{3-5} \rightarrow Li_2S_{6-8}$). Furthermore, the intensified Raman peaks demonstrated the recovery of long-chain polysulfides during discharging at 405 and 453 cm^{-1} (Figure 4.13) and the light-to-dark yellow color change (Figure 4.11a) in the micro-cell. This finding suggests the excellent reversibility of sulfur crystals in cycling Li-S batteries.

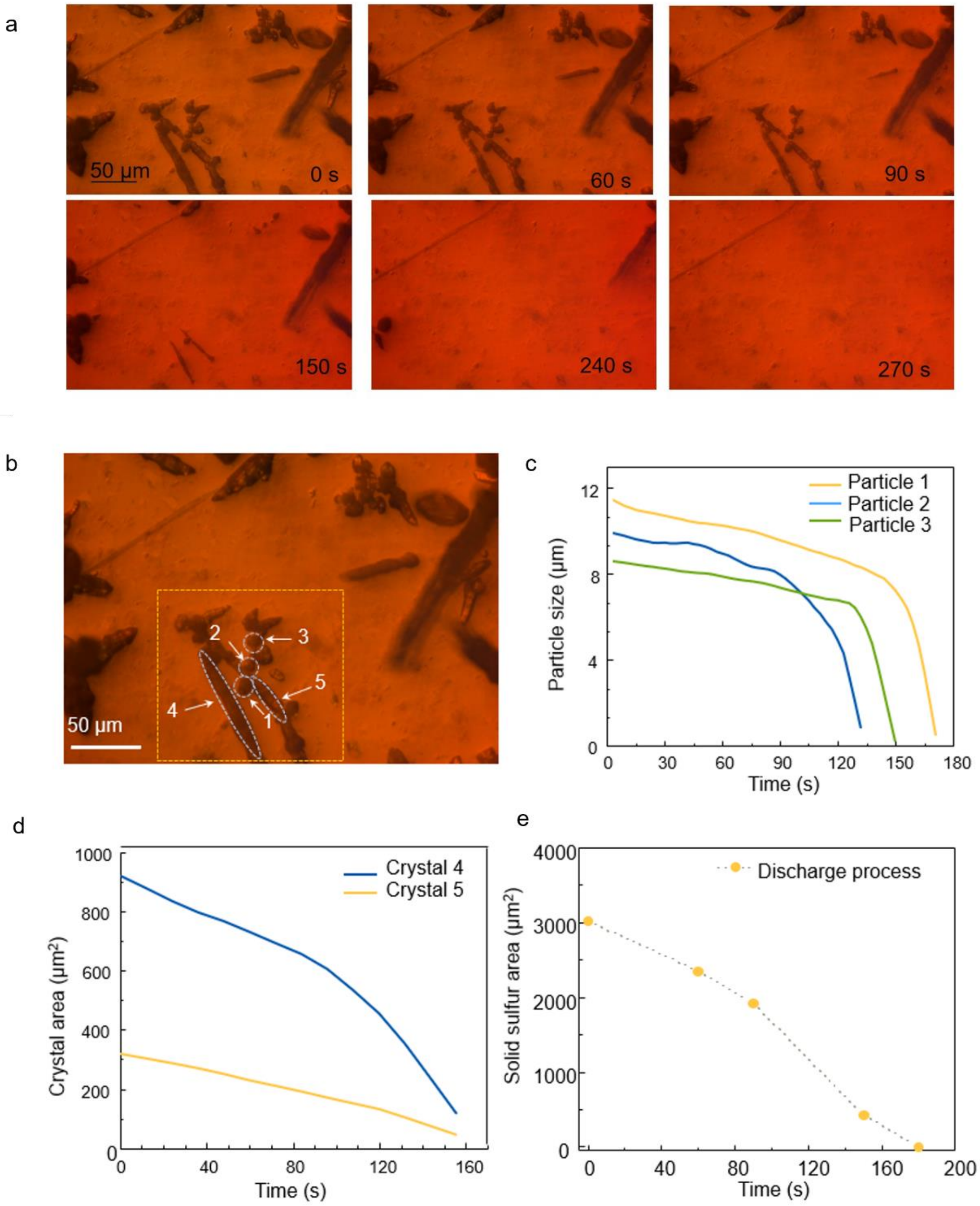

Figure 4.12 a. The optical images of the solid sulfur dissolution process. b. The optical image of the selected area to analyze the dissolution process of solid sulfur, which are marked 1, 2, 3, 4, 5 (1-3: polycrystalline sulfur; 4, 5: single crystal sulfur). c. The particle size as a function of time. d. The area changes of particle 4, 5. e. The area changes of the selected whole part.

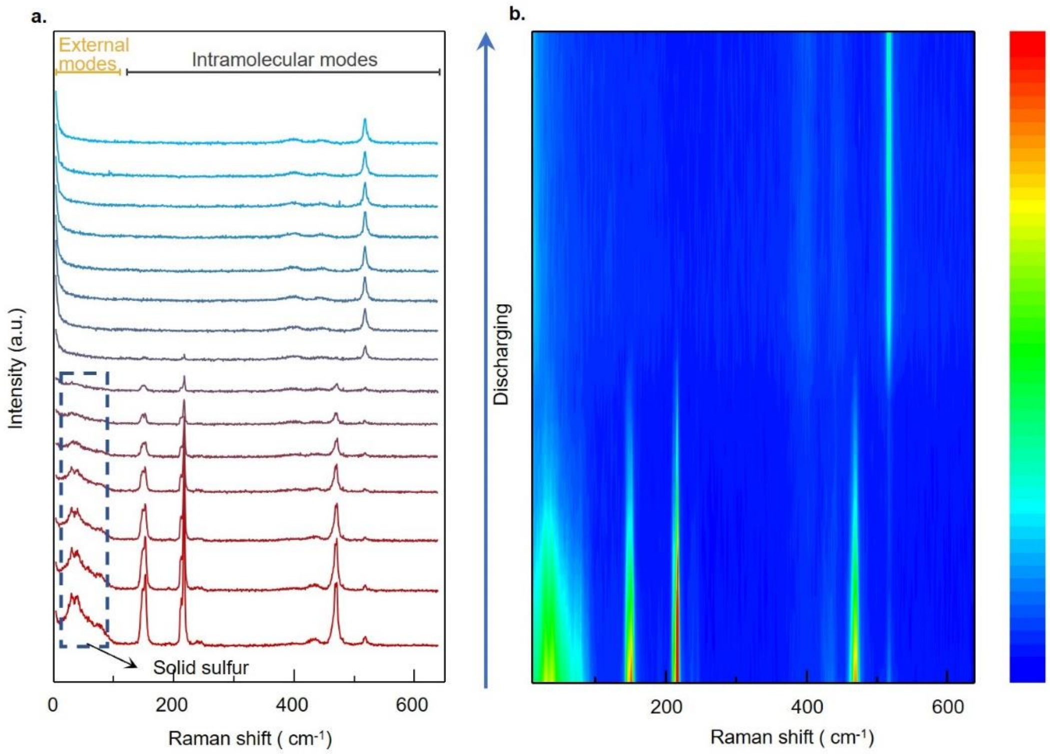

Figure 4.13 a. *In situ* Raman spectra of the discharging process of S_8 reduction to long chain polysulfides and b. the corresponding contour pattern.

4.1.4 Liquid sulfur formation at different current densities

The above analyses of the sulfur growing dynamics and phase transition signify that liquid sulfur plays a significant role in the charging process. Liquid sulfur appears as the charging intermediate from Li_2S_8 to solid sulfur. The droplets can benefit solid sulfur growth and regulate its orientation. Compared to the extensively investigated solid sulfur, liquid sulfur has rarely been explored, especially its role in regulating the electrochemical performance of Li-S batteries. Furthermore, the sulfur deposition is sensitive to current densities, further influencing the charging capacity in real batteries. Hence, the following section will discuss the correlation between current density and liquid sulfur formation.

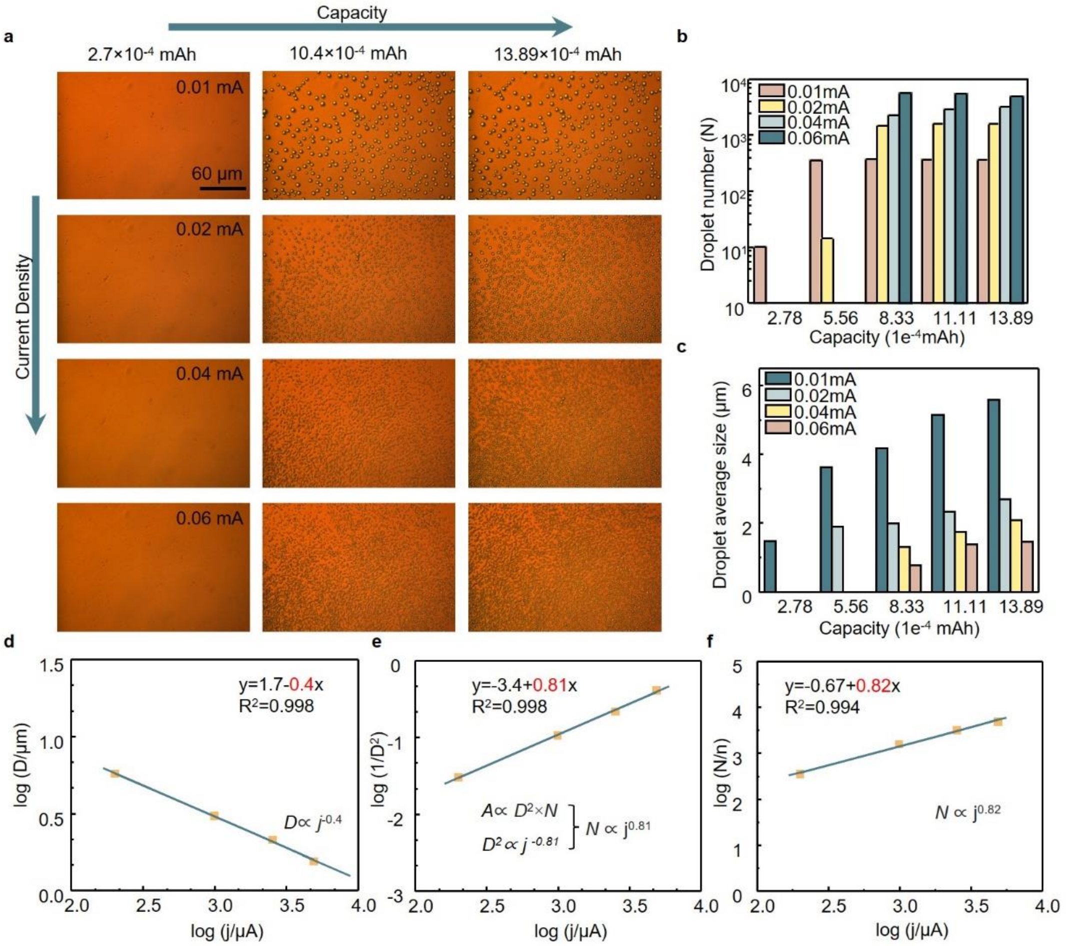

Figure 4.14 a. Optical image of liquid sulfur generation at different current densities at a fixed capacity. b. The particle number distribution at different current densities at a fixed capacity. c. The particle size distribution at different current densities at a fixed capacity. d. The plots of the double logarithmic relationship of the droplet geometric mean diameters versus the current density. e. The plot of the double logarithmic relationship of the inverse of the square of the geometric mean diameter of the droplet versus the current densities. f. The plot of the double logarithmic relationship of the droplet number versus the current densities.

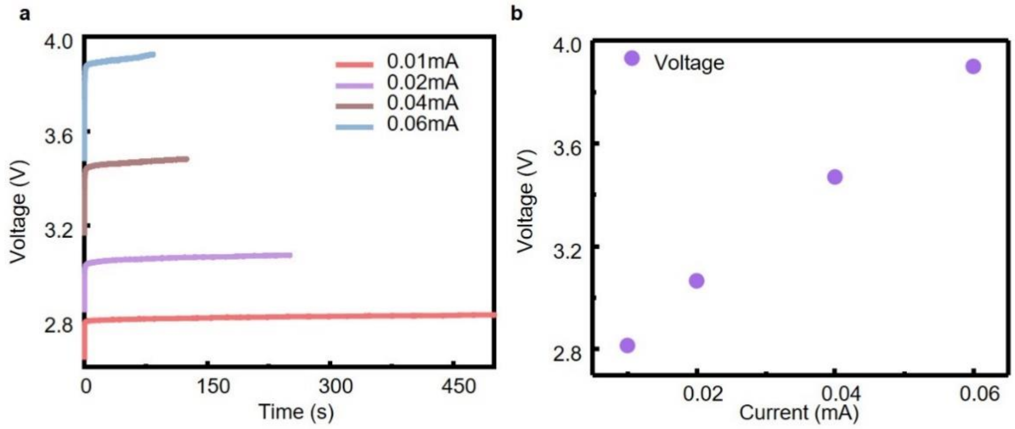

Figure 4.15 a. The voltage changes with time at a constant current. b. The voltage at the end of charging and the corresponding current.

The electrochemical generation of liquid sulfur from catholyte was conducted to explore the influence of current density on the size and density of liquid sulfur droplets (Figure 4.14a). When a driving force of 60 μA was applied, the overpotential approached at ~3.9 V *vs.* Li/Li^+ immediately (Figure 4.15), which is close to the electrochemical stability window of the electrolyte. Therefore, we limited the applied current to 60 μA in this study. Statistical analysis of the droplet number and size under the same capacities reveals that the liquid sulfur became smaller and denser as the current densities increased, as shown in Figure 4.14 b-c. The final droplet size formed at 10 μA is more than 3 times larger than that created at 60 μA (5.36 μm vs. 1.54 μm). Furthermore, the droplet density enlarged by more than 16 times (total particle number of 356 vs. 4904 in the selected area) as the charging rate increased from 10 to 60 μA. The particle sizes followed the Gaussian distribution (Figure 4.16), suggesting that the liquid sulfur growing process is associated with the classical Kolmogorov-Avrami-Mehl-Johnson (KAMJ) random nucleation theory.[140]

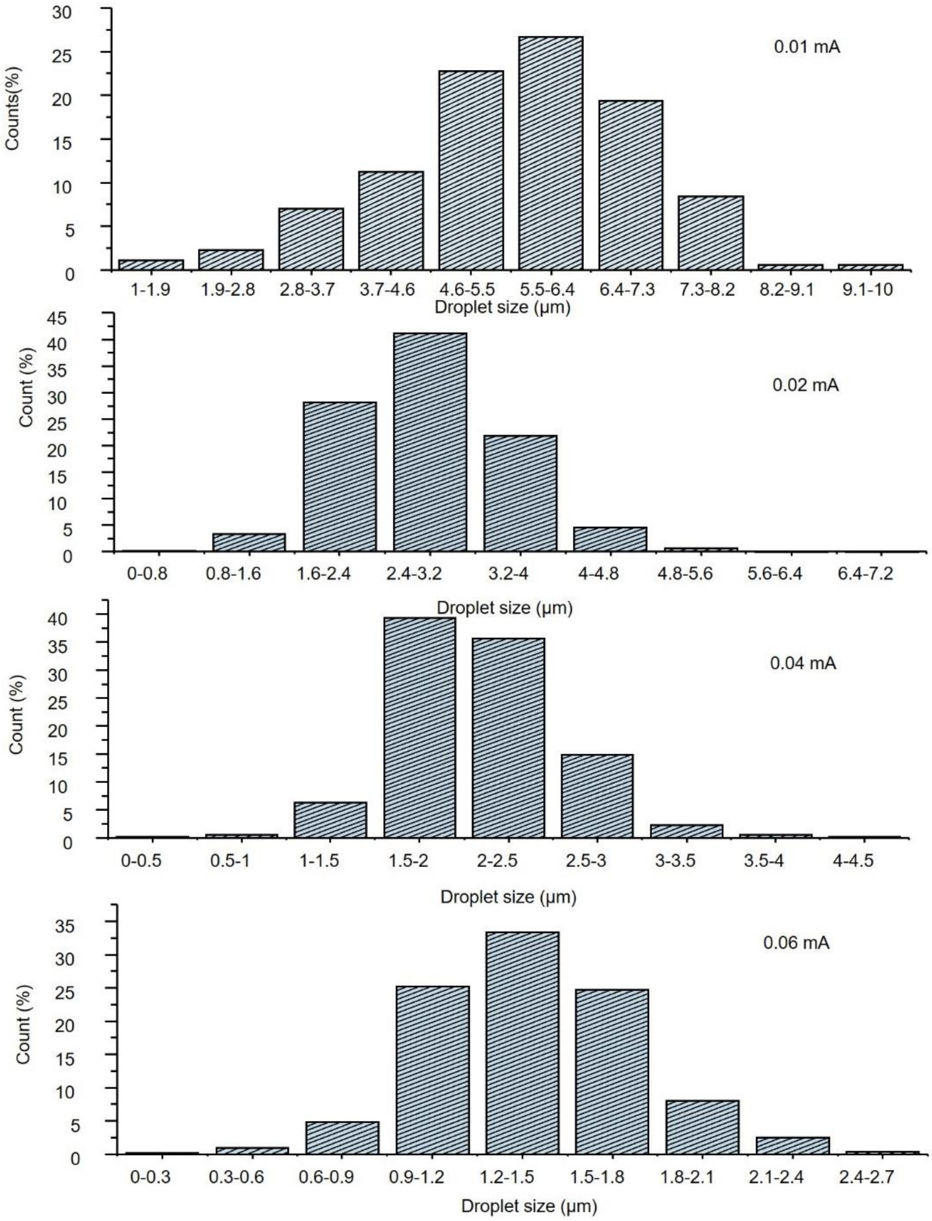

Figure 4.16 The particle size distribution under different current densities.

The above observations imply the dependence of droplet density and size on the current densities. A plot of the logarithm of *D* (quadratic mean of droplet sizes) versus the logarithm of current density *j* exhibited a linear relationship (Figure 4.14d). The line has a slope of -0.4 and an R-squared of 0.998. Hence, *D* displayed a proportional relationship with $j^{-0.4}$, as shown in Eqn (23).

$$D \propto j^{-0.4} \tag{24}$$

We assumed the liquid sulfur fully occupied the conductive surface of graphene. Therefore, the theoretical number of droplets (N_t) should be inversely proportional to D^2 on a fixed surface area (A). The logarithm of $1/D^2$ versus the logarithm of current density j displayed a linear relationship with a 0.81 slope and 0.998 R-squared (Figure 4.14e). Therefore, the relationship between N_t and j can be built in Eqn (18).

$$N_t \propto j^{0.81} \tag{25}$$

By counting the number of droplets in actual conditions, we can plot the logarithm of N_r (droplet number in real) and log (j) in Figure 4.14f. Interestingly, the log (N_r) also indicates a linear relationship to log(j) with a 0.994 R-squared and a slope of 0.82. Apparently, the N_r is very close to N_t, allowing our further estimations by directly using N_r to estimate the relationship between charging current (j) and capacity (Q).

According to Faraday's laws of electrolysis, the charging capacity should be proportional to the volume (V) and the number (N_r) of the charging product. If the droplets are regarded as ideal spheres with an identical growth rate along the radius direction, the relationship between Q and V, N_r of the charging product can be built in Eqn (19).

$$Q \propto D^3 \times N_r \tag{26}$$

$$Q \propto j^{-0.39} \tag{27}$$

Taking Eqn 17 and 18 into Eqn 19, it is found that Q is approximately proportional to $j^{-0.39}$, which signifies an inverse relationship between the current density and the charging capacity. If heat loss is not considered in the electrochemical system, the size of sulfur droplets is inversely proportional to the cubic root of the droplet number under a constant capacity. Clearly, the current significantly influences the droplet size and numbers. Interestingly, the charging capacity for the above liquid sulfur analyses is fixed, arguing against our institution that the charging capacity should depend on current densities, especially in actual batteries. The unique features of liquid sulfur can interpret abnormal results. During the charging process, sulfur is generated on the surface of the graphene. Due to liquid sulfur's mobility and reshaping properties, they would release the conductive surface by merging into larger droplets to occupy less surface area.

In contrast, the solid sulfur charging product would occupy the surface with a thin reaction product layer and low charging capacities. This comparison illustrates that liquid sulfur can deliver higher charging capacities than solid sulfur (or expected capacities) on the same conductive surface.[17,130] Therefore, it is unsurprising that the capacities are almost constant by increasing the current from 10 to 60 μA.

Electrochemical performance of liquid-sulfur mediated cathodes

The above finding suggests that introducing liquid sulfur can be a feasible strategy for fast-charging Li-S batteries. To be a proof-of-concept, we chose graphene on nickel foam (G-Ni) and electrospun carbon nanofibers (CNF) as two representative cathode hosts, where the former indicates solid sulfur formation (Figure 4.17), whereas liquid sulfur is generated on the latter (Figure 4.18a). To characterize the fast-charging ability, the CNF cathode with Li_2S_8 catholyte is charged at 0.1 C and gradually increased to 3 C (at a constant discharging rate of 0.1C). The charging capacity of Li_2S_8/CNF cathode is shown in Figure 4.18b. The first 5 cycles exhibited increasing capacities and slight fluctuation due to the activation process. The cells indicated capacities of 1147 mAh g^{-1}, 1080 mAh g^{-1}, 1028 mAh g^{-1}, 1001 mAh g^{-1}, 974 mAh g^{-1}, 944 mAh g^{-1} at 0.1 C, 0.2 C, 0.5 C, 1 C, 2 C, and 3 C, respectively. The capacity retention is more than 82 %, increasing the current density by 30-folds. When the charging rate is recovered to 0.5 C, a reversible capacity of 966 mAh g^{-1} was retained, illustrating excellent cyclic stability of the liquid-sulfur-involved Li-S batteries.

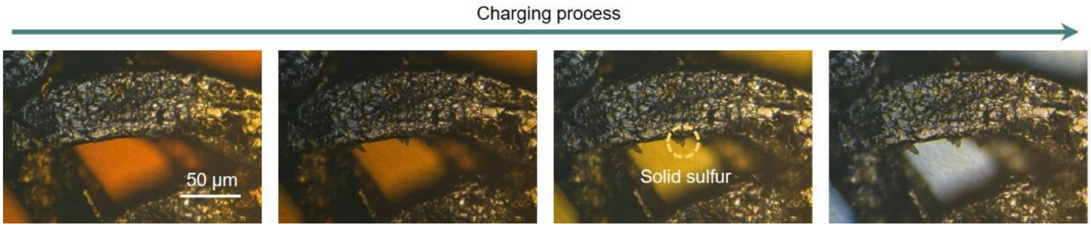

Figure 4.17 The optical image of solid sulfur formation on the graphene Ni foam.

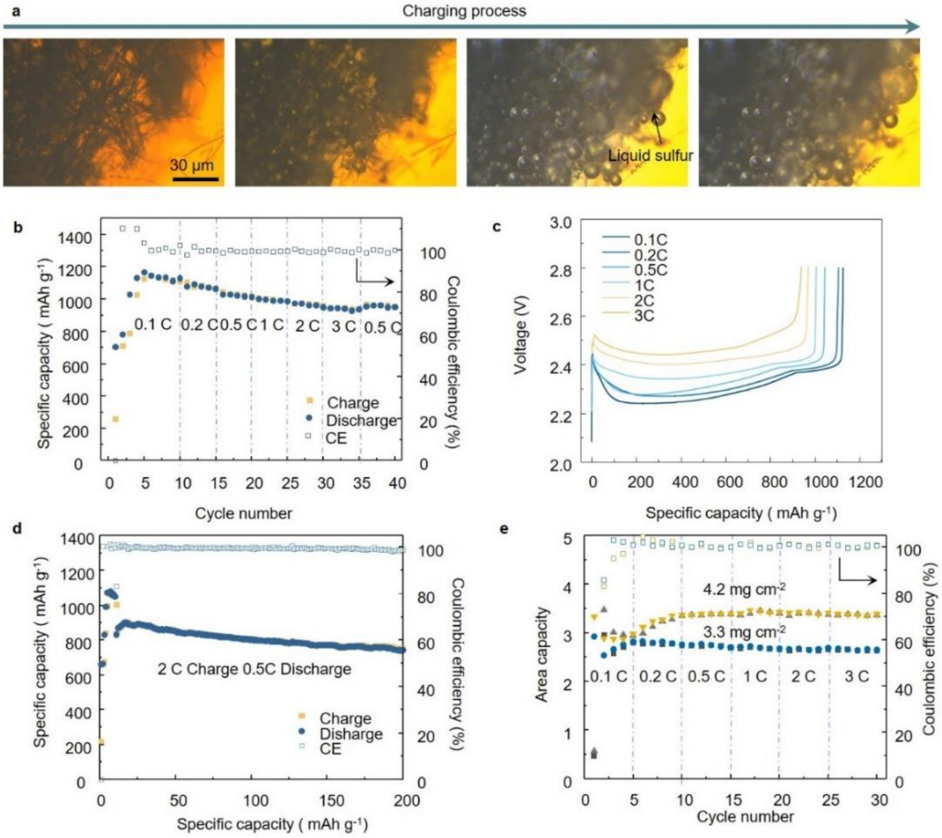

Figure 4.18 a. Optical images of liquid and solid sulfur generation on CNFs. b. Rate

performance of the CNF electrode at different charge current densities and 0.1 C discharge current density. c. Charge voltage profiles of CNFs cathode at different charge current densities d. Cycling performance and Coulombic efficiency of the CNFs electrode at 0.5 C discharge and 2 C charge for 200 cycles. e. Rate performance of the high-loading CNF electrode at different charge current densities and 0.1 C discharge current density.

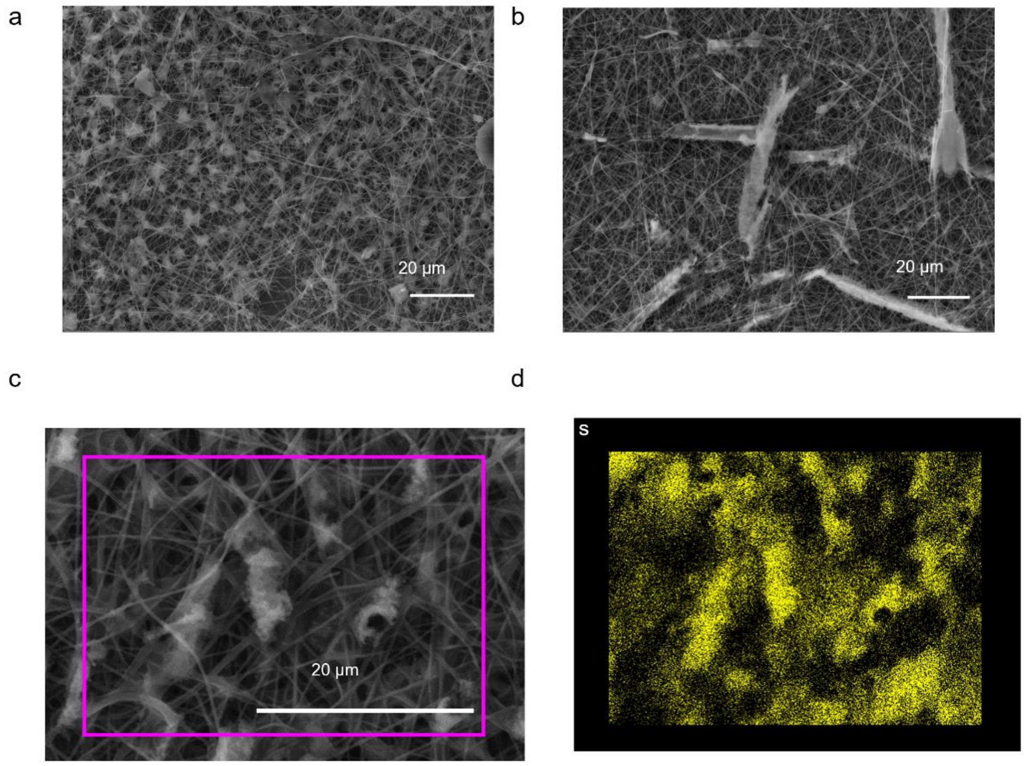

Figure 4.19 a. The SEM image of spherical-like solid sulfur. b. The SEM image of needle-like solid sulfur. c. The SEM image of selected areas CNF d. and the corresponding EDS-mapping.

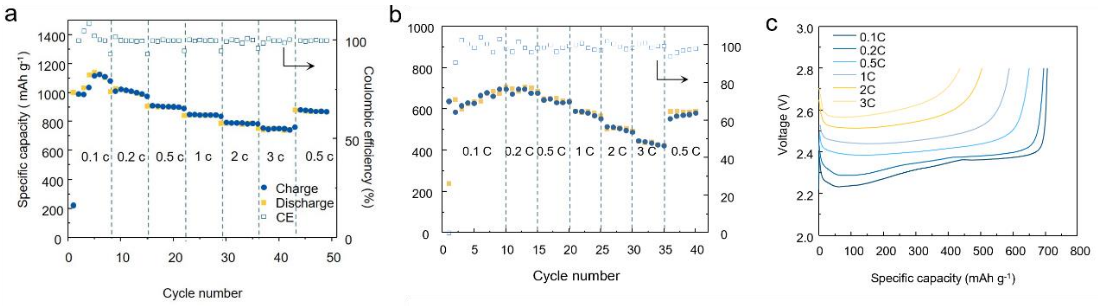

Figure 4.20 a. The rate performance of CNFs under 0.1 C, 0.2 C, 0.5 C, 1 C, 2 C, 3 C. b. Rate performance of the graphene/Ni foam cathode at different charge current densities and 0.1C discharge current density. c. Charge voltage profiles of graphene/Ni foam cathode at different current densities.

We believe the high-rate capacity relates to the liquid sulfur formed on the CNFs. The sulfur droplets served as the intermediate phase to postpone the passivation of the CNF surfaces by the solid sulfur phase. The liquid-solid sulfur phase transition in a working Li-S cell occurred at the end of charging. The SEM images presented needle-shaped and spherical sulfur particles on the CNF host (Figure 4.19), similar to the results on graphene substrates. To identify the impact of liquid sulfur on the charging process, we cycled the CNF-based cathode under galvanostatic charging and discharging programs from 0.1 C to 3 C. A capacity retention of only 66 % is obtained (Figure 4.20a), which is attributed to the incomplete reduction of Li_2S at the high-rate discharging process. The G-Ni foam-based cathodes were also cycled under the same measurement conditions. As shown in Figure 4.20b, c, a capacity retention of 63 % was observed for the pure solid-sulfur formation systems. The charging voltage profiles for G-Ni-based cathode indicated large polarizations and short plateaus at high rates (Figure 4.20c), in sharp contrast to the long-charging plateaus of Li_2S_8/CNF in Figure 4.18c. The differences demonstrate the influential role of liquid sulfur in accelerating the charging kinetics in Li-S batteries.

Long-term cycling was also performed for the liquid-sulfur Li-S system. We cycled the Li_2S_8/CNF cathode by charging at 2 C/discharging at 0.5 C, which exhibited remarkable capacity retention of 751 mAh g^{-1} after 200 cycles (Figure 4.18d). Li-S batteries with high sulfur loading and lean electrolyte parameters were also cycled at different current densities to identify the practical feasibility of liquid sulfur. As a result, the Li-S cells can indicate areal capacities of 2.6 mAh cm^{-2} and 3.6 mAh cm^{-2} at 3 C charging with high sulfur loadings of 3.3 mg cm^{-2} and 4.2 mg cm^{-2} (Figure 4.18e), respectively. The high-rate charging performance of the Li-S cells displayed a competitive electrochemical performance even without the aid of catalysts, as shown in Table 4.1, further demonstrating the promise of liquid sulfur chemistry. Compared with others, our work achieves 100% capacity retention in high-loading and lean electrolyte conditions. Findings in this work can promote the realization of practically high-power Li-S batteries, for example, by designing catalysts to facilitate equivalent reduction and oxidation kinetics for the discharging/charging processes in future works.

Table 4.1 Charging capacity comparison between our work and others in recent publications. The battery testing condition of others' work uses the same charge and discharge rate. Our work uses different charge rates and 0.1 C discharge rate.

Materials	E/S ratio (μL/mg)	Sulfur loading (mg/cm)	Areal capacity (2C)	Capacity retention (0.5C/2C)	Energy density (Wh kg^{-1})
$CoSe_2/Co_3O_4$@NC-CNT (cathode) [141]	/	2	1.56	78.70%	277.3(0.5C)
MoS_2-MoN/CNT(cathode) [142]	/	1.2	0.98	75.60%	146.2(0.5C)

Ni_3FeN/G(separator)[143]	16	1.2	1.09	86%	120.4(0.2C)
ZnSSnS@NC(separator)[27]	12	2.2	2.06	81%	158.9(1C)
ZnS, Co–N–C(cathode)[144]	7	1.2	1.06	~81%	148.3(0.6C)
$CoSe_2$/G(separator)[145]	15	1	0.97	87%	111.9(0.5C)
Nb−SAs@NC(cathode)[146]	15	2	1.97	88%	211.9(1C)
MSC/P⊂$NiTe_{2-x}$(separator)[26]	15	1.8	1.62	79.80%	163.2(1C)
Rhizopus hyphae carbon fiber(separator)[147]	20	2	1.56	77%	96.5(1C)
$CoNiO_2$/Co_4N/graphene(cathode) [148]	15	1	0.85	87%	95.3(0.5C)
CNF (this work)	9.5	4.2	3.44	100%	141.0(3C)

4.2 Conclusion

We identified sulfur's nucleation and growth dynamics on a graphene substrate based on *in situ* Raman and optical microscope observations. Following the formation of metastable liquid sulfur, single- and polycrystalline sulfur particles appeared upon further charging the micro-electrochemical cells. The single-crystal sulfur anisotropically grew along the (224) orientation, while the polycrystalline particles were derived from liquid sulfur droplets. Quantifying the growing dynamics of liquid sulfur droplets as a function of current density reveals that the size and number density are susceptible to applied current, whereas the areal capacities are almost intact. This remarkable finding is ascribed to the less dependence of liquid sulfur growth on the substrate surface area, which signifies the possibility of fast-charging liquid-sulfur cathodes. As a proof-of-concept, we prepared CNF/Li_2S_8 cathodes enabling a liquid sulfur-associated Li-S system. The new Li-S batteries demonstrated negligible capacity loss, even increasing the charging current densities by 30-fold, which rivals the state-of-the-art high-rate performance in literature. It is believed that the liquid-sulfur electrochemistry proposed in this work would unlock a new avenue toward fast-charging Li-S batteries.

Chapter 5 Liquid sulfur deposition kinetics through electrochemical oxidation

In Chapter 4, we observed sulfur formation on single-layer graphene. Though we suggest liquid sulfur is hard to keep as the final charging product, it has the potential to help the Li-S batteries achieve fast charging. It is important to understand the reaction kinetics of the electrodeposition of liquid sulfur.

5.1 Introduction

As shown in Figure 5.1a, the liquid sulfur deposition process includes three steps: I. the polysulfides, as reactants, arrive at the reaction surface; II. the polysulfides lose electrons to form sulfur; III. the electrons are transported through the external circuit. Step I is related to mass transport, and Step II and III can decide the charge transfer kinetics. Any step can be a major factor in determining the kinetics of electrochemical reactions. For example, if step II is the rate-limiting step, the electrochemical reaction kinetics are determined by the reaction kinetics of S_8^{2-} to S_8, no matter how fast the mass transfer or the conductivity of the cathode material is. If the conductivity of the cathode host and reaction kinetics of S_8^{2-} to S_8 are large enough, the electrochemical reaction kinetic will be controlled by the kinetic of reactants arriving reaction surface. The effects of electrode kinetics and mass transport of species on liquid sulfur deposition have been inspected in this research. The influence of cathode materials conductivity, catalysts, and temperature on the electrochemical kinetics have been observed through the optical cell on carbon film (derived from the carbonization of PAN film) under a constant voltage, as shown in Figure 5.1b. This work reveals that excellent conductivity, efficient catalysts, and suitable temperature favor liquid sulfur deposition kinetics.

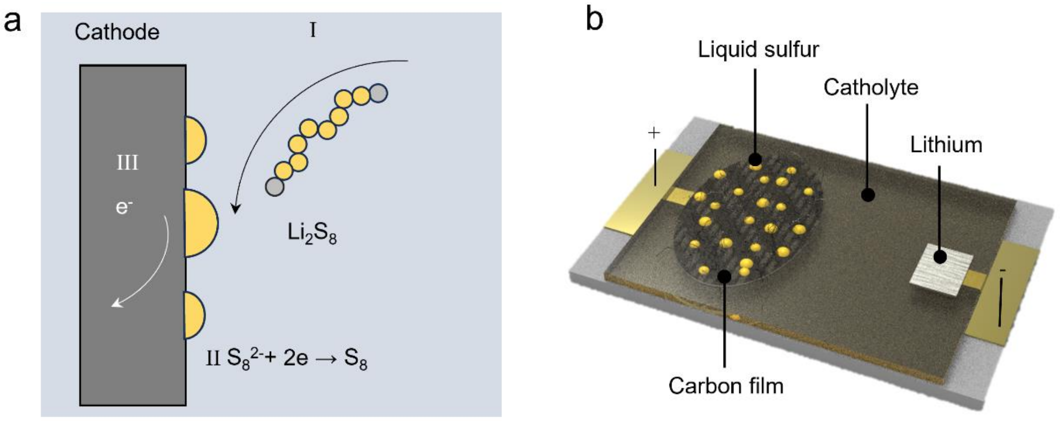

Figure 5.1 a. The schematic of the Li_2S_8 oxidation process. b. The schematic of the optical cell.

5.2 Discussion

5.2.1 Conductivity

This research used polyacrylonitrile (PAN) as a precursor to producing carbon film with different thermal treatment temperatures. Through stepwise carbonization between 650 °C and 1050 °C, the conductivity of carbon film can be tailored to explore the relationship between liquid sulfur formation behavior and charge transfer of substrate. After annealing, the PAN-based carbon film on the SiO_2/Si wafer can keep intact. XRD results display that the carbon film keeps the amorphous structure between 650 °C and 1050 °C (Figure 5.2).

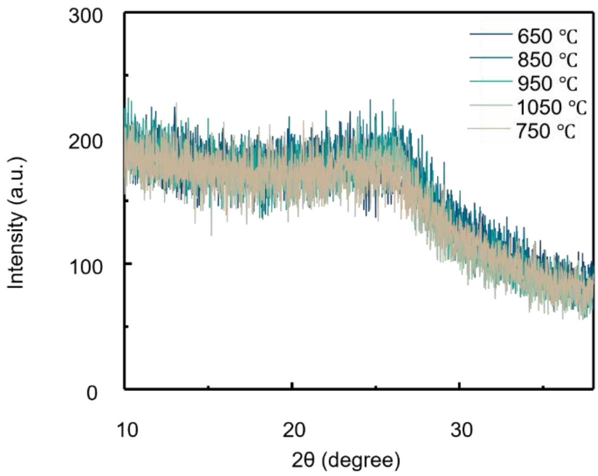

Figure 5.2 The XRD spectra of PAN-based carbon film at different annealing temperatures.

The stepwise carbonization process also results in the surface chemistry change. The surface chemistry change was analyzed by SEM, as shown in Figure 5.3. The surface of CNF films has abundant N and O elements, and the content of O has a little increase before 950 °C (6.96% to 13.42%) and then decreases to 5.32%. N content gradually decreases with the temperature increase, from 25.93% at 650 °C to 8.91% at 1050 °C. Besides, the carbon content gradually increases from 67.12% to 85.86% during stepwise carbonization. These results demonstrate that N and O functional groups on the carbon surface have been removed significantly at 1050 °C.

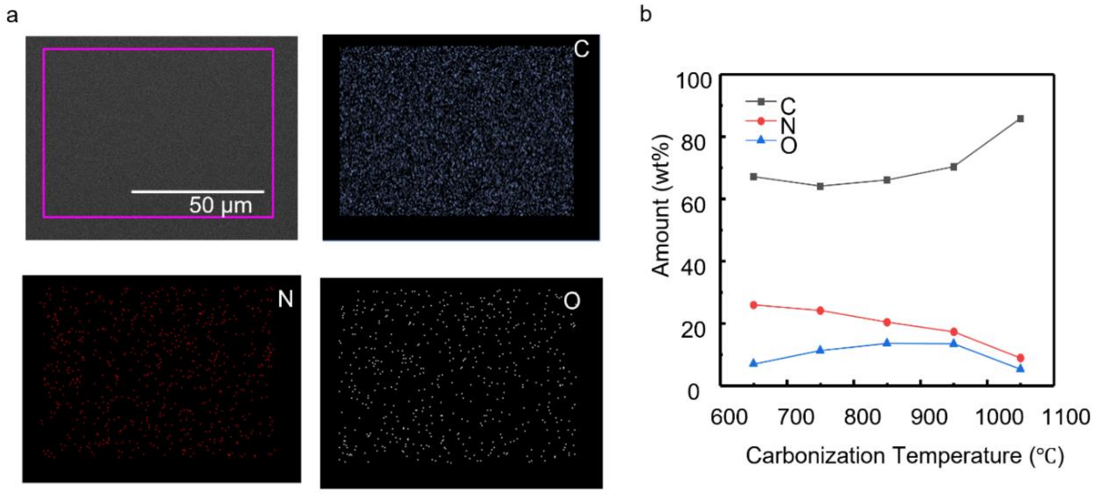

Figure 5.3 a. The SEM images of PAN-based carbon film and related EDS mapping at 950 °C. b. The amount change of C, N, and O under different temperatures.

The sheet resistance (R_{sr}) of carbon films was measured through four-probe conductivity measurements, and the testing results are presented in Figure 5.4. R_{sr} is the electrical resistance of a thin film of material, measured in ohms per square (Ω/sq). It is calculated by dividing the resistivity of the material by its thickness. Therefore, the sheet resistance of carbon film is inversely proportional to electric conductivity. Three different samples were prepared at the same annealing temperature to minimize the effects of random error and ensure the measurements' accuracy. Each sample was measured three times, and the average of the three values was used as the result. At 650 ℃, the PAN-based carbon film (650 °C carbon film) has the largest R_{sr} and the R_{sr} become smaller as the temperature increase. From 950 °C (39.213 Ω/sq) to 1050 °C (28.07 Ω/sq), the decrease about R_{sr} is negligible (Figure 5.4b).

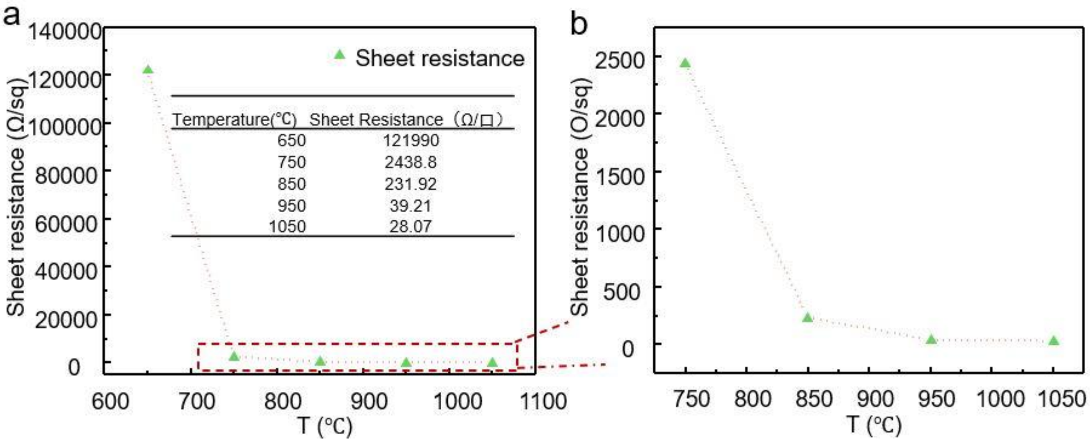

Temperature(℃)	Sheet Resistance（Ω/□）
650	121990
750	2438.8
850	231.92
950	39.21
1050	28.07

Figure 5.4 a. The sheet resistance of carbon film at 650 ℃, 750 ℃, 850 ℃, 950 ℃, 1050 ℃. b. The sheet resistance of carbon film at different temperatures film at 750 ℃, 850 ℃, 950 ℃, 1050 ℃.

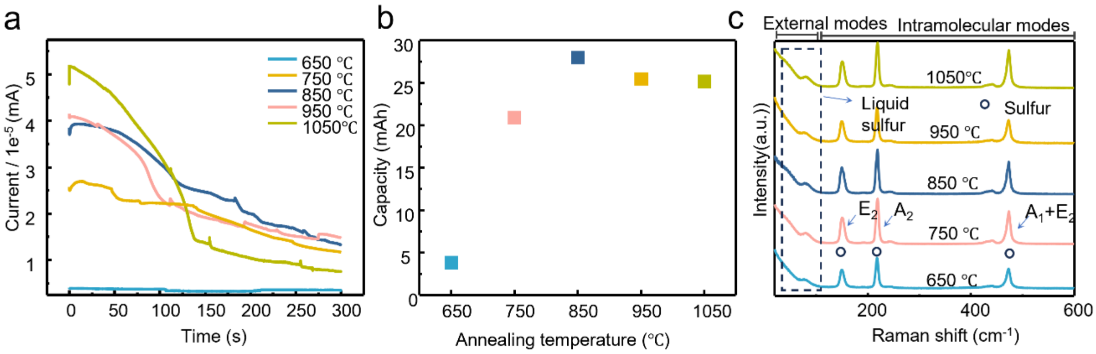

Figure 5.5 a. The I-t curves of LiPSs electrochemical oxidation at 3V on PAN-based carbon film with different annealing temperatures. b. The capacity of the charging process of LiPSs electrochemical oxidation at 3 V on PAN-based carbon film with varying annealing temperatures. c. The Raman spectra of liquid sulfur generation on PAN-based-carbon film with different annealing temperatures.

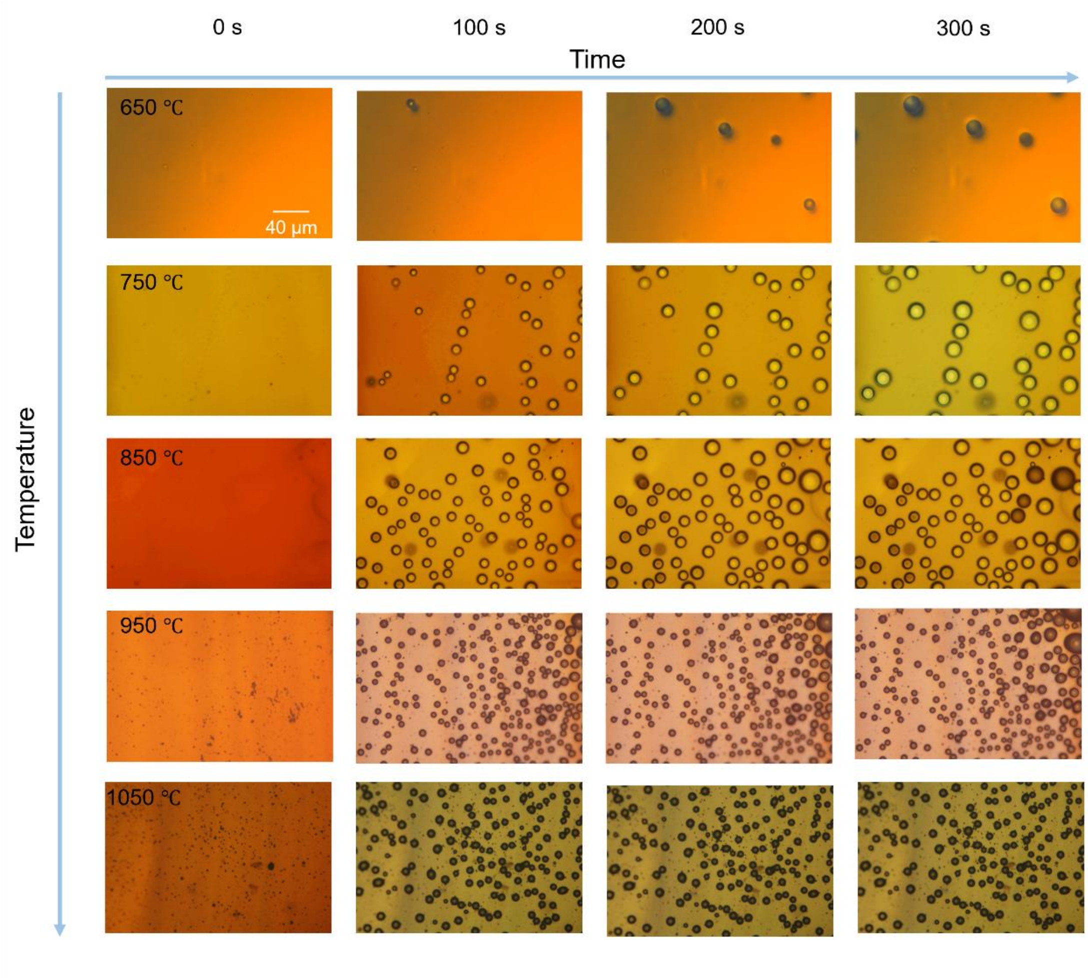

Figure 5.6 The optical images of sulfur generation at 3V on PAN-based carbon film with different annealing times.

The current as a function of time was recorded when a constant current was applied to the optical cell. The resulting I-t curve and related optical images are shown in Figure 5.5a and Figure 5.6. We observed the spherical charging product generated on the carbon film (Figure 5.6) and the liquid sulfur is confirmed by Raman Figure 5.5c. The peaks on 150, 220, and 473 cm^{-1} of Raman are attributed to the asymmetric S-S bending mode, the symmetric S-S bending mode and the S-S stretching mode of sulfur. A Rayleigh wing feature in external modes illustrates that sulfur is liquid sulfur. Raman and optical images show that liquid sulfur can be generated on the PAN-based carbon film (annealing range between 650 °C and 1050 °C). It is found that the reaction current is minimal on 650 °C annealed PAN-based carbon film (650 °C carbon films) in the whole charging process. In contrast, the reaction current keeps one order of magnitude for 750 -1050 °C carbon film, indicating that the conductivity of PAN-based carbon film will not significantly influence the reaction kinetics when the annealing temperature is over 750°. This conclusion is also reflected by the charging capacity of different samples, as shown in Figure 5.5b.

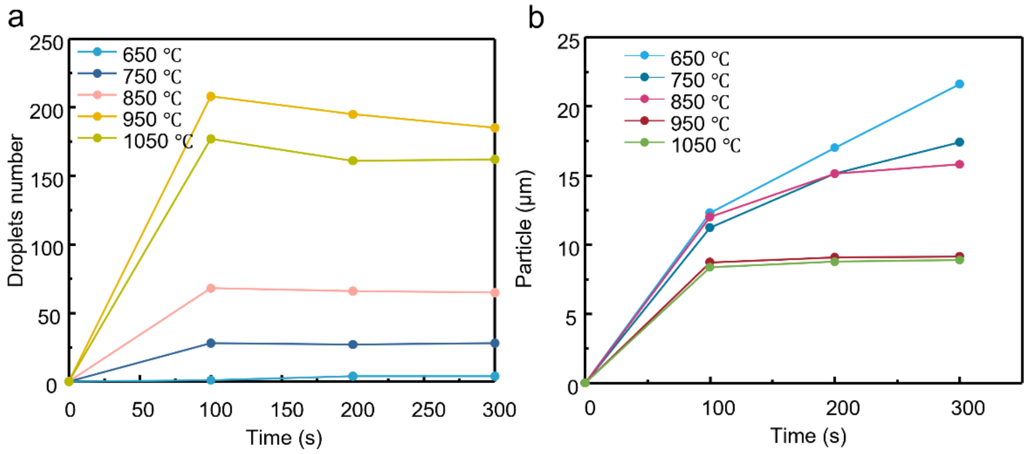

Figure 5.7 a. Statistics of the number of droplets and b. size on different annealed temperature PAN-based carbon films.

From the optical images (Figure 5.6), we found that the liquid growth behavior is related to the conductivity. The relationship between the annealing temperature and droplet number as well as particle size, are summarized in Figure 5.7. With the increase of annealing temperature, the number of droplets increased while the size decreased except for 950 °C and 1050 °C- carbon films, both the numbers and size of droplets on 950 °C and 1050°C- carbon films were very close (Figure 5.7a). High conductivity carbon will bring more reaction sites, leading to many sulfur droplet formations (Figure 5.7b). For the carbon substrate with relatively low conductivity, the solution-mediated pathway helps the liquid sulfur growth. Results show that particle growth behavior can be affected by carbon conductivity instead of the functional groups.

Moreover, the catholyte concentration change was analyzed according to the gray value of the catholyte in the video. The gray value is inversely proportional to the concentration of polysulfides in the catholyte; the larger the gray value, the lower the concentration of polysulfides in the electrolyte. The catholyte RGB colors were converted to grayscale values and then analyzed the average grayscale value by Image J, as shown in Figures 5.8 a-e. The change tendency between the grayscale and sulfur area keeps consistent. It is worth noting that an unstable testing environment may cause some fluctuations in the grayscale of the 850-carbon film. The relationship between I and $t^{-0.5}$ becomes linear in the middle and late stages of the reaction (after ~120s), as shown in Figure 5.8 e-h, indicating that the reaction becomes diffusion-controlled (Cottrell equation). In the initial stages, the charge transfer on the interface controls the reaction. The rate constant k can be calculated based on the formula:

$$-\frac{d[Li_2S_8]}{dt}=k[Li_2S_8]^n \tag{28}$$

The fit results display the n=1, and 750 °C-carbon film shows the smallest k of $\sim 8\times10^{-4}$, the 1050 °C, 950 °C, and 850 °C -carbon films have similar k values of around 2.8×10^{-3}, 2.4×10^{-3}, and 2.4×10^{-3} respectively. The results illustrate that the conductivity of carbon film has few influences on the charge transfer process.

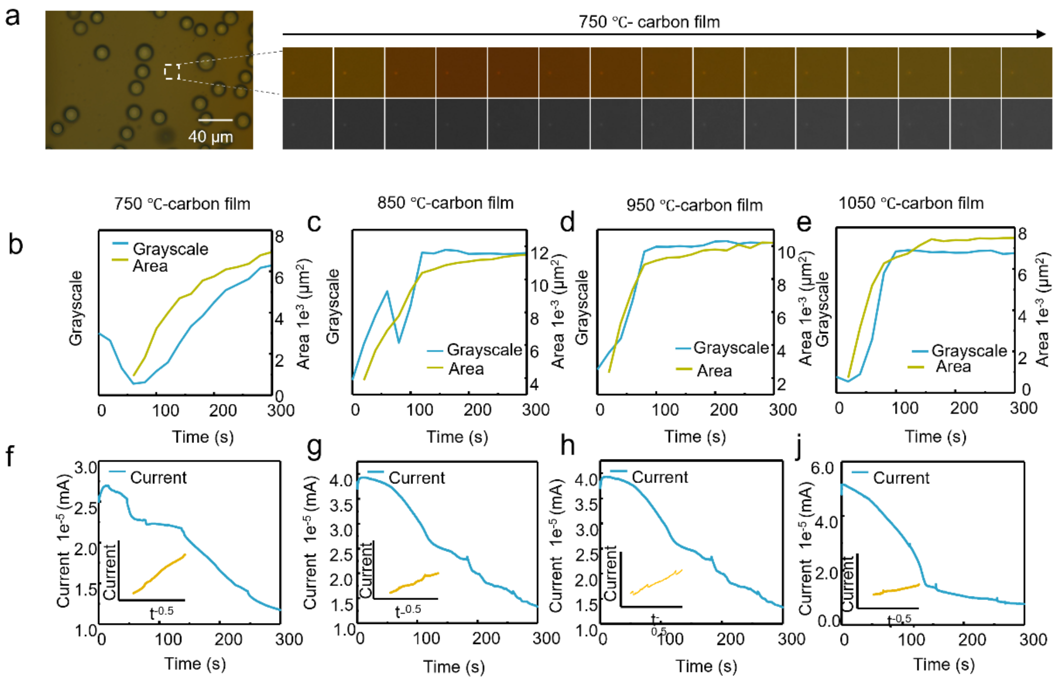

Figure 5.8 a. Monitoring the RGB color variation and conversion RGB color to 8-bit grayscale image. Liquid sulfur area and catholyte gray value variation on b. 750 °C, c. 850 °C, d. 950 °C, e. 1050 °C carbon film in the charging process. The I-t curve of f. 750°C, g. 850 °C, h. 950 °C, i. 1050 °C carbon film at 3V (insets show the relationship between I and $t^{-0.5}$ in the middle and late stages of the reaction).

According to the Cottrell equation:

$$i = \frac{\mathrm{nFAc_j^0}\sqrt{\mathrm{D_j}}}{\sqrt{\Pi \mathrm{t}}} \tag{29}$$

n is the number of electrons, F is Faraday constant and A is the electrode area (we assume all the samples have the same area of ~6 mm^2), c_j^0 is the initial concentration of reactants, the D_j diffusion coefficient can be calculated. The D_j for this reaction is ~4.88±3.25 10^{-8} cm^2 S^{-1}.

5.2.2 Catalysts

Liquid sulfur has been observed on a metal substrate like Au, Pd, and Pt.[14] Among them, Pt works as an electrocatalyst and has been applied to Li-S batteries system.[153-155] Through the electron-beam physical vapor deposition, 10 nm and 1 nm Pt films have been prepared on the 950 °C-carbon film. A constant voltage of 3 V was applied to the optical cell to observe the process of lithium polysulfide oxidation to liquid sulfur. To our surprise, we found that liquid sulfur prefers to form on the surface of the carbon film rather than Pt, as shown in Figure 5.9. The amount of liquid sulfur on the carbon film far exceeds that on the Pt surface.

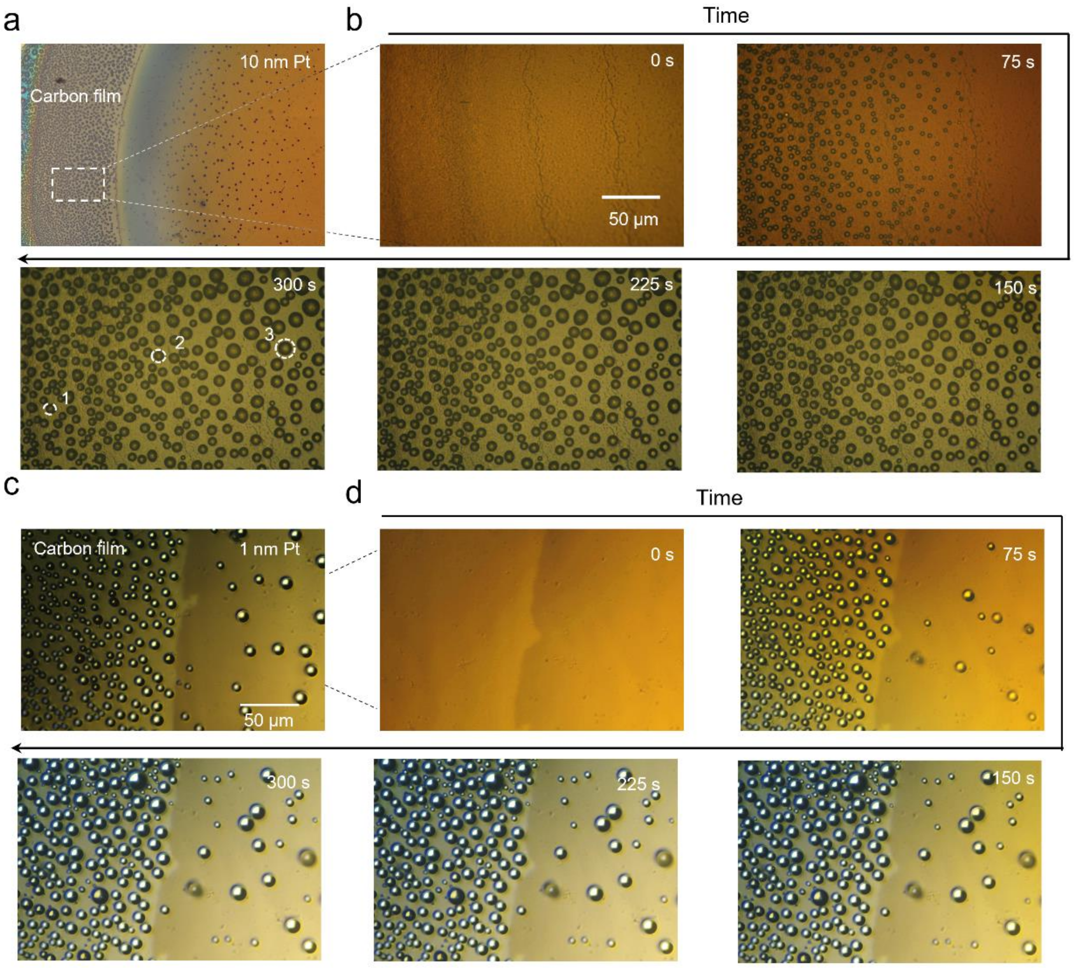

Figure 5.9 a. b The optical images of liquid sulfur generation on the carbon zone of 10 nm Pt-carbon film. c, d The optical images of liquid sulfur generation on the carbon zone and Pt zone of 1nm Pt-carbon film.

The I-t curves show that the 10 nm Pt-carbon film has a larger current response than the 1nm Pt (Figure 5.10 a, b). The I-t curve of the carbon film with Pt dropped steadily, while that of the carbon film dropped suddenly (Figure 5.8). In Figure 5.10a, I and $t^{-0.5}$ show a linear relationship illustrating that the reaction becomes the diffusion control after 100 s on 10 nm Pt-carbon film, and the related diffusion coefficient is about 5.26×10^{-4} cm^2 S^{-1}, consistent with the pure carbon system. The reaction on 1 nm Pt-carbon film has not shifted to diffusion-controlled after the end charging process (Figure 5. 10b). The 10 nm Pt-carbon film displays a larger capacity than 1 nm-Pt carbon film. The change of the gray value of the catholyte is consistent with the change of the liquid sulfur area (Figure 5.11a), and the change reaction constant on 10 nm Pt-carbon film can be calculated around 2×10^{-3}. The k values are similar with/without Pt because the Pt film provides only limited reaction sites, resulting in k reflecting an average value between the carbon and Pt regions. Therefore, we suggest the real k for this system in the carbon zone is larger than the pure carbon system. Three droplets in three different places are analyzed on 10 nm Pt-carbon film. These droplets formed at the initial stage and grew without merging. According to the particle growth behavior (1,2,3 in Figure 5.9b) the droplets closest to the carbon and Pt interface have the largest size, fastest growth kinetics, and longest growth time (Figure 5.11b). The droplet size and number are compared between 10 nm Pt-carbon film and carbon film (Figure 5.12). Droplet sizes are similar on both substrates (Figure 5.12b), but there are almost 1.5 times as many droplets on the 10 nm Pt-carbon film as on pure carbon (Figure 5.12a). Based on the observation of liquid sulfur generation on 10 nm Pt-carbon film, 1 nm Pt-carbon film, and pure carbon film, we claim Pt as the catalyst can help the Li_2S_8 oxidation process but is not a suitable substrate for the accumulation of liquid sulfur. A higher capacity of 10 nm Pt-carbon film can be attributed to more deposition sites emerging in the carbon zone because of some Pt nanoparticles in the carbon zone.

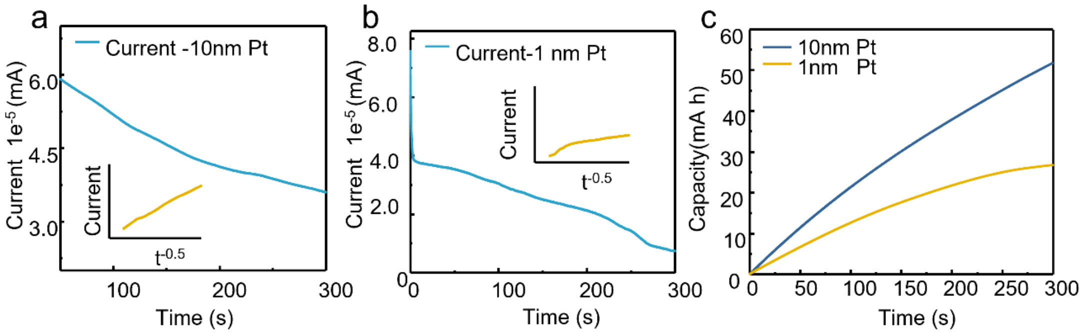

Figure 5.10 The I-t curves of a. 10 nm Pt- carbon film and b. a. 1 nm Pt- carbon film at 3V (insets show the relationship between I and $t^{-0.5}$ in the middle and late stages of the reaction). c. The capacity comparison between 10 nm Pt- carbon film and 1 nm Pt-carbon film.

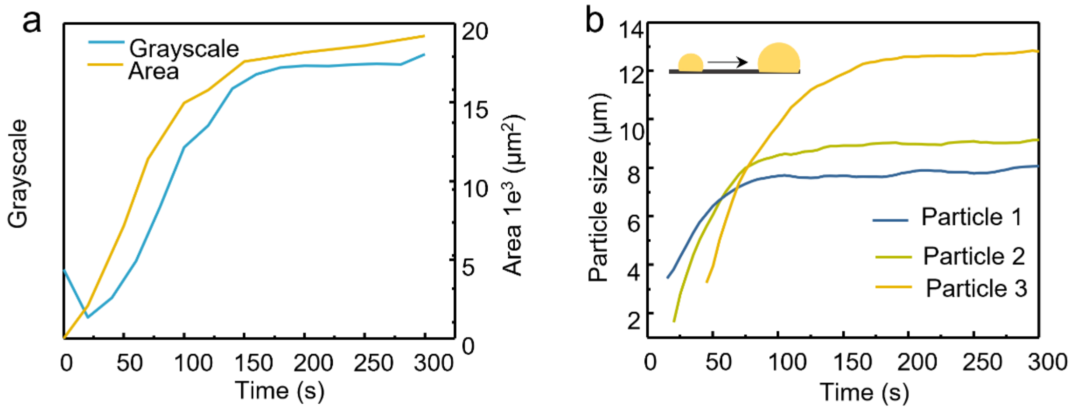

Figure 5.11 a. Liquid sulfur area and catholyte gray value variation on 10 nm Pt-950°C carbon film in the charging process. b. Size change of three droplets grown in a 10 nm Pt-950°C carbon film during charging.

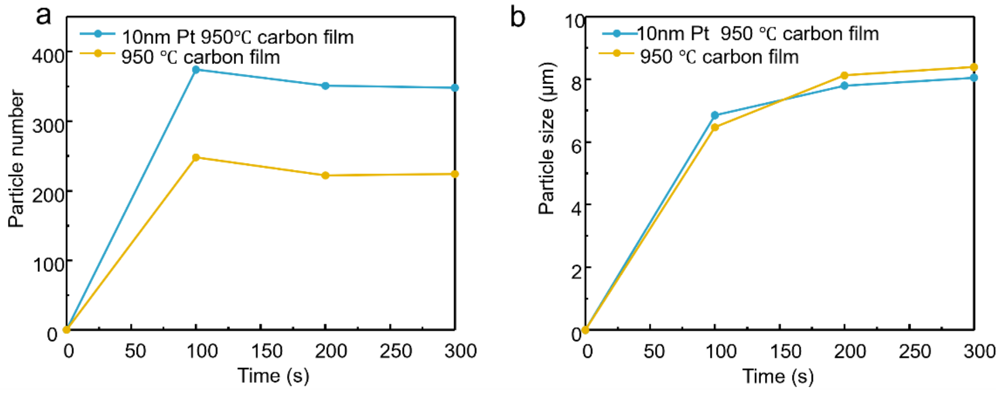

Figure 5.12 a. Statistics of the number of droplets and b. size on 10 nm Pt-950 °C carbon film and 1 nm Pt-950 °C carbon film.

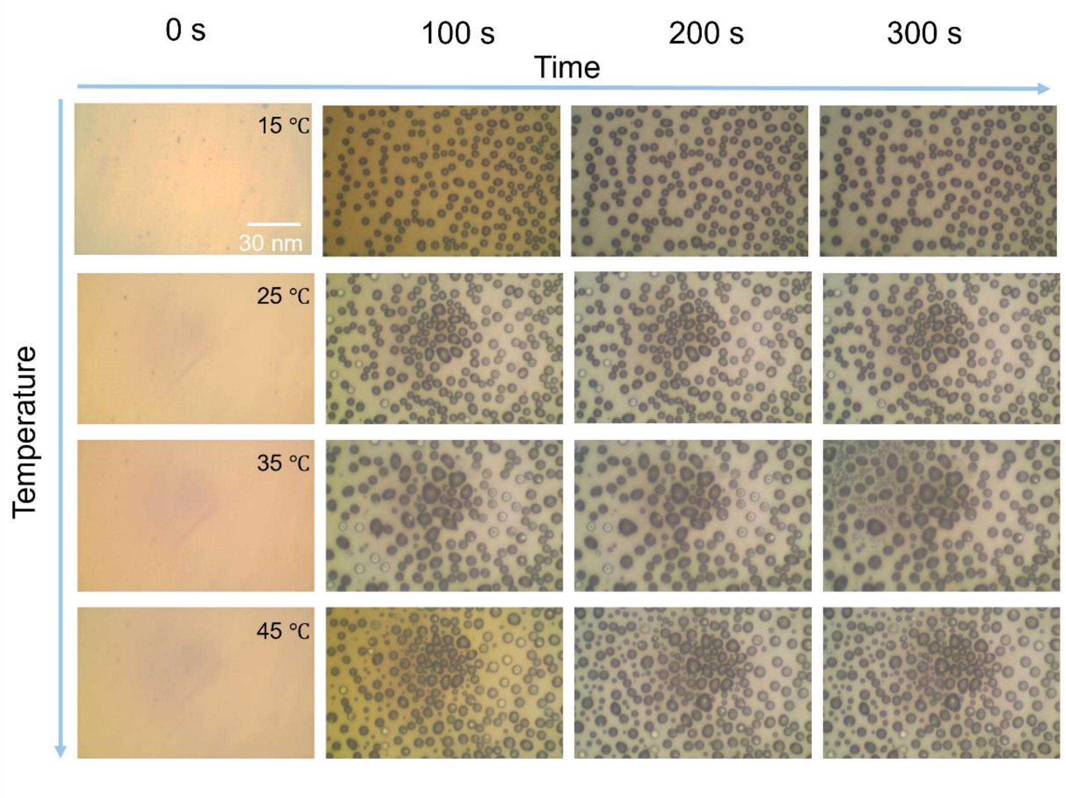

Figure 5.13 The optical images of liquid sulfur generation on the 950 °C carbon film carbon at 15 °C, 25 °C, 35 °C, and 45 °C.

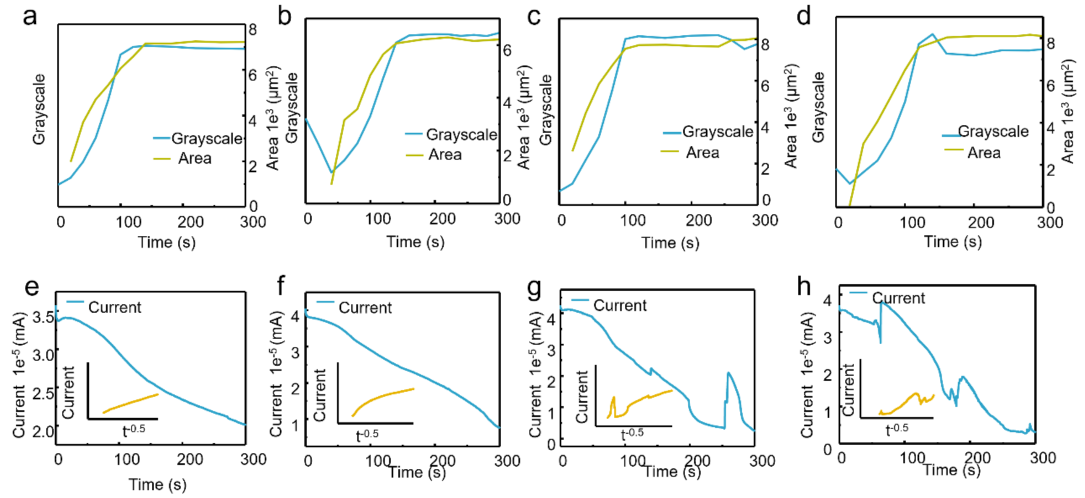

Figure 5.14 Liquid sulfur area and catholyte gray value variation at a. 15 °C, b. 25 °C, c. 35 °C, d. 45 °C on 950 °C-carbon film in the charging process. The I-t curve of e. 15 °C, f. 25 °C, g. 35 °C, h. 45 °C carbon film at 3V (insets show the relationship between I and $t^{-0.5}$ in the middle and late stages of the reaction).

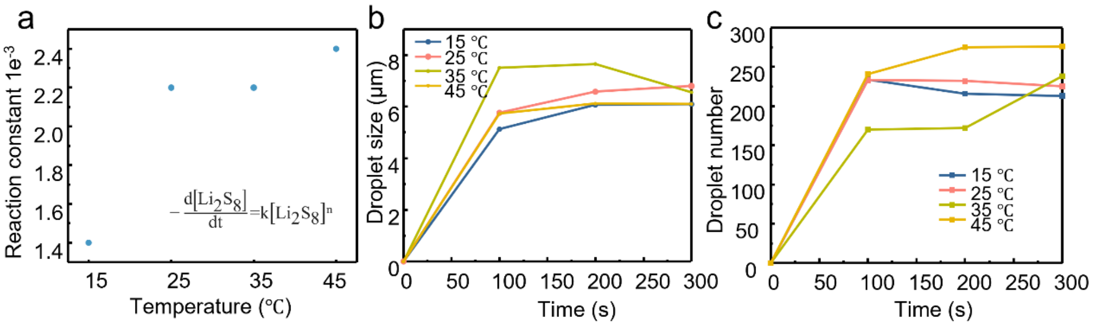

Figure 5.15 a. The reaction constant at different temperatures. b. The variation of droplets' average size in the charging process. c. The variation of droplets number in the charging process.

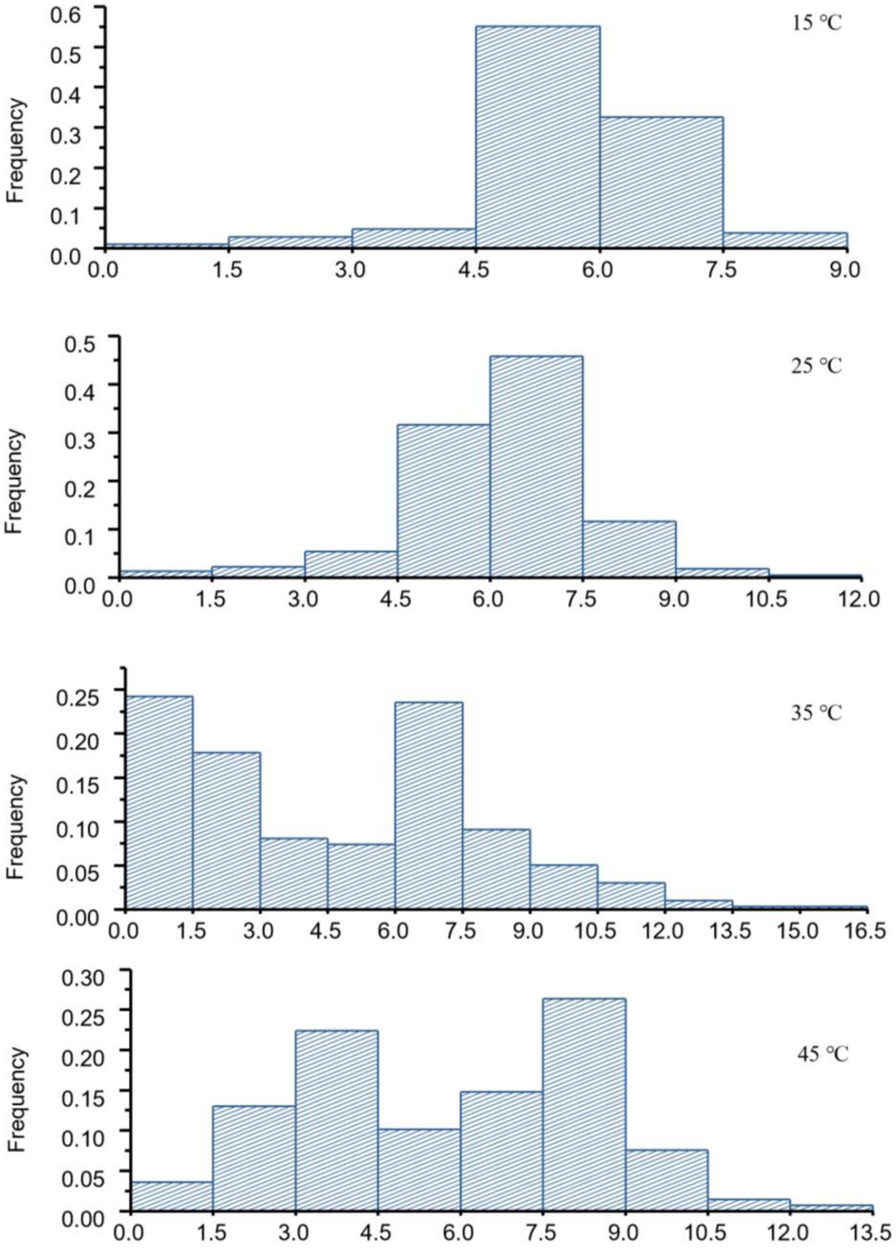

Figure 5.16 Statistics of droplet size distribution at different temperatures.

5.2.3 Temperature

Changing the temperature will affect the reaction barrier and mass transport process. We observed the sulfur droplet deposition at 15 °C, 25 °C, 35 °C and 45°C as shown in Figure 5.13. The change of gray value in catholyte, sulfur droplet area, and current are recorded in Figure 5.14. Gray value and sulfur droplet area show a positive correlation at any temperature (Figure 5.14 a-d). According to the gray value, we calculate the kinetic constant at different temperatures and found that after 25 °C, the temperature has limited influence on the reaction constant, as shown in Figure 5.15a. The reason may be that increasing the temperature lowers the energy barrier of the polysulfide oxidation process and improves the reaction kinetics of the reverse reaction (metastable liquid sulfur decomposition).

Increasing the temperature makes the unstable of the current curve (Figure 5.14 e-f), and the current suddenly increases because of the large droplet generation on the surface as shown in the highlighted circle in Figure 5.14g. Except at 15 °C, the reaction does not turn into diffusion control before the charging process end (Figure 5.14 e-f). The diffusion coefficient at 15 °C is around 1.4×10^{-8} cm^2 S^{-1}, slightly lower than the room temperature. At the end of charging, the currents at 35 °C and 45 °C are lower than those at 25 °C, indicating that higher temperatures benefit the decomposition of liquid sulfur. The statistical data about the average size and number of sulfur droplets at different temperatures are shown in Figures 5.15 b, c, and 5.16.

Though the average size at the end of charging is similar, the distribution has a significant difference. Most of the droplet sizes at 15 °C and 25 °C are in the 4.5-7.5 μm range, while the particle size distribution was broader at 25°C than at 15°C due to increased reaction and coalescence kinetics. At 35°C, the particle size distribution is broadest, indicating that the coalescence process and growth kinetics favor droplet growth. A large number of droplet formation on the substrate induces the particle number increase, as shown in Figure 5.15 c. At 45°C, the particle size distribution is relatively average, and the particle number is the largest. By analyzing the results, increasing the temperature will increase the mass transfer, thereby creating more reaction sites on the substrate and bringing more liquid sulfur to progressive deposit on the substrate. The higher temperature does not bring higher reaction kinetics because it accelerates the liquid sulfur decomposition kinetics.

5.3 Conclusion

The charge transfer and mass transport effect on liquid sulfur deposition have been observed in this research. At room temperature, the reaction kinetics are dominated by charge transfer in the initial stage and followed by mass transfer. When the sheet resistance of carbon is less than 2400Ω/sq, the conductivity of carbon has a limited influence on the liquid sulfur deposition. Increasing temperatures favor mass transport and bring more reaction sites, while the kinetics constants are similar because the reaction kinetics of sulfur reduction and Li_2S_8 oxidation are improved simultaneously. In addition, liquid sulfur is easier to deposit on carbon than Pt film. Compared with the pure carbon system, more reactive sites appeared in the carbon region of the Pt/carbon film system. The rational design of Pt and carbon composites benefits liquid sulfur deposition. This work comprehensively studies liquid sulfur deposition kinetics and provides insights for designing cathode materials utilizing sulfur physical states.

Chapter 6 Conclusion and Future Work

6.1 Conclusion

In this thesis, we systematically study the deposition of liquid sulfur on different materials and the deposition kinetics. First, we observe sulfur generation on TMD materials and propose a general method to keep liquid sulfur in the charging process. In the second work, we use graphene as a substrate to explore the role of liquid sulfur and find that it favors fast-charging Li-S batteries. In the third work, we investigate how the charge transfer and mass transport influence on liquid sulfur deposition. The findings of each work are highlighted below:

(1) Liquid sulfur has a higher area capacity than solid sulfur on TMD nanoflakes due to its reshaping ability. However, solid sulfur nucleates on the edges of thick TMD nanoflakes. We found that H_2 annealing MoS_2 can preserve the liquid sulfur in the charging process even under harsh conditions (large overpotential and low temperature). Oxide and anion vacancies are introduced to the edge and basal plane of MoS_2 nanoflakes through H_2 annealing. The oxide reduces the uneven distribution of the electric field around the edges, suppressing solid sulfur nucleation. The anion vacancies favor fast reaction kinetics. This method is also suitable for other TMD materials.

(2) By observing the electrochemical generation of sulfur on single-layer graphene, we suggested that liquid sulfur, as a metastable state, is difficult to preserve as the final charging product. However, liquid sulfur plays a key role in Li-S batteries. The crystallography of solid sulfur and final areal capacity is related to the kinetics of liquid sulfur growth. Liquid sulfur is insensitive to current density, indicating that liquid sulfur

can be generated under large current densities. We developed a free-standing material for fast-charging Li-S batteries based on these findings.

(3) This research has studied the effects of charge transfer and mass transport on liquid sulfur deposition. At room temperature, the reaction kinetics are initially dominated by charge transfer, followed by mass transport. The conductivity of carbon has a limited impact on liquid sulfur deposition when the sheet resistance of carbon is less than 2400Ω/sq. Elevating the temperature is beneficial for mass transfer without affecting the reaction constants. Liquid sulfur is preferentially deposited on the carbon film rather than the platinum film, but the introduction of the platinum film will favore the reaction.

6.2 Future work

The thesis mainly focuses on liquid sulfur in the Li-S batteries system. Through microscope investigation, we observed the liquid sulfur formation in the charging process which is insensitive to the current density. Based on this finding, we proposed the fast-charging Li-S batteries can be achieved by controlling the physical state of sulfur. Some problems need to be further explored from the liquid sulfur direction.

1. We proposed that liquid sulfur can unlock the fast-charging ability of Li-S batteries. The Li_2S decomposition is a crucial step and needs to overcome the energy barrier. Is there any relationship between liquid sulfur and Li_2S?

2. Liquid sulfur can be generated at the extremely low temperature of -50 ℃ on H_2-MoS_2. According to this, is it possible to explore the potential materials for low-temperature Li-S batteries?

3. The main factor in deciding whether liquid sulfur or solid sulfur is formed is ambiguous. Is there any convincing mechanism to demonstrate how to control the physical state of sulfur during electrochemical oxidation?

4. We observe the generation of liquid sulfur in Li-S batteries on some specific substrates. Is this common in other metal-sulfur battery systems on the same substrate?

In addition, optical cells can provide clear images about the generation and growth of sulfur and the concentration of electrolytes. Through the utilization of optical cells, future work can be explored:

We have calculated the kinetic constant of Li_2S_8 oxidation based on the grayscale change in the third work. This method can also observe the LiPS color variation in the discharging process. The Li_2S deposition is a crucial step during the discharging process. The rational design of experiments may potentially explore the reaction constant for Li_2S deposition and decomposition.

References

Uncategorized References

(1) Seh, Z. W.; Sun, Y.; Zhang, Q.; Cui, Y. Designing High-Energy Lithium-Sulfur Batteries. *Chem. Soc. Rev.* **2016**, *45* (20), 5605-5634.

(2) Chung, S. H.; Chang, C. H.; Manthiram, A. Progress on the Critical Parameters for Lithium–Sulfur Batteries to Be Practically Viable. *Adv. Funct. Mater.* **2018**, *28* (28), 1801188.

(3) Wang, L.; Ye, Y.; Chen, N.; Huang, Y.; Li, L.; Wu, F.; Chen, R. Development and Challenges of Functional Electrolytes for High-Performance Lithium-Sulfur Batteries. *Adv. Funct. Mater.* **2018**, *28* (38), 1800919.

(4) Li, J.; Fleetwood, J.; Hawley, W. B.; Kays, W. From Materials to Cell: State-of-the-Art and Prospective Technologies for Lithium-Ion Battery Electrode Processing. *Chem. Rev.* **2022**, *122* (1), 903-956.

(5) Zhu, K.; Wang, C.; Chi, Z.; Ke, F.; Yang, Y.; Wang, A.; Wang, W.; Miao, L. How Far Away Are Lithium-Sulfur Batteries from Commercialization? *Front. Energy Res.* **2019**, *7*, 123.

(6) Ji, X.; Lee, K. T.; Nazar, L. F. A Highly Ordered Nanostructured Carbon-Sulphur Cathode for Lithium-Sulphur Batteries. *Nat. Mater.* **2009**, *8* (6), 500-506.

(7) Liu, T.; Hu, H.; Ding, X.; Yuan, H.; Jin, C.; Nai, J.; Liu, Y.; Wang, Y.; Wan, Y.; Tao, X. 12 Years Roadmap of the Sulfur Cathode for Lithium Sulfur Batteries (2009–2020). *Energy Storage Mater.* **2020**, *30*, 346-366.

(8) Chen, X.; Ji, H.; Rao, Z.; Yuan, L.; Shen, Y.; Xu, H.; Li, Z.; Huang, Y. Insight into

the Fading Mechanism of the Solid-Conversion Sulfur Cathodes and Designing Long Cycle Lithium–Sulfur Batteries. *Adv. Energy Mater.* **2021**, *12* (1), 2102774.

(9) Ding, Y.; Cheng, Q.; Wu, J.; Yan, T.; Shi, Z.; Wang, M.; Yang, D.; Wang, P.; Zhang, L.; Sun, J. Enhanced Dual-Directional Sulfur Redox Via Biotemplated Single-Atomic Fe-N2 Mediator Promises Durable Li-S Batteries. *Adv. Mater.* **2022**, e2202256.

(10) Zhou, J.; Liu, X.; Zhu, L.; Zhou, J.; Guan, Y.; Chen, L.; Niu, S.; Cai, J.; Sun, D.; Zhu, Y.; et al. Deciphering the Modulation Essence of P Bands in Co-Based Compounds on Li-S Chemistry. *Joule* **2018**, *2* (12), 2681-2693.

(11) Zhang, H.; Ono, L. K.; Tong, G.; Liu, Y.; Qi, Y. Long-Life Lithium-Sulfur Batteries with High Areal Capacity Based on Coaxial Cnts@Tin-Tio2 Sponge. *Nat. Commun.* **2021**, *12* (1), 4738.

(12) Li, R.; Rao, D.; Zhou, J.; Wu, G.; Wang, G.; Zhu, Z.; Han, X.; Sun, R.; Li, H.; Wang, C.; et al. Amorphization-Induced Surface Electronic States Modulation of Cobaltous Oxide Nanosheets for Lithium-Sulfur Batteries. *Nat. Commun.* **2021**, *12* (1), 3102.

(13) Zhong, Y.; Wang, Q.; Bak, S. M.; Hwang, S.; Du, Y.; Wang, H. Identification and Catalysis of the Potential-Limiting Step in Lithium-Sulfur Batteries. *J. Am. Chem. Soc.* **2023**, *145* (13), 7390-7396.

(14) Liu, N.; Zhou, G.; Yang, A.; Yu, X.; Shi, F.; Sun, J.; Zhang, J.; Liu, B.; Wu, C. L.; Tao, X.; et al. Direct Electrochemical Generation of Supercooled Sulfur Microdroplets Well Below Their Melting Temperature. *Proc. Natl. Acad. Sci.* **2019**, *116* (3), 765-770.

(15) Waluś, S.; Barchasz, C.; Bouchet, R.; Leprêtre, J.-C.; Colin, J.-F.; Martin, J.-F.;

Elkaïm, E.; Baehtz, C.; Alloin, F. Lithium/Sulfur Batteries Upon Cycling: Structural Modifications and Species Quantification by in Situ and Operando X-Ray Diffraction Spectroscopy. *Adv. Energy Mater.* **2015**, *5* (16), 1500165.

(16) Jung, S. C.; Han, Y.-K. Monoclinic Sulfur Cathode Utilizing Carbon for High-Performance Lithium–Sulfur Batteries. *J. Power Sources* **2016**, *325*, 495-500.

(17) Yang, A.; Zhou, G.; Kong, X.; Vila, R. A.; Pei, A.; Wu, Y.; Yu, X.; Zheng, X.; Wu, C. L.; Liu, B.; et al. Electrochemical Generation of Liquid and Solid Sulfur on Two-Dimensional Layered Materials with Distinct Areal Capacities. *Nat. Nanotechnol.* **2020**, *15* (3), 231-237.

(18) Zhou, G.; Ankun Yang; Guoping Gao; Xiaoyun Yu; Jinwei Xu; Chenwei Liu; Yusheng Ye; Allen Pei; Yecun Wu; Yucan Peng; et al. Supercooled Liquid Sulfur Maintained in Three-Dimensional Current Collector for High-Performance Li-S Batteries. *Sci. Adv.* **2020**, *6*, eaay5098.

(19) Zhang, S. S.; Tran, D. T. A Proof-of-Concept Lithium/Sulfur Liquid Battery with Exceptionally High Capacity Density. *J. Power Sources* **2012**, *211*, 169-172.

(20) Zou, Q.; Lu, Y. C. Solvent-Dictated Lithium Sulfur Redox Reactions: An Operando Uv-Vis Spectroscopic Study. *J. Phys. Chem. Lett.* **2016**, *7* (8), 1518-1525.

(21) Liu, Y.; Elias, Y.; Meng, J.; Aurbach, D.; Zou, R.; Xia, D.; Pang, Q. Electrolyte Solutions Design for Lithium-Sulfur Batteries. *Joule* **2021**, *5* (9), 2323-2364.

(22) Chen, Z.-X.; Zhang, Y.-T.; Bi, C.-X.; Zhao, M.; Zhang, R.; Li, B.-Q.; Huang, J.-Q. Premature Deposition of Lithium Polysulfide in Lithium-Sulfur Batteries. *Journal of Energy Chemistry* **2023**, *82*, 507-512.

(23) Yu, X.; Manthiram, A. A Class of Polysulfide Catholytes for Lithium-Sulfur Batteries: Energy Density, Cyclability, and Voltage Enhancement. *Phys. Chem. Chem. Phys.* **2015**, *17* (3), 2127-2136.

(24) Li, G.; Wang, S.; Zhang, Y.; Li, M.; Chen, Z.; Lu, J. Revisiting the Role of Polysulfides in Lithium-Sulfur Batteries. *Adv. Mater.* **2018**, *30* (22), e1705590.

(25) Xu, Z. L.; Lin, S.; Onofrio, N.; Zhou, L.; Shi, F.; Lu, W.; Kang, K.; Zhang, Q.; Lau, S. P. Exceptional Catalytic Effects of Black Phosphorus Quantum Dots in Shuttling-Free Lithium Sulfur Batteries. *Nat. Commun.* **2018**, *9* (1), 4164.

(26) Yao, W.; Tian, C.; Yang, C.; Xu, J.; Meng, Y.; Manke, I.; Chen, N.; Wu, Z.; Zhan, L.; Wang, Y.; et al. P-Doped Nite$_2$ with Te-Vacancies in Lithium-Sulfur Batteries Prevents Shuttling and Promotes Polysulfide Conversion. *Adv. Mater.* **2022**, *34* (11), e2106370.

(27) Yao, W.; Zheng, W.; Xu, J.; Tian, C.; Han, K.; Sun, W.; Xiao, S. Zns-Sns@Nc Heterostructure as Robust Lithiophilicity and Sulfiphilicity Mediator toward High-Rate and Long-Life Lithium-Sulfur Batteries. *ACS Nano* **2021**, *15* (4), 7114-7130.

(28) Chen, Z. X.; Cheng, Q.; Li, X. Y.; Li, Z.; Song, Y. W.; Sun, F.; Zhao, M.; Zhang, X. Q.; Li, B. Q.; Huang, J. Q. Cathode Kinetics Evaluation in Lean-Electrolyte Lithium-Sulfur Batteries. *J Am Chem Soc* **2023**, *145* (30), 16449–16457.

(29) Chen, Y.; Wang, T.; Tian, H.; Su, D.; Zhang, Q.; Wang, G. Advances in Lithium-Sulfur Batteries: From Academic Research to Commercial Viability. *Adv Mater* **2021**, *33* (29), e2003666.

(30) Guo, J.; Pei, H.; Dou, Y.; Zhao, S.; Shao, G.; Liu, J. Rational Designs for Lithium-

Sulfur Batteries with Low Electrolyte/Sulfur Ratio. *Adv. Funct. Mater.* **2021**, *31* (18), 2010499.

(31) Peng, H.-J.; Huang, J.-Q.; Cheng, X.-B.; Zhang, Q. Review on High-Loading and High-Energy Lithium-Sulfur Batteries. *Adv. Energy Mater.* **2017**, *7* (24), 1700260.

(32) Zhao, M.; Li, B. Q.; Zhang, X. Q.; Huang, J. Q.; Zhang, Q. A Perspective toward Practical Lithium-Sulfur Batteries. *ACS Cent. Sci.* **2020**, *6* (7), 1095-1104.

(33) Zhao, M.; Li, B. Q.; Peng, H. J.; Yuan, H.; Wei, J. Y.; Huang, J. Q. Lithium-Sulfur Batteries under Lean Electrolyte Conditions: Challenges and Opportunities. *Angew. Chem., Int. Ed. Engl.* **2020**, *59* (31), 12636-12652.

(34) Chung, S.-H.; Manthiram, A. Designing Lithium-Sulfur Cells with Practically Necessary Parameters. *Joule* **2018**, *2* (4), 710-724.

(35) Liu, J.; Bao, Z.; Cui, Y.; Dufek, E. J.; Goodenough, J. B.; Khalifah, P.; Li, Q.; Liaw, B. Y.; Liu, P.; Manthiram, A.; et al. Pathways for Practical High-Energy Long-Cycling Lithium Metal Batteries. *Nat. Energy* **2019**, *4* (3), 180-186.

(36) Gering, K. L. Prediction of Electrolyte Viscosity for Aqueous and Non-Aqueous Systems: Results from a Molecular Model Based on Ion Solvation and a Chemical Physics Framework. *Electrochim. Acta* **2006**, *51* (15), 3125-3138.

(37) Conder, J.; Bouchet, R.; Trabesinger, S.; Marino, C.; Gubler, L.; Villevieille, C. Direct Observation of Lithium Polysulfides in Lithium–Sulfur Batteries Using Operando X-Ray diffraction. *Nat. Energy* **2017**, *2* (6), 17069.

(38) Chien, Y.-C.; Menon, A. S.; Brant, W. R.; Lacey, M. J.; Brandell, D. Understanding the Impact of Precipitation Kinetics on the Electrochemical Performance of Lithium–

Sulfur Batteries by Operando X-Ray Diffraction. *J. Phys. Chem. C* **2022**, *126* (6), 2971-2979.

(39) Seh, Z. W.; Sun, Y.; Zhang, Q.; Cui, Y. Designing High-Energy Lithium-Sulfur Batteries. *Chem Soc Rev* **2016**, *45* (20), 5605-5634.

(40) Ye, H.; Li, Y. Room-Temperature Metal–Sulfur Batteries: What Can We Learn from Lithium–Sulfur? *InfoMat* **2022**, e12291.

(41) Wang, Z.; Tang, Y.; Zhang, L.; Li, M.; Shan, Z.; Huang, J. In Situ Tem Observations of Discharging/ Charging of Solid-State Lithium-Sulfur Batteries at High Temperatures. *Small* **2020**, *16* (28), e2001899.

(42) Xu, Z.-L.; Huang, J.-Q.; Chong, W. G.; Qin, X.; Wang, X.; Zhou, L.; Kim, J.-K. In Situ Tem Study of Volume Expansion in Porous Carbon Nanofiber/Sulfur Cathodes with Exceptional High-Rate Performance. *Adv. Energy Mater.* **2017**, *7* (9), 1602078.

(43) Kim, H.; Lee, J. T.; Magasinski, A.; Zhao, K.; Liu, Y.; Yushin, G. In Situ Tem Observation of Electrochemical Lithiation of Sulfur Confined within Inner Cylindrical Pores of Carbon Nanotubes. *Adv. Energy Mater.* **2015**, *5* (24), 1501306.

(44) Yan, Z.; Liang, Y.; Xiao, J.; Lai, W.; Wang, W.; Xia, Q.; Wang, Y.; Gu, Q.; Lu, H.; Chou, S. L.; et al. A High-Kinetics Sulfur Cathode with a Highly Efficient Mechanism for Superior Room-Temperature Na-S Batteries. *Adv. Mater.* **2020**, *32* (8), e1906700.

(45) Wu, X.; Li, S.; Yang, B.; Wang, C. In Situ Transmission Electron Microscopy Studies of Electrochemical Reaction Mechanisms in Rechargeable Batteries. *Electrochem. Energy Rev.* **2019**, *2* (3), 467-491.

(46) Chen, W.; Qian, T.; Xiong, J.; Xu, N.; Liu, X.; Liu, J.; Zhou, J.; Shen, X.; Yang, T.;

Chen, Y.; et al. A New Type of Multifunctional Polar Binder: Toward Practical Application of High Energy Lithium Sulfur Batteries. *Adv. Mater.* **2017**, *29* (12), 1605160.

(47) Yang, T.; Qian, T.; Liu, J.; Xu, N.; Li, Y.; Grundish, N.; Yan, C.; Goodenough, J. B. A New Type of Electrolyte System to Suppress Polysulfide Dissolution for Lithium-Sulfur Battery. *ACS Nano* **2019**, *13* (8), 9067-9073.

(48) Liu, X.; Qian, T.; Liu, J.; Tian, J.; Zhang, L.; Yan, C. Greatly Improved Conductivity of Double-Chain Polymer Network Binder for High Sulfur Loading Lithium-Sulfur Batteries with a Low Electrolyte/Sulfur Ratio. *Small* **2018**, *14*, e1801536.

(49) Zou, Q.; Liang, Z.; Du, G. Y.; Liu, C. Y.; Li, E. Y.; Lu, Y. C. Cation-Directed Selective Polysulfide Stabilization in Alkali Metal-Sulfur Batteries. *J. Am. Chem. Soc.* **2018**, *140* (34), 10740-10748.

(50) Hua, W.; Li, H.; Pei, C.; Xia, J.; Sun, Y.; Zhang, C.; Lv, W.; Tao, Y.; Jiao, Y.; Zhang, B.; et al. Selective Catalysis Remedies Polysulfide Shuttling in Lithium-Sulfur Batteries. *Adv. Mater.* **2021**, *33* (38), 2101006.

(51) Xue, L.; Li, Y.; Hu, A.; Zhou, M.; Chen, W.; Lei, T.; Yan, Y.; Huang, J.; Yang, C.; Wang, X.; et al. In Situ/Operando Raman Techniques in Lithium–Sulfur Batteries. *Small Structures* **2022**, *3* (3), 2100170.

(52) Wu, H. L.; Huff, L. A.; Gewirth, A. A. In Situ Raman Spectroscopy of Sulfur Speciation in Lithium-Sulfur Batteries. *ACS Appl. Mater. Interfaces* **2015**, *7* (3), 1709-1719.

(53) Wang, T.; Zhang, Q.; Zhong, J.; Chen, M.; Deng, H.; Cao, J.; Wang, L.; Peng, L.; Zhu, J.; Lu, B. 3d Holey Graphene/Polyacrylonitrile Sulfur Composite Architecture for High Loading Lithium Sulfur Batteries. *Adv. Energy Mater.* **2021**, *11* (16), 2100448.

(54) Dominko, R.; Vizintin, A.; Aquilanti, G.; Stievano, L.; Helen, M. J.; Munnangi, A. R.; Fichtner, M.; Arcon, I. Polysulfides Formation in Different Electrolytes from the Perspective of X-Ray Absorption Spectroscopy. *J. Electrochem. Soc.* **2017**, *165* (1), A5014-A5019.

(55) Celorrio, V.; Leach, A. S.; Huang, H.; Hayama, S.; Freeman, A.; Inwood, D. W.; Fermin, D. J.; Russell, A. E. Relationship between Mn Oxidation State Changes and Oxygen Reduction Activity in (La, Ca)Mno_3 as Probed by in Situ Xas and Xes. *ACS Catal.* **2021**, *11* (11), 6431-6439.

(56) Srinath, N. V.; Longo, A.; Poelman, H.; Ramachandran, R. K.; Feng, J.-Y.; Dendooven, J.; Reyniers, M.-F.; Galvita, V. V. In Situ Xas/Saxs Study of Al2o3-Coated Ptga Catalysts for Propane Dehydrogenation. *ACS Catal.* **2021**, *11* (18), 11320-11335.

(57) Li, H.; Meng, R.; Guo, Y.; Chen, B.; Jiao, Y.; Ye, C.; Long, Y.; Tadich, A.; Yang, Q. H.; Jaroniec, M.; et al. Reversible Electrochemical Oxidation of Sulfur in Ionic Liquid for High-Voltage Al-S Batteries. *Nat. Commun.* **2021**, *12* (1), 5714.

(58) Xu, Y.; Ye, Y.; Zhao, S.; Feng, J.; Li, J.; Chen, H.; Yang, A.; Shi, F.; Jia, L.; Wu, Y.; et al. In Situ X-Ray Absorption Spectroscopic Investigation of the Capacity Degradation Mechanism in Mg/S Batteries. *Nano Lett.* **2019**, *19* (5), 2928-2934.

(59) Wu, C.; Lei, Y.; Simonelli, L.; Tonti, D.; Black, A.; Lu, X.; Lai, W. H.; Cai, X.; Wang, Y. X.; Gu, Q.; et al. Continuous Carbon Channels Enable Full Na-Ion

Accessibility for Superior Room-Temperature Na-S Batteries. *Adv. Mater.* **2022**, *34* (8), e2108363.

(60) Ye, C.; Chao, D.; Shan, J.; Li, H.; Davey, K.; Qiao, S.-Z. Unveiling the Advances of 2d Materials for Li/Na-S Batteries Experimentally and Theoretically. *Mater.* **2020**, *2* (2), 323-344.

(61) Ci, H.; Cai, J.; Ma, H.; Shi, Z.; Cui, G.; Wang, M.; Jin, J.; Wei, N.; Lu, C.; Zhao, W.; et al. Defective Vse2-Graphene Heterostructures Enabling in Situ Electrocatalyst Evolution for Lithium-Sulfur Batteries. *ACS Nano* **2020**, *14* (9), 11929-11938.

(62) Zhang, S.; Yao, Y.; Jiao, X.; Ma, M.; Huang, H.; Zhou, X.; Wang, L.; Bai, J.; Yu, Y. Mo2 N-W2 N Heterostructures Embedded in Spherical Carbon Superstructure as Highly Efficient Polysulfide Electrocatalysts for Stable Room-Temperature Na-S Batteries. *Adv. Mater.* **2021**, *33* (43), e2103846.

(63) Meng, Z.; Foix, D.; Brun, N.; Dedryvère, R.; Stievano, L.; Morcrette, M.; Berthelot, R. Alloys to Replace Mg Anodes in Efficient and Practical Mg-Ion/Sulfur Batteries. *ACS Energy Lett.* **2019**, *4* (9), 2040-2044.

(64) Zhao, E.; Nie, K.; Yu, X.; Hu, Y. S.; Wang, F.; Xiao, J.; Li, H.; Huang, X. Advanced Characterization Techniques in Promoting Mechanism Understanding for Lithium–Sulfur Batteries. *Adv. Funct. Mater.* **2018**, *28* (38), 1707543.

(65) Zhang, Y.; Luo, Y.; Fincher, C.; McProuty, S.; Swenson, G.; Banerjee, S.; Pharr, M. In-Situ Measurements of Stress Evolution in Composite Sulfur Cathodes. *Energy Storage Mater.* **2019**, *16*, 491-497.

(66) Luo, L.; Li, J.; Yaghoobnejad Asl, H.; Manthiram, A. In-Situ Assembled Vs4 as a

Polysulfide Mediator for High-Loading Lithium–Sulfur Batteries. *ACS Energy Letters* **2020**, *5* (4), 1177-1185.

(67) Feng, Z.; Kim, C.; Vijh, A.; Armand, M.; Bevan, K. H.; Zaghib, K. Unravelling the Role of Li_2s_2 in Lithium–Sulfur Batteries: A First Principles Study of Its Energetic and Electronic Properties. *J. Power Sources* **2014**, *272*, 518-521.

(68) Luo, Y.; Fang, Z.; Duan, S.; Wu, H.; Liu, H.; Zhao, Y.; Wang, K.; Li, Q.; Fan, S.; Zheng, Z.; et al. Direct Monitoring of Li(2) S(2) Evolution and Its Influence on the Reversible Capacities of Lithium-Sulfur Batteries. *Angew. Chem., Int. Ed. Engl.* **2023**, *62* (11), e202215802.

(69) Chao Ye; Yan Jiao; Huanyu Jin; Ashley D. Slattery; Kenneth Davey; Haihui Wang; Qiao, S.-Z. 2d Mon-Vn Heterostructure to Regulate Polysulfides for Highly Efficient Lithium-Sulfur.Pdf>. *Angew. Chem. Int. Ed.* **2018**, *57*, 16703 –16707.

(70) Ma, C.; Zhang, Y.; Feng, Y.; Wang, N.; Zhou, L.; Liang, C.; Chen, L.; Lai, Y.; Ji, X.; Yan, C.; et al. Engineering Fe-N Coordination Structures for Fast Redox Conversion in Lithium-Sulfur Batteries. *Adv. Mater.* **2021**, *33* (30), e2100171.

(71) Qian, J.; Wang, F.; Li, Y.; Wang, S.; Zhao, Y.; Li, W.; Xing, Y.; Deng, L.; Sun, Q.; Li, L.; et al. Electrocatalytic Interlayer with Fast Lithium–Polysulfides Diffusion for Lithium–Sulfur Batteries to Enhance Electrochemical Kinetics under Lean Electrolyte Conditions. *Adv. Funct. Mater.* **2020**, *30* (27), 2000742.

(72) He, J.; Bhargav, A.; Manthiram, A. Molybdenum Boride as an Efficient Catalyst for Polysulfide Redox to Enable High-Energy-Density Lithium-Sulfur Batteries. *Adv. Mater.* **2020**, *32* (40), e2004741.

(73) Wang, L.; Wang, Z.-Y.; Wu, J.-F.; Li, G.-R.; Liu, S.; Gao, X.-P. To Effectively Drive the Conversion of Sulfur with Electroactive Niobium Tungsten Oxide Microspheres for Lithium−Sulfur Battery. *Nano Energy* **2020**, *77*, 105173.

(74) Liu, X.-C.; Yang, Y.; Wu, J.; Liu, M.; Zhou, S. P.; Levin, B. D. A.; Zhou, X.-D.; Cong, H.; Muller, D. A.; Ajayan, P. M.; et al. Dynamic Hosts for High-Performance Li–S Batteries Studied by Cryogenic Transmission Electron Microscopy and in Situ X-Ray Diffraction. *ACS Energy Lett.* **2018**, *3* (6), 1325-1330.

(75) Xu, Z.-L.; Kim, S. J.; Chang, D.; Park, K.-Y.; Dae, K. S.; Dao, K. P.; Yuk, J. M.; Kang, K. Visualization of Regulated Nucleation and Growth of Lithium Sulfides for High Energy Lithium Sulfur Batteries. *Energy Environ. Sci.* **2019**, *12* (10), 3144-3155.

(76) Tang, W.; Chen, Z.; Tian, B.; Lee, H. W.; Zhao, X.; Fan, X.; Fan, Y.; Leng, K.; Peng, C.; Kim, M. H.; et al. In Situ Observation and Electrochemical Study of Encapsulated Sulfur Nanoparticles by Mos2 Flakes. *J. Am. Chem. Soc.* **2017**, *139* (29), 10133-10141.

(77) Hwa, Y.; Seo, H. K.; Yuk, J. M.; Cairns, E. J. Freeze-Dried Sulfur-Graphene Oxide-Carbon Nanotube Nanocomposite for High Sulfur-Loading Lithium/Sulfur Cells. *Nano Lett.* **2017**, *17* (11), 7086-7094.

(78) Liu, H.; Lai, W.-H.; Liang, Y.; Liang, X.; Yan, Z.-C.; Yang, H.-L.; Lei, Y.-J.; Wei, P.; Zhou, S.; Gu, Q.-F.; et al. Sustainable S Cathodes with Synergic Electrocatalysis for Room-Temperature Na–S Batteries. *J. Mater. Chem. A* **2021**, *9* (1), 566-574.

(79) Ding, X.; Yang, S.; Zhou, S.; Zhan, Y.; Lai, Y.; Zhou, X.; Xu, X.; Nie, H.; Huang, S.; Yang, Z. Biomimetic Molecule Catalysts to Promote the Conversion of Polysulfides

for Advanced Lithium-Sulfur Batteries. *Adv. Funct. Mater.* **2020**, *30* (38), 2003354.

(80) Xu, N.; Qian, T.; Liu, X.; Liu, J.; Chen, Y.; Yan, C. Greatly Suppressed Shuttle Effect for Improved Lithium Sulfur Battery Performance through Short Chain Intermediates. *Nano Lett.* **2016**, *17* (1), 538-543.

(81) Zhou, J.; Ji, H.; Liu, J.; Qian, T.; Yan, C. A New High Ionic Conductive Gel Polymer Electrolyte Enables Highly Stable Quasi-Solid-State Lithium Sulfur Battery. *Energy Storage Mater.* **2019**, *22*, 256-264.

(82) Du, M.; Geng, P.; Pei, C.; Jiang, X.; Shan, Y.; Hu, W.; Ni, L.; Pang, H. High-Entropy Prussian Blue Analogues and Their Oxide Family as Sulfur Hosts for Lithium-Sulfur Batteries. *Angew. Chem., Int. Ed. Engl.* **2022**, *61* (41), e202209350.

(83) Lang, S.; Yu, S. H.; Feng, X.; Krumov, M. R.; Abruna, H. D. Understanding the Lithium-Sulfur Battery Redox Reactions Via Operando Confocal Raman Microscopy. *Nat. Commun.* **2022**, *13* (1), 4811.

(84) Zhu, W.; Paolella, A.; Kim, C. S.; Liu, D.; Feng, Z.; Gagnon, C.; Trottier, J.; Vijh, A.; Guerfi, A.; Mauger, A.; et al. Investigation of the Reaction Mechanism of Lithium Sulfur Batteries in Different Electrolyte Systems by in Situ Raman Spectroscopy and in Situ X-Ray Diffraction. *Sustain. Energy Fuels* **2017**, *1* (4), 737-747.

(85) Xue, P.; Zhu, K.; Gong, W.; Pu, J.; Li, X.; Guo, C.; Wu, L.; Wang, R.; Li, H.; Sun, J.; et al. “One Stone Two Birds” Design for Dual-Functional Tio$_2$-Tin Heterostructures Enabled Dendrite-Free and Kinetics-Enhanced Lithium–Sulfur Batteries. *Adv. Energy Mater.* **2022**, *12* (18),

(86) Sun, R.; Bai, Y.; Bai, Z.; Peng, L.; Luo, M.; Qu, M.; Gao, Y.; Wang, Z.; Sun, W.;

Sun, K. Phosphorus Vacancies as Effective Polysulfide Promoter for High-Energy-Density Lithium–Sulfur Batteries. *Adv. Energy Mater.* **2022**, *12* (12), 2102739.

(87) Robba, A.; Vizintin, A.; Bitenc, J.; Mali, G.; Arčon, I.; Kavčič, M.; Žitnik, M.; Bučar, K.; Aquilanti, G.; Martineau-Corcos, C.; et al. Mechanistic Study of Magnesium–Sulfur Batteries. *Chem. Mater.* **2017**, *29* (21), 9555-9564.

(88) Xu, Y.; Zhao, Y.; Zhao, S.; Zhang, J.; Li, J.; Guo, J.; Zhang, Y. Reversible Function Switching of Ag Catalyst in Mg/S Battery with Chloride-Containing Electrolyte. *Energy Storage Mater.* **2021**, *42*, 513-516.

(89) Zech, C.; Hönicke, P.; Kayser, Y.; Risse, S.; Grätz, O.; Stamm, M.; Beckhoff, B. Polysulfide Driven Degradation in Lithium–Sulfur Batteries During Cycling – Quantitative and High Time-Resolution Operando X-Ray Absorption Study for Dissolved Polysulfides Probed at Both Electrode Sides. *J. Mater. Chem. A* **2021**, *9* (16), 10231-10239.

(90) Pang, Q.; Kundu, D.; Cuisinier, M.; Nazar, L. F. Surface-Enhanced Redox Chemistry of Polysulphides on a Metallic and Polar Host for Lithium-Sulphur Batteries. *Nat. Commun.* **2014**, *5*, 4759.

(91) Yang, X.; Gao, X.; Sun, Q.; Jand, S. P.; Yu, Y.; Zhao, Y.; Li, X.; Adair, K.; Kuo, L. Y.; Rohrer, J.; et al. Promoting the Transformation of $Li_2 S_2$ to Li_2s: Significantly Increasing Utilization of Active Materials for High-Sulfur-Loading Li-S Batteries. *Adv. Mater.* **2019**, *31* (25), e1901220.

(92) Benayad, A.; Morales-Ugarte, J. E.; Santini, C. C.; Bouchet, R. Operando Xps: A Novel Approach for Probing the Lithium/Electrolyte Interphase Dynamic Evolution. *J.*

Phys. Chem. A **2021**, *125* (4), 1069-1081.

(93) Nandasiri, M. I., Luis E. Camacho-Forero, Ashleigh M. Schwarz, Vaithiyalingam Shutthanandan, Suntharampillai Thevuthasan, Perla B. Balbuena, Karl T. Mueller, and Vijayakumar Murugesan. In-Situ Chemical Imaging of Solid-Electrolyte Interphase Layer. *Chem. Mater.* **2017**, *29*, 4728–4737.

(94) Zhang, Y.; Yang, S.; Zhou, S.; Zhang, L.; Gu, B.; Dong, Y.; Kong, S.; Cai, D.; Fang, G.; Nie, H.; et al. Oxygen Doping in Antimony Sulfide Nanosheets to Facilitate Catalytic Conversion of Polysulfides for Lithium-Sulfur Batteries. *Chem. Commun.* **2021**, *57* (26), 3255-3258.

(95) Bhardwaj, R. K.; Gomes, R.; Bhattacharyya, A. J. Probing the Polysulfide Confinement in Two Different Sulfur Hosts for a Mg|S Battery Employing Operando Raman and Ex-Situ Uv-Visible Spectroscopy. *J. Phys. Chem. Lett.* **2022**, *13* (5), 1159-1164.

(96) Wang, J.; Cheng, S.; Li, W.; Jia, L.; Xiao, Q.; Hou, Y.; Zheng, Z.; Li, H.; Zhang, S.; Zhou, L.; et al. Robust Electrical "Highway" Network for High Mass Loading Sulfur Cathode. *Nano Energy* **2017**, *40*, 390-398.

(97) Dillard, C.; Singh, A.; Kalra, V. Polysulfide Speciation and Electrolyte Interactions in Lithium–Sulfur Batteries with in Situ Infrared Spectroelectrochemistry. *J. Phys. Chem. C* **2018**, *122* (32), 18195-18203.

(98) Saqib, N.; Ohlhausen, G. M.; Porter, J. M. In Operando Infrared Spectroscopy of Lithium Polysulfides Using a Novel Spectro-Electrochemical Cell. *J. Power Sources* **2017**, *364*, 266-271.

(99) Lang, S. Y.; Shi, Y.; Guo, Y. G.; Wang, D.; Wen, R.; Wan, L. J. Insight into the Interfacial Process and Mechanism in Lithium-Sulfur Batteries: An in Situ Afm Study. *Angew. Chem. Int. Ed.* **2016**, *55* (51), 15835-15839.

(100) Lang, S. Y.; Shi, Y.; Guo, Y. G.; Wen, R.; Wan, L. J. High-Temperature Formation of a Functional Film at the Cathode/Electrolyte Interface in Lithium-Sulfur Batteries: An in Situ Afm Study. *Angew. Chem. Int. Ed.* **2017**, *56* (46), 14433-14437.

(101) Steudel, R. Elemental Sulfur and Sulfur-Rich Compounds Ii. In *Liquid Sulfur*, Steudel, R. Ed.; Vol. 2; Springer Science & Business Media Verlag: Berlin, Heidelberg, NewYork, 2003; pp pp81-116.

(102) Zhou, G.; Yang, A.; Wang, Y.; Gao, G.; Pei, A.; Yu, X.; Zhu, Y.; Zong, L.; Liu, B.; Xu, J.; et al. Electrotunable Liquid Sulfur Microdropletsopy. *Nat. Commun.* **2020**, *11* (1), 606.

(103) Kresse, G.; Furthmuller, J. Efficient Iterative Schemes for Ab Initio Total-Energy Calculations Using a Plane-Wave Basis Set. *Phys. Rev. B* **1996**, *54* (16), 11169-11186.

(104) Kresse, G.; Furthmuller, J. Efficiency of Ab-Initio Total Energy Calculations for Metals and Semiconductors Using a Plane-Wave Basis Set. *Comput. Mater. Sci.* **1996**, *6* (1), 15-50.

(105) Grimme, S.; Antony, J.; Ehrlich, S.; Krieg, H. A Consistent and Accurate Ab Initio Parametrization of Density Functional Dispersion Correction (Dft-D) for the 94 Elements H-Pu. *Chem. Phys.* **2010**, *132* (15), 154104.

(106) Laturia, A.; Van de Put, M. L.; Vandenberghe, W. G. Dielectric Properties of Hexagonal Boron Nitride and Transition Metal Dichalcogenides: From Monolayer to

Bulk. *NPJ 2D Mater. Appl* **2018**, *2* (1), 4106.

(107) Dukštienė, N.; Sinkevičiūtė, D. Photoelectrochemical Properties of Moo2 Thin Films. *J. Solid State Electrochem.* **2013**, *17* (4), 1175-1184.

(108) Xu, Z.-L.; Onofrio, N.; Wang, J. Boosting the Anchoring and Catalytic Capability of Mos$_2$ for High-Loading Lithium Sulfur Batteries. *J. Mater. Chem. A* **2020**, *8* (34), 17646-17656.

(109) Yang, Z.; Zhu, Z.; Ma, J.; Xiao, D.; Kui, X.; Yao, Y.; Yu, R.; Wei, X.; Gu, L.; Hu, Y.-S.; et al. Phase Separation of L$_{i2}$s/S at Nanoscale During Electrochemical Lithiation of the Solid-State Lithium–Sulfur Battery Using in Situ Tem. *Adv. Energy Mater.* **2016**, *6* (20), 1600806.

(110) Gorlin, Y.; Patel, M. U. M.; Freiberg, A.; He, Q.; Piana, M.; Tromp, M.; Gasteiger, H. A. Understanding the Charging Mechanism of Lithium-Sulfur Batteries Using Spatially Resolved Operando X-Ray Absorption Spectroscopy. *J. Electrochem. Soc.* **2016**, *163* (6), A930-A939.

(111) Ye, G.; Gong, Y.; Lin, J.; Li, B.; He, Y.; Pantelides, S. T.; Zhou, W.; Vajtai, R.; Ajayan, P. M. Defects Engineered Monolayer Mos$_2$ for Improved Hydrogen Evolution Reaction. *Nano Lett.* **2016**, *16* (2), 1097-1103.

(112) Nims, C.; Cron, B.; Wetherington, M.; Macalady, J.; Cosmidis, J. Low Frequency Raman Spectroscopy for Micron-Scale and in Vivo Characterization of Elemental Sulfur in Microbial Sampleses. *Sci. Rep.* **2019**, *9* (1), 7971.

(113) Wang, H.-E.; Li, X.; Qin, N.; Zhao, X.; Cheng, H.; Cao, G.; Zhang, W. Sulfur-Deficient Mos$_2$ Grown inside Hollow Mesoporous Carbon as a Functional Polysulfide

Mediator. *J. Mater. Chem. A* **2019**, *7* (19), 12068-12074.

(114) Liu, B.; Ma, C.; Liu, D.; Yan, S. Sulfur-Vacancy Defective Mos2 as a Promising Electrocatalyst for Nitrogen Reduction Reaction under Mild Conditions. *ChemElectroChem* **2021**, *8* (16), 3030-3039.

(115) Wang, H.; Xu, X.; Neville, A. Facile Synthesis of Vacancy-Induced 2h-Mos2 Nanosheets and Defect Investigation for Supercapacitor Application. *RSC Adv.* **2021**, *11* (42), 26273-26283.

(116) Goodrich, F. C. On Diffusion-Controlled Particle Growth the Moving Boundary Probleme. *J. Phys. Chem.* **1966**, *70*, 3660-3665.

(117) Huang, W.; Li, J.; Xu, Y. Nucleation/Growth Mechanisms and Morphological Evolution of Porous Mno2 Coating Deposited on Graphite for Supercapacitor. *Mater.* **2017**, *10* (10), 1205.

(118) Dahiya, P.; Caggioni, M.; Spicer, P. T. Arrested Coalescence of Viscoelastic Droplets: Polydisperse Doublets. *Philos. Trans. R. Soc. A* **2016**, *374* (2072), 20150132.

(119) Nam, Y.; Kim, H.; Shin, S. Energy and Hydrodynamic Analyses of Coalescence-Induced Jumping Droplets. *Appl. Phys. Lett.* **2013**, *103* (16), 3660-3665.

(120) Lin, H.; Yang, L.; Jiang, X.; Li, G.; Zhang, T.; Yao, Q.; Zheng, G. W.; Lee, J. Y. Electrocatalysis of Polysulfide Conversion by Sulfur-Deficient Mos2 Nanoflakes for Lithium-Sulfur Batteries. *Energy Environ. Sci.* **2017**, *10* (6), 1476-1486.

(121) Kumari, L.; Ma, Y.-R.; Tsai, C.-C.; Lin, Y.-W.; Wu, S. Y.; Cheng, K.-W.; Liou, Y. X-Ray Diffraction and Raman Scattering Studies on Large-Area Array and Nanobranched Structure of 1d Moo2 Nanorodss. *Nanotechnology* **2007**, *18* (11), 115717.

(122) Kiriya, D.; Lobaccaro, P.; Nyein, H. Y.; Taheri, P.; Hettick, M.; Shiraki, H.; Sutter-Fella, C. M.; Zhao, P.; Gao, W.; Maboudian, R.; et al. General Thermal Texturization Process of Mos2 for Efficient Electrocatalytic Hydrogen Evolution Reaction. *Nano Lett.* **2016**, *16* (7), 4047-4053.

(123) Wu, W.; Niu, C.; Wei, C.; Jia, Y.; Li, C.; Xu, Q. Activation of Mos2 Basal Planes for Hydrogen Evolution by Zinc. *Angew. Chem. Int. Ed.* **2019**, *58* (7), 2029-2033.

(124) Jayan, R.; Islam, M. M. First-Principles Investigation of the Anchoring Behavior of Pristine and Defect-Engineered Tungsten Disulfide for Lithium–Sulfur Batteries. *J. Phys. Chem. C* **2020**, *124* (50), 27323-27332.

(125) Gupta, A.; Manthiram, A. Designing Advanced Lithium-Based Batteries for Low-Temperature Conditions. *Adv. Energy Mater.* **2020**, *10* (38), 2001972.

(126) Deng, D. R.; Xue, F.; Bai, C. D.; Lei, J.; Yuan, R.; Zheng, M. S.; Dong, Q. F. Enhanced Adsorptions to Polysulfides on Graphene-Supported Bn Nanosheets with Excellent Li-S Battery Performance in a Wide Temperature Range. *ACS Nano* **2018**, *12* (11), 11120-11129.

(127) Holoubek, J.; Liu, H.; Wu, Z.; Yin, Y.; Xing, X.; Cai, G.; Yu, S.; Zhou, H.; Pascal, T. A.; Chen, Z.; et al. Tailoring Electrolyte Solvation for Li Metal Batteries Cycled at Ultra-Low Temperature. *Nat. Energy* **2021**, *6*, 303-313.

(128) Yu, S. H.; Huang, X.; Schwarz, K.; Huang, R.; Arias, T. A.; Brock, J. D.; Abruna, H. D. Direct Visualization of Sulfur Cathodes: New Insights into Li-S Batteries Via Operando X-Ray Based Methods. *Energy Environ. Sci.* **2018**, *8* (1), 202-210.

(129) Tonin, G.; Vaughan, G. B. M.; Bouchet, R.; Alloin, F.; Di Michiel, M.; Barchasz,

C. Operando Investigation of the Lithium/Sulfur Battery System by Coupled X-Ray Absorption Tomography and X-Ray Diffraction Computed Tomography. *J. Power Sources* **2020**, *468*,

(130) Shi, F.; Onofrio, N.; Chen, C.; Cai, S.; Li, Y.; Zhai, L.; Zhuang, L.; Xu, Z. L.; Lau, S. P. Stable Liquid-Sulfur Generation on Transition-Metal Dichalcogenides toward Low-Temperature Lithium-Sulfur Batteries. *ACS Nano* **2022**, *16* (9), 14412-14421.

(131) Tian, J. H.; Jiang, T.; Wang, M.; Hu, Z.; Zhu, X.; Zhang, L.; Qian, T.; Yan, C. In Situ/Operando Spectroscopic Characterizations Guide the Compositional and Structural Design of Lithium–Sulfur Batteries. *Small Methods* **2019**, *4* (6), 1900467.

(132) Trofimov, B. A.; Sinegovskaya, L. M.; Gusarova, N. K. Vibrations of the S–S Bond in Elemental Sulfur and Organic Polysulfides: A Structural Guide. *J. Sulphur Chem.* **2009**, *30* (5), 518-554.

(133) Eckert, B.; Albert, H. O.; Jodl, H. J.; Foggi, P. Raman Studies of Sulfur Crystal (R-S_8) at High Pressures and Low Temperatures. *J. Phys. Chem.* **1996**, *100*, 8212-8219.

(134) Thanh, N. T.; Maclean, N.; Mahiddine, S. Mechanisms of Nucleation and Growth of Nanoparticles in Solution. *Chem. Rev.* **2014**, *114* (15), 7610-7630.

(135) Biswal, P.; Stalin, S.; Kludze, A.; Choudhury, S.; Archer, L. A. Nucleation and Early Stage Growth of Li Electrodeposits. *Nano Lett.* **2019**, *19* (11), 8191-8200.

(136) Wang, L.; Wang, F.; Lu, C.; Liu, H. Nucleation in Supercooled Water Triggered by Mechanical Impact: Experimental and Theoretical Analyses. *J. Energy Storage* **2022**, *52*, 104755.

(137) Li, Y.; Huang, W.; Li, Y.; Chiu, W.; Cui, Y. Opportunities for Cryogenic Electron

Microscopy in Materials Science and Nanoscience. *ACS Nano* **2020**, *14* (8), 9263-9276.

(138) Geng, C.; Hua, W.; Wang, D.; Ling, G.; Zhang, C.; Yang, Q. H. Demystifying the Catalysis in Lithium–Sulfur Batteries: Characterization Methods and Techniques. *SusMat* **2021**, *1* (1), 51-65.

(139) Yu, X.; Liu, Z.; Yang, X.; Wang, Y.; Zhang, J.; Duan, J.; Liu, L.; Tang, Q. Crystal-Plane Controlled Spontaneous Polarization of Inorganic Perovskite toward Boosting Triboelectric Surface Charge Density. *ACS Appl. Mater. Interfaces* **2021**, *13* (22), 26196-26203.

(140) Pei, A.; Zheng, G.; Shi, F.; Li, Y.; Cui, Y. Nanoscale Nucleation and Growth of Electrodeposited Lithium Metal. *Nano Lett.* **2017**, *17* (2), 1132-1139.

(141) Chu, R.; Nguyen, T. T.; Bai, Y.; Kim, N. H.; Lee, J. H. Uniformly Controlled Treble Boundary Using Enriched Adsorption Sites and Accelerated Catalyst Cathode for Robust Lithium–Sulfur Batteries. *Adv. Energy Mater.* **2022**, *12* (9), 2102805.

(142) Wang, S.; Feng, S.; Liang, J.; Su, Q.; Zhao, F.; Song, H.; Zheng, M.; Sun, Q.; Song, Z.; Jia, X.; et al. Insight into Mos_2–Mon Heterostructure to Accelerate Polysulfide Conversion toward High-Energy-Density Lithium-Sulfur Batteries. *Adv. Energy Mater.* **2021**, *11* (11), 2003314.

(143) Zhao, M.; Peng, H. J.; Zhang, Z. W.; Li, B. Q.; Chen, X.; Xie, J.; Chen, X.; Wei, J. Y.; Zhang, Q.; Huang, J. Q. Activating Inert Metallic Compounds for High-Rate Lithium-Sulfur Batteries through in Situ Etching of Extrinsic Metal. *Angew. Chem. Int. Ed.* **2019**, *58* (12), 3779-3783.

(144) Zhao, C.; Xu, G. L.; Yu, Z.; Zhang, L.; Hwang, I.; Mo, Y. X.; Ren, Y.; Cheng, L.;

Sun, C. J.; Ren, Y.; et al. A High-Energy and Long-Cycling Lithium-Sulfur Pouch Cell Via a Macroporous Catalytic Cathode with Double-End Binding Sites. *Nat. Nanotechnol.* **2021**, *16* (2), 166-173.

(145) Yuan, H.; Peng, H.-J.; Li, B.-Q.; Xie, J.; Kong, L.; Zhao, M.; Chen, X.; Huang, J.-Q.; Zhang, Q. Conductive and Catalytic Triple-Phase Interfaces Enabling Uniform Nucleation in High-Rate Lithium-Sulfur Batteries. *Adv. Energy Mater.* **2019**, *9* (1), 1802768.

(146) Zhang, Y.; Kang, C.; Zhao, W.; Song, Y.; Zhu, J.; Huo, H.; Ma, Y.; Du, C.; Zuo, P.; Lou, S.; et al. D-P Hybridization-Induced "Trapping-Coupling-Conversion" Enables High-Efficiency Nb Single-Atom Catalysis for Li-S Batteries. *J. Am. Chem. Soc.* **2023**, *145* (3), 1728-1739.

(147) Huang, L.; Shen, S.; Zhong, Y.; Zhang, Y.; Zhang, L.; Wang, X.; Xia, X.; Tong, X.; Zhou, J.; Tu, J. Multifunctional Hyphae Carbon Powering Lithium-Sulfur Batteries. *Adv. Mater.* **2022**, *34* (6), e2107415.

(148) Pu, J.; Gong, W.; Shen, Z.; Wang, L.; Yao, Y.; Hong, G. Conio$_2$/Co$_4$n Heterostructure Nanowires Assisted Polysulfide Reaction Kinetics for Improved Lithium-Sulfur Batteries. *Adv. Sci.* **2022**, *9* (4), e2104375.

(149) Manthiram, A. An Outlook on Lithium Ion Battery Technology. *ACS Cent. Sci.* **2017**, *3* (10), 1063-1069.

(150) Lin, D. C.; Liu, Y. Y.; Cui, Y. Reviving the Lithium Metal Anode for High-Energy Batteries. *Nat. Nanotechnol.* **2017**, *12* (3), 194-206.

(151) Shi, F.; Zhai, L.; Liu, Q.; Yu, J.; Lau, S. P.; Xia, B. Y.; Xu, Z.-L. Emerging

Catalytic Materials for Practical Lithium-Sulfur Batteries. *Journal of Energy Chemistry* **2023**, *76*, 127-145.

(152) Dorfler, S.; Walus, S.; Locke, J.; Fotouhi, A.; Auger, D. J.; Shateri, N.; Abendroth, T.; Hartel, P.; Althues, H.; Kaskel, S. Recent Progress and Emerging Application Areas for Lithium-Sulfur Battery Technology. *Energy Technol.* **2021**, *9* (1), 2000694.

(153) Peng, Y.-Q.; Zhao, M.; Chen, Z.-X.; Cheng, Q.; Liu, Y.; Li, X.-Y.; Song, Y.-W.; Li, B.-Q.; Huang, J.-Q. Boosting Sulfur Redox Kinetics by a Pentacenetetrone Redox Mediator for High-Energy-Density Lithium-Sulfur Batteries. *Nano Res.* **2022**, *16* (6), 8253-8259.

(154) Liu, Y.; Hong, D.; Chen, M.; Su, Z.; Gao, Y.; Zhang, Y.; Long, D. Pt-Nbc Composite as a Bifunctional Catalyst for Redox Transformation of Polysulfides in High-Rate-Performing Lithium-Sulfur Batteries. *ACS Appl. Mater. Interfaces* **2021**, *13* (29), 35008-35018.

(155) Al Salem, H.; Babu, G.; Rao, C. V.; Arava, L. M. Electrocatalytic Polysulfide Traps for Controlling Redox Shuttle Process of Li-S Batteries. *J. Am. Chem. Soc.* **2015**, *137* (36), 11542-11545.